

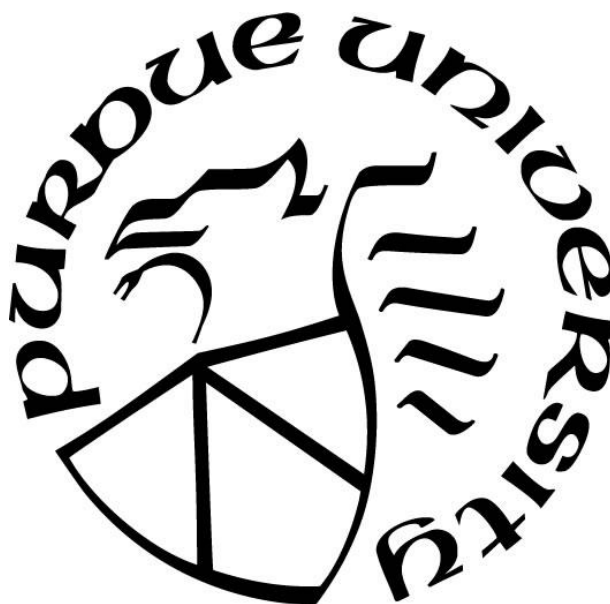
**DEVELOPMENT OF NANOPARTICLES WITH HIGH DRUG
LOADING CAPACITY AND STABILITY**

by
Maie Taha

A Dissertation

*Submitted to the Faculty of Purdue University
In Partial Fulfillment of the Requirements for the degree of*

Doctor of Philosophy



Department of Industrial & Physical Pharmacy

West Lafayette, Indiana

May 2019

THE PURDUE UNIVERSITY GRADUATE SCHOOL
STATEMENT OF COMMITTEE APPROVAL

Dr. Yoon Yeo, Chair

Department of Industrial and Physical Pharmacy

Dr. Kinam Park

Department of Industrial and Physical Pharmacy

Dr. Tonglei Li

Department of Industrial and Physical Pharmacy

Dr. Sandro Matosevic

Department of Industrial and Physical Pharmacy

Approved by:

Dr. Rodolfo Pinal

Head of the Graduate Program

*To my parents and enthusiastic supporters, Wafaa Gaafar and Shaaban Taha, to whom I
owe everything.*

I love you and will always do my best to make you proud of me.

ACKNOWLEDGMENTS

”رَبِّ أَوْزَعْنِي أَنْ أَشْكُرَ نِعْمَتَكَ الَّتِي أَنْعَمْتَ عَلَيَّ وَعَلَى وَالِدَيَّ وَأَنْ أَعْمَلَ صَالِحًا تَرْضَاهُ وَأَدْخِلْنِي بِرَحْمَتِكَ فِي عِبَادِكَ الصَّالِحِينَ“ [النمل: ١٩]

Alhamdulillah, all praises and thanks to Allah the most merciful and most gracious, for endowing me with health, patience, and knowledge to complete this work. Peace and blessing of Allah be upon last Prophet Muhammad (Peace Be upon Him).

First, I would like to express my deepest sense of gratitude to my advisor Dr. Yoon Yeo for her constructive guidance and continuous support throughout my PhD study. Her hardworking, passionate attitude, and attention to detail have set an example I hope to match someday. I would give Dr. Yeo most of the credit for becoming the kind of scientist I am today, and she will remain to be my lifelong mentor.

I also thank the rest of my dissertation committee members, Dr. Kinam Park, Dr. Tonglei Li and Dr. Sandro Matosevic. They generously gave their time to offer invaluable feedback and eye-opening critique on my research. I am also grateful to Dr. Timothy Ratliff and Dr. Greg Creswell for lending me their expertise in immunology.

To the Yeo lab family, thank you for the support, fun and all the enjoyable memories. I could not have asked for better colleagues. I also want to express my heartfelt gratitude to Dr. Sara Ahmed, Dr. Heysun Hyun and Dr. Yihua Pei. Your kindness, sincere advice and cheerfulness always brightened my darkest moments. I am sure our friendship will last a lifetime.

I gratefully acknowledge the funding received towards my PhD from the Egyptian Government and the tax payers in Egypt. This fellowship enabled me to get an exceptional experience in Purdue and grow both personally and academically.

No words could ever express my everlasting gratitude to my parents, the only ones who want to see me better than themselves. For my entire life, they have showered me with unconditional love and unwavering support. By setting high moral standards, they gave me wisdom to be sincere in my work, and their faith in me gave me strength to reach for my dreams.

To my brothers and sisters, thanks for your generous love, encouragement and valuable prayers despite the long distance between us. Life wouldn't have been fun without you.

To my lovely husband and best friend, Mohamed, who have been by my side giving me the courage to embark on this PhD journey. Thanks for all the late nights and early mornings, and

for making me feel special even when times were tough for me. Your love and support have led me to where I am now, I realize a thank you is not enough.

The last word goes to Alei and Zeina, my beloved cute kids, who are the light of my life and whose smiles gave me the strength to finish this work. Thank you for bearing with my absence to do experiments, I am deeply sorry for the time we spent apart. I love you so much and I am blessed to have you.

To all of you, thank you.

Maie Shaaban Taha

TABLE OF CONTENTS

LIST OF TABLES	9
LIST OF FIGURES	10
ABSTRACT.....	14
CHAPTER 1. INTRODUCTION	16
1.1 Nanoparticles for systemic drug delivery.....	16
1.2 Limitations of current NP systems	17
1.2.1 Drug loading capacity	17
1.2.2 Circulation stability.....	18
1.2.3 Drug release kinetics.....	19
1.3 Achieving nanoparticles with high drug loading and circulation stability.....	20
1.3.1 Factors affecting drug loading in NP	20
1.3.2 Factors affecting NP colloidal stability in circulation	22
1.3.3 Factors affecting drug release rate from NP	24
1.3.4 New approaches for preparation of NP with high drug loading capacity and circulation stability	26
1.4 Conclusions	35
1.5 References	37
CHAPTER 2. PREPARATION OF NANOCORE FORMULATION STABILIZED BY TA/Fe ³⁺ INTERFACIAL ASSEMBLIES	48
2.1 Introduction	48
2.2 Materials and Methods	53
2.2.1 Materials.....	53
2.2.2 TA/Fe ³⁺ -stabilized nanocore preparation.....	53
2.2.3 TA/Fe ³⁺ -stabilized nanocore characterization.....	54
2.3 Results	55
2.3.1 Preparation and characterization of TA/Fe ³⁺ -stabilized nanocores	55
2.3.2 Colloidal stability of TA/Fe ³⁺ -stabilized nanocores	57
2.3.3 Co-loading drugs in TA/Fe ³⁺ -stabilized nanocores	58
2.4 Discussion	58

2.5	Conclusions	61
2.6	References	62
CHAPTER 3. SURFACE FUNCTIONALIZATION OF NANOCORE FORMULATIONS 66		
3.1	Introduction	66
3.2	Materials and Methods	67
3.2.1	Materials.....	67
3.2.2	Surface decoration of nanocore with plasmid DNA	67
3.2.3	Surface decoration of nanocore with quinic acid derivative.....	70
3.2.4	Surface decoration with human serum albumin.....	71
3.3	Results	73
3.3.1	Surface decoration of nanocore with plasmid DNA	73
3.3.2	Surface decoration of nanocore with quinic acid derivative.....	79
3.3.3	Surface decoration of nanocore with human serum albumin.....	81
3.4	Discussion	85
3.4.1	PTX-pTA-pDNA	85
3.4.2	PTX-pTA-QA	87
3.4.3	CFZ-pTA-alb	88
3.5	Conclusion.....	91
3.6	References	92
CHAPTER 4. EVALUATION OF PHARMACODYNAMICS OF ALBUMIN-COATED NANOCORES IN MURINE TUMOR MODELS		
4.1	Introduction	96
4.2	Materials and Methods	97
4.2.1	Materials.....	97
4.2.2	<i>In vitro</i> experiments	97
4.2.3	Systemic administration.....	98
4.2.4	Local administration	100
4.3	Results	102
4.3.1	Antitumor effect and biodistribution with systemic administration	102
4.3.2	Antitumor effect with localized administration	106

4.3.3 Discussion	116
4.3.4 Conclusions	119
4.3.5 References	120
CHAPTER 5. CONCLUSION	124
5.1 Summary	124
5.2 Future studies	125
5.3 References	126
VITA	127
PUBLICATION	128

LIST OF TABLES

Table 1: Particle size, zeta potential and drug content of nanocores (Size and charge measured in 10 mM phosphate buffer, pH 7.4).....	56
Table 2: Molecular weights, solubility and chemical structures of model drugs used.	60

LIST OF FIGURES

- Figure 1: Schematic representation for Ostwald ripening. Reprinted from ref (Sun & Yeo, 2012), Copyright (2012), with permission from Elsevier. 28
- Figure 2: a) Schematic representation of LbL coated NP drug delivery systems, (b) The particle size growth curve of poly-L-lysine/dextran sulfate nanofilms deposited on gold NP (each layer is ~ 2 nm thick), and (c) The ζ -potential of LbL particle show complete reversal of charge after deposition of each poly-L-lysine or dextran sulfate layer. Reprinted with permission from ref (Poon, Lee, Morton, & Hammond, 2011). Copyright (2011) American Chemical Society..... 29
- Figure 3: Schematic representation for the preparation of drug-loaded polymeric NP using FNP. Reprinted with permission from ref (Pustulka et al., 2013). Copyright (2013) American Chemical Society..... 31
- Figure 4: (a) Schematic for the synthesis of NMOF (NCP-1) of Tb^{3+} with disuccinatocisplatin (a cisplatin prodrug), followed by coating with silica shell (NCP-1') and conjugation to cRGDfk (PVP, polyvinylpyrrolidone; TEOS, tetraethylorthosilicate), (b) TEM and (c) SEM images of coated NCP-1'. Adapted with permission from ref (Rieter et al., 2008). Copyright (2008) American Chemical Society. 35
- Figure 5: TA- Fe^{3+} is an efficient tool for coating a variety of substrates. (a) Confocal laser scanning microscopy image of $CaCO_3$ particles (red) coated with TA- Fe^{3+} films (green), (b and c) TEM images of Au NP before (b) and after (c) coating with a TA- Fe^{3+} film, and (d) The dominant TA- Fe^{3+} complexation state depends on pH (R represents the remainder of the TA molecule). From ref (Ejima et al., 2013). Reprinted with permission from AAAS. 49
- Figure 6: (a) Schematic for the general procedure for fabrication of PTX@TA- Fe^{3+} nanoparticles, (b) Morphology of PTX@TA- Fe^{3+} nanoparticles shown by TEM (scale bar 100 nm), (c) TA anchors onto the surface of preformed PTX nanocores via multiple hydrogen binding sites, and (d) Dissipative particle dynamics simulation of the TA assembly process (Middle: bis-complex with tight multilayer structure of TA molecules deposited on the PTX surface, Right: tris-complex with compacted TA aggregates deposited on the PTX surface, Left: mono-complex with TA molecules no longer covering the whole PTX surface, and PTX molecules are exposed to the solvent. Adapted with permission from ref (Shen et al., 2016). Copyright (2016) American Chemical Society. ... 50
- Figure 7: Schematic for preparation of TA/ Fe^{3+} -stabilized nanocore 54
- Figure 8: TEM images of nanocores of different drugs (Scale bar: 100 nm). 56
- Figure 9: TEM image of (a) bare CFZ nanoclusters and (b) core-etched CFZ-pTA (Scale bar: 100 nm). 57
- Figure 10: Colloidal stability of nanocores: Z-average of (a) PTX-pTA and (b) CFZ-pTA nanocores incubated in 50% FBS at 60 $\mu g/mL$ of drug equivalent concentration, measured by DLS at different time points, and (c) TEM image of CFZ-pTA after 24 h incubation in FBS (Scale bar = 100 nm). 57

Figure 11: Co-loading drugs in TA/Fe³⁺-stabilized nanocore: (a) TEM image of PTX-CFZ-pTA and (b) Drug loading capacity and the ratio of PTX and CFZ loading in PTX-CFZ-pTA nanocores at different starting feed ratios. 58

Figure 12: pDNA binding to PTX-pTA surface: (a and h) free pDNA (negative control), (b) BPEI-bound pDNA (positive control), (c-f and i) PTX-pTA mixture with pDNA at different PTX-pTA/pDNA weight ratio as indicated on the gel image below the lanes, and (g) blank pTA without pDNA. (h and i were ran in a separate gel)..... 74

Figure 13: Stability of pDNA binding to PTX-pTA upon challenging: (a) free pDNA (negative control), (b) PTX-pTA-pDNA (unchallenged), (c-h) PTX-pTA-pDNA challenged with heparin (c), DNase and heparin (d), 50% FBS (e), 10 mM PB (f), 5 M urea (g) or saline (h), and (i) 50% FBS (without pDNA) run as a control. 75

Figure 14: Cell interaction of PTX-pTA-pDNA with NCI/ADR-RES: (a) efficient pDNA binding to Nile red labeled PTX*-pTA was confirmed by gel retardation assay (a: free pDNA, b: PTX-pTA, and c: PTX*-pTA, all wells were loaded with 0.2 µg of pDNA), cell interaction was (b) visualized by confocal microscopy imaging of PTX*-pTA, PTX*-pTA-pDNA and free Nile red (negative control), 4 h after incubation with NCI/ADR-RES cells. (Blue= nuclei stained with Hoechst dye and red= nanocores labeled with Nile red) (Scale bar= 50 µm), and (c) quantified by flow cytometry analysis..... 76

Figure 15: Viability of NCI/ADR-RES cells after incubation with PTX-pTA at different PTX-equivalent concentrations (µM) for 4 hours as determined with MTT assay..... 77

Figure 16: *In vitro* transfection of EGFP-expressing pDNA (green) bound to (a) lipofectamine (positive control) or (b) PTX-pTA nanocore, 24 and 48 h after treatment to NCI/ADR-RES cells (treatment was done for 4 h followed by wash and media replacement), imaged by Cytation-3 imaging system. (Scale bar = 300 µm) 78

Figure 17: Quantitative analysis of EGFP expression 48 h after *in vitro* transfection of EGFP-expressing pDNA via lipofectamine (positive control) or PTX-pTA nanocore in NCI/ADR-RES cells (treatment was done for 4 h followed by wash and media replacement), analyzed by flow cytometry. Untreated cells were analyzed as a negative control. 78

Figure 18: Stability of pDNA binding to PTX-pTA in serum-containing RPMI medium and in 100 mM acetate buffer (pH 5): (a) free pDNA (negative control), (b) BPEI-bound pDNA (positive control), (c) BPEI-bound pDNA challenged with complete medium, (d) PTX-pTA-pDNA, (e) PTX-pTA-pDNA challenged with complete medium, (f) complete medium (negative control), (g) PTX-pTA-pDNA challenged with acetate buffer and (h) acetate buffer (negative control). 79

Figure 19: Binding assay of PTX-pTA-QA to mouse recombinant E-selectin immobilized on 96-well ELISA plate: (a) Direct assay, fluorescent (rhodamine-doped) nanocores (0.1 mg/mL) were incubated in the wells for 1 h followed by wash then remaining fluorescence was normalized to initial fluorescence (albumin-coated plate is control for non-specific binding), and (b) Indirect assay (HL-60 binding inhibition assay), nanocores (0.5 mg/mL) were incubated in the wells for 2.5 h, then washed and replaced with HL-60 cells for 2 h, after washing, number of bound HL-60 cells was counted using flow cytometry (PTX-pTA-PEG is negative control). ** indicates p<0.01 vs. control wells (HL-60 treated without prior NP treatment) (one-way ANOVA followed by Tukey's test)..... 81

Figure 20: (a) TEM images of CFZ-pTA-alb (scale bar= 100 nm), (b) SDS-PAGE was replicated two times to confirm albumin content, lanes 1, 2, 3, 4 and 5 are albumin standards of 10, 25, 50, 75 and 100 µg/mL, and (c) size stability of CFZ-pTA-alb after incubation in 50% FBS solution.

..... 82

Figure 21: *In vitro* release kinetics of CFZ-pTA and CFZ-pTA-alb in 10% FBS/RPMI medium.

..... 83

Figure 22: Controlled cytotoxicity as indirect indicator of release stability: (a) Cytotoxicity to HCC-1937 and B16F10 cells after 2 h of direct exposure to free CFZ, CFZ-pTA or CFZ-pTA-alb at equivalent CFZ concentrations, followed by incubation in drug-free medium, (b) cytotoxicity to HCC-1937 and B16F10 cells after 72 h of direct exposure to free CFZ, CFZ-pTA or CFZ-pTA-alb at equivalent CFZ concentrations, and (c) cytotoxicity to B16F10 cells after 72 h of exposure to blank pTA or pTA-alb at concentrations equivalent to their respective percentages in CFZ nanocores (the table shows concentrations of pTA and pTA-alb relative to CFZ concentrations in their corresponding nanocores)..... 84

Figure 23: *In vitro* metabolic stability of CFZ in different formulations after incubation at 37 °C in (a) mouse liver homogenate for 60 min or in (b) whole blood for 30 min. 85

Figure 24: Antitumor activity of CFZ-pTA-alb and CFZ-CD in B16F10@C57BL/6 tumor model after IV injection: (a) Tumor growth curves for individual mice treated with either PBS (n=5), CFZ-CD (n=6) or CFZ-pTA-alb (n=9) at 6 mg/kg of CFZ-equivalent QDx2, and (b) specific tumor growth rate ($\Delta\log V/\Delta t$, V: tumor volume and t: time in days). ***: $p < 0.001$ and ****: $p < 0.0001$, one-way ANOVA with Tukey's multiple comparisons test. 103

Figure 25: Biodistribution of CFZ in major organs 48 h after 2 consecutive doses of CFZ-CD or CFZ-pTA-alb at a dose equivalent to 6 mg/kg*2 of CFZ in B16F10@C57BL/6 (n=4 mice per group). Quantification done using LC-MS/MS. 104

Figure 26: Repeated injections in B16F10@C57BL/6 tumor model. (a) Kaplan–Meier survival curve of mice treated with PBS, CFZ-CD or CFZ-pTA-alb (6 mg/kg CFZ equivalent, QDx2 for 2 weeks), and (b) body weight of treated mice. 105

Figure 27: Blood chemistry 48 h after 2 consecutive doses of PBS, CFZ-CD, CFZ-pTA-alb or blank pTA-alb, at a dose equivalent to 6 mg/kg*2 of CFZ in B16F10@C57BL/6 (n=4 mice per group). (TP: total serum protein, ALB: albumin, GLOB: globulin, ALT: alanine transaminase, ALKP: alkaline phosphatase, GGT: gamma-glutamyl transpeptidase, AMY: amylase, LIPA: lipase, BUN: blood urea nitrogen, CREA: creatinine, TBIL: total bilirubin, Glu: glucose, PHOS: phosphate, CA: calcium, CHOL: cholesterol, NA: sodium, K: potassium, CL: chloride, CO2: carbon dioxide, AGAP: anion gap, and A/G: albumin/globulin ratio). 106

Figure 28: Antitumor activity of CFZ-pTA-alb and CFZ-CD in B16F10@C57BL/6 tumor model after IT injection: (a) Tumor growth curves for individual mice treated once with either PBS (n=4), CFZ-CD (n=5) or CFZ-pTA-alb (n=5) at 1.2 µg CFZ equivalent, (b) specific growth rate of B16F10 tumor ($\Delta\log V/\Delta t$, V: tumor volume and t: time in days), and (c) quantification of tumor infiltrating CD8⁺ T cells using antibody staining and flow cytometry analysis. *: $p < 0.05$ and **: $p < 0.005$ by one-way ANOVA with Tukey's multiple comparisons test. 109

Figure 29: *In vitro* Cytotoxicity of bolus versus sustained CFZ: (a) Schematic for the bolus (cells incubated with different CFZ concentrations for 2.4 h then washed and incubated with drug-free medium for additional 21.6 h) and sustained (cells incubated with different CFZ concentrations for 24 h) exposure regimens, (b) cell viability of B16F10 cells, and (c) cell viability of spleen cells from C57BL/6 mice, after treatment with CFZ (solution in DMSO) in a bolus regimen or sustained regimen. Cell viability measured using MTT assay at the end of 24 h. AUC (area under the curve: dose x exposure time) indicates the total exposure to CFZ over time. 110

Figure 30: *In vitro* DC phagocytosis: B16F10 cells (DiI-labeled) were either non-treated or treated with blank pTA-alb, CFZ solution or CFZ-pTA-alb (at 10 μ M CFZ equivalent) for 4 h, followed by wash and coculture with BMDCs for 4 h. BMDCs were labeled with APC anti-mouse CD11c antibody and analyzed with flow cytometry. Percentage DC phagocytosis, quantified as the percentage of DiI⁺/CD11c⁺ cells among the CD11c⁺ cells. **: $p < 0.005$ and ****: $p < 0.0001$ by one-way ANOVA with Tukey's multiple comparisons test. 110

Figure 31: Retention of CFZ formulations in tumor after IT injection: (a) Amount of CFZ in tumor tissue 2 h following IT injection of CFZ-CD (n=4) or CFZ-pTA-alb (n=4) at 1.2 μ g CFZ equivalent, and (b) CFZ concentration in plasma collected at mice sacrifice. Quantification done using LC-MS/MS. *: $p < 0.05$ and **: $p < 0.01$, unpaired two-tailed *t*-test. 111

Figure 32: Levels of IFN- γ secretion from splenic T cells upon stimulation with irradiated B16F10 lysate (relative to unstimulated control cells), following single IT injection in B16F10@C57BL/6 tumor model with either PBS (n=4), CFZ-CD (n=5) or CFZ-pTA-alb (n=4) at 1.2 μ g CFZ equivalent. 112

Figure 33: Antitumor activity of CFZ-pTA-alb and CFZ-CD in CT26@Balb/c tumor model after IT injection: (a) Tumor growth curves for individual mice treated once with either PBS (n=3), CFZ-CD (n=3) or CFZ-pTA-alb (n=4) at 1.2 μ g CFZ equivalent, and (b) specific growth rate of CT26 tumor ($\Delta \log V / \Delta t$, V: tumor volume and t: time in days). *: $p < 0.05$ and **: $p < 0.005$ by one-way ANOVA with Tukey's multiple comparisons test. 113

Figure 34: Evaluation of abscopal effect with simultaneous tumor inoculation. (a) Balb/c mice were inoculated with 300,000 and 100,000 CT26 on the right and left hind limb, respectively, on the same day. Right tumors (tumor A) reaching 50 mm³ were treated once with 60 μ g CFZ-equivalent CFZ-pTA-alb or PBS (n=4 per group). (b) Growth curves for treated (tumor A) and non-treated (tumor B) tumors in all mice collectively, and (c and d) individual tumor growth curves for each mouse receiving (c) PBS or (d) CFZ-pTA-alb. 114

Figure 35: Evaluation of abscopal effect with separated tumor inoculation. (a) Balb/c mice were inoculated with 300,000 CT26 cells on the right hind limb followed by 100,000 CT26 cells on the left hind limb 7 days later. Right tumors (tumor A) reaching 50 mm³ were treated once with 60 μ g CFZ-equivalent CFZ-pTA-alb, CFZ-CD or PBS (n=5 per group). (b) Growth curves for treated (tumor A) tumors. (c and d) Tumor-specific immunity: (c) spleen or (d) DLN cells from mice sacrificed on day 22 post-treatment were challenged with AH1 peptide and IFN- γ secretion was measured using ELISA kit (IFN- γ secretion is presented relative to basal secretion of non-challenged cells). *: $p < 0.05$ by one-way ANOVA with Tukey's multiple comparisons test... 115

ABSTRACT

Author: Taha, Maie, S. PhD

Institution: Purdue University

Degree Received: May 2019

Title: Development of Nanoparticles with High Drug Loading Capacity and Stability

Committee Chair: Yoon Yeo

Many anti-cancer drugs are poorly water-soluble and show undesirable pharmacokinetics and low bioavailability. Nanoparticles (NP) are used as delivery vehicles to improve bioavailability and biodistribution of such drugs. For clinical translation of an NP product, it is critical that the NP carry a large amount of drug and maintain good stability during circulation. A typical drug loading capacity of current NP formulations is less than 20% of the total mass, which is concerning from the standpoint of safety and administration convenience. Current NP formulations are also limited in retaining a drug during circulation and release the drug prematurely before they reach target tissues. These challenges are responsible at least partly for recent failure of leading NP products in clinical trials.

Given these challenges, I have focused on developing a stable NP formulation with high drug loading capacity, drug-rich nanocores stabilized by interfacial assemblies of iron-tannic acid (pTA) and albumin. Tannic acid is a polyphenol of natural origin and can form coordination complexes with Fe^{3+} ions that stabilize the interface between drug rich core droplets and aqueous solution. The underlying hypotheses are that (i) NP core formed solely of drug will offer a high drug loading capacity and (ii) the strong interaction of TA with drug molecules will maintain the nanocore stability and avoid premature drug release. Carfilzomib (CFZ), an epoxyketone peptide and a second-generation proteasome inhibitor, the use of which is limited to multiple myeloma due to the low stability, was chosen as a model drug to encapsulate in the new NP formulation. The NP surface was further functionalized with albumin, quinic acid derivative and plasmid DNA based on their affinity for TA complex. With an additional albumin coating, CFZ nanocore (CFZ-pTA-alb) showed sustained drug release and metabolic stability. In murine syngeneic model of B16F10 melanoma, systemically administered CFZ-pTA-alb showed enhanced biodistribution and anti-tumor effect than commercial cyclodextrin-based CFZ (CFZ-CD). With localized intratumoral administration, CFZ-pTA-alb also outperformed CFZ-CD in antitumor efficacy,

potentially by prolonged drug retention, reduced damage to tumor-infiltrating lymphocytes, and enhanced delivery of tumor antigens to DCs.

CHAPTER 1. INTRODUCTION

1.1 Nanoparticles for systemic drug delivery

In the past few decades, nanoparticles (NP) have been used as a way of systemic delivery of drugs. In particular, the use of NP for delivering chemotherapeutic agents to solid tumors has received considerable attention. Organic nanoparticles are prepared of lipids or biodegradable polymers with a diameter ranging from 10 nm to 1 μm (Allouche, 2013). A large array of organic materials has been used to load chemotherapeutic drugs into NP offering additional functionalities. The unique size range and large customizable surface (relative to volume) enable NP to improve drug performance upon intravenous (IV) injection by the following mechanisms (Li & Huang, 2008): (i) Drugs carried by NP are protected from renal clearance owing to the particle size greater than the renal clearance cut-off (5.5 nm) (Choi et al., 2007). (ii) NP-carried drugs are also protected from metabolizing enzymes in the liver and circulation. The stability against degradation is particularly important for chemically and/or metabolically labile molecules such as proteins, peptides and nucleic acids (Singh & Lillard, 2009). Consequently, NP can increase the half-life of a drug and improve drug accumulation at the target site (Li & Huang, 2008). (iii) Moreover, NP access tumors with leaky vasculature and impaired lymphatic drainage via the Enhanced permeability and Retention (EPR) phenomenon (Matsumura & Maeda, 1986), unlike free drug molecules that enter tissues by diffusion across the blood capillaries causing off-target side effects, resulting in higher specific bioavailability and reduced nonspecific drug toxicity (Brannon-Peppas & Blanchette, 2004). (iv) In delivery of hydrophobic drugs, NP can serve as a safe alternative to organic solvents or surfactants that generally have systemic toxicities (Singh & Lillard, 2009). (v) Also, NP can be engineered to release its payload in a controlled rate and maintain the drug concentration within a therapeutic window (Malam, Loizidou, & Seifalian, 2009). (vi) The surface of NP can be modified with various polymers and ligands for prolonging NP circulation and target-specific NP delivery (Banerjee & Sengupta, 2011). For example, PEGylated “Stealth” NP have shown to improve pharmacokinetics than their bare NP counterparts. PEG helps to avoid opsonization of NP by serum proteins to their surfaces and subsequent uptake by the reticuloendothelial system (RES), thereby allowing NP to circulate for a longer period of time in the body (Li & Huang, 2010). (vii) Drug-loaded NP can help overcome multiple drug resistance

(MDR), a major challenge for many chemotherapeutics (Cho, Wang, Nie, Chen, & Shin, 2008). One of the main mediators of MDR is P-glycoprotein efflux pumps, which are overexpressed in tumor cells and interfere with intracellular delivery of a chemotherapeutic drug. NP can bypass P-glycoprotein and enter the cells via receptor-mediated endocytosis, thus increasing intracellular drug concentrations (Brigger, Dubernet, & Couvreur, 2002). (viii) NP are also used for incorporating diagnostic agents and simultaneous loading of multiple drugs (Rocca, Liu, & Lin, 2012) for real-time tracking of the administered systems in the body and synergistic combination therapies, respectively.

1.2 Limitations of current NP systems

Despite the potential advantages of NP and years of research, NP has not shown much clinical success (Rocca et al., 2012). While each NP system may have different issues, drug loading capacity, colloidal stability and drug encapsulation stability in circulation, and spatiotemporal release of the payload are considered critical challenges to successful NP development (Bae & Park, 2011).

1.2.1 Drug loading capacity

It is important to define drug loading capacity versus encapsulation efficiency, which are often interchangeably used in the literature. Inaccurate definition of drug loading capacity creates confusion in interpreting literature data. Drug loading capacity (or drug content) is the ratio of drug mass to total mass of the prepared NP, whereas encapsulation efficiency indicates the ratio of drug encapsulated in NP per total drug feed during the preparation procedure. High encapsulation efficiency is important from the economics standpoint because it means cost-effective production of NP. High drug loading capacity is important in the context of therapeutic efficacy. A typical NP drug loading capacity is less than 20 %w/w of the total NP mass (Wilhelm et al., 2016). Low drug content means that a large amount of NP need to be administered to achieve a therapeutic dose. This incurs an increase in the injection volume and/or NP concentration, which are technically and clinically challenging (Wilhelm et al., 2016). Large injection volume necessitates a long-term infusion and increases medical costs. High NP concentration compromises colloidal stability of NP, potentially resulting in irreversible particle aggregation. Aggregated NP are prone to the RES removal (Alexis, Pridgen, Molnar, & Farokhzad, 2008). A large amount of NP also means an

introduction of a lot of excipients to the patient's body. Despite careful choice of excipients used in NP preparations, their biological effects and toxicities due to long term exposure may not be well predicted (Laine, Hossain, Solis, & Adams, 1995). Given that >90% of drug and excipients eventually interact with off-target tissues, the safety of excipients can never be underestimated (Wilhelm et al., 2016). In addition, the large amount of NP needed per dosing necessitates a large scale production of NP, increasing the challenges in scale-up and quality control such as size distribution and batch-to-batch variability (Rocca et al., 2012; Wilhelm et al., 2016).

1.2.2 Circulation stability

NP need to circulate long enough to locate tumors and extravasate into the tumors. For the NP to modify biodistribution of a drug, it is important that they remain stable during the circulation. NP may encounter different forms of instability in circulation: they may lose colloidal stability to form aggregates and/or release drug prematurely in blood stream (K. C. Liu & Yeo, 2014). Aggregated NP are readily removed by RES resulting in decreased drug bioavailability. Mohr *et al.* (Mohr et al., 2014) prepared polystyrene NP with different surface functionalization so that they aggregated differently in presence of serum proteins. They examined the *in vivo* distribution of the different NP and showed that aggregating NP localized mainly in the liver, while non-aggregating NP distributed to all organs.

NP unable to retain drug during circulation will reach the tumor empty, failing to make difference from free drug in therapeutic efficacy. An anticancer drug, carfilzomib, encapsulated in polymeric micelles composed of polyethylene glycol and poly(caprolactone) block copolymers had high metabolic stability and cytotoxic activity *in vitro* (Ao et al., 2015). Upon IV injection into mice bearing a lung cancer xenograft, the micelle formulation however did not show better anticancer efficacy compared to the drug solution (Park et al., 2017). This can be explained by the instability of micelles in circulation releasing the drug rapidly, as evidenced by the lack of difference in pharmacokinetic profiles between micelles and drug solution formulations. Similar stability problem is seen with paclitaxel commercial NP, Abraxane®, composed of paclitaxel bound to human serum albumin (Desai, 2008). Abraxane® forms NP of 130 nm in saline, but in blood it rapidly dissociates into paclitaxel-albumin complexes with the same size as endogenous albumin molecules (Desai, 2008). Although Abraxane® avoids the vehicle-related toxicity of

Taxol® (a surfactant-based formulation), it does not improve the circulation kinetics of the drug (Hamaguchi et al., 2007; Miele, Spinelli, Miele, Tomao, & Tomao, 2009).

1.2.3 Drug release kinetics

For NP to successfully accumulate their payload at the intended target site they should have controlled drug release rate. Typically, circulating NP take 24 to 48 h to reach solid tumors via the EPR effect (Iyer, Khaled, Fang, & Maeda, 2006). Therefore, sustained or tumor-responsive drug release are needed to minimize drug leakage to the systemic circulation. In addition, NP at the tumor site should release the drug in a timely manner to give therapeutic effect according to the purpose or mode of action. For example, Doxil®, a liposomal formulation of doxorubicin, effectively carries the drug to the tumor but fails to show increased efficacy (Ellerhorst et al., 1999; Garcia, Kempf, Rogers, & Muggia, 1998). This is attributed to the highly stable drug retention both in circulation and at the tumor site (Andresen, Jensen, & Jørgensen, 2005). On the other hand, an NP formulation with sustained drug release might be beneficial in mimicking the metronomic chemotherapy schedules. Metronomic regimens refer to the frequent or prolonged administration of chemotherapeutics at much lower doses than those used in maximum tolerated doses (MTDs) regimens (Kareva, Waxman, & Lakka Klement, 2015). MTDs selectively target chemo-sensitive cancer cells, leaving behind chemo-resistant populations that might lead to tumor relapse and emergence of drug resistance (Shah, Rejniak, & Gevertz, 2016). On the contrary, metronomic chemotherapy targets the tumor microenvironment, disengaging the tumor from its support system and resulting in long lasting tumor regression. Sustained low doses of chemotherapeutics results in profound antiangiogenic effects (Browder et al., 2000; Klement et al., 2000), activate the antitumor immunity without killing the immune cells recruited to the tumor (Banissi, Ghiringhelli, Chen, & Carpentier, 2009; Ghiringhelli et al., 2007), and avoids the induction of tumor-initiating cancer stem cells (T.-S. Chan et al., 2016). One study reports that topotecan treated to tumor-endothelial spheroids in fractionated doses, to mimic the metronomic chemotherapy, was more effective in reducing the spheroid size than the bolus dose given once (Jyoti et al., 2015). More interestingly, topotecan encapsulated in a liposomal formulation that offered sustained release rate, was found as effective as the fractionated doses. Therefore, an NP formulation designed with a balance between sustained drug release and bioavailability at the site of action can achieve the full potential of enhanced pharmacokinetics and pharmacodynamics.

1.3 Achieving nanoparticles with high drug loading and circulation stability

An NP formulation with high drug loading, colloidal stability and stable drug retention in circulation and at the tumor site can overcome the above-mentioned limitations of current NP-therapeutics. Increasing the drug loading in a NP will reduce the total NP dose and the amount of excipients to be administered, decreasing safety issues and manufacturing cost. A NP with high circulation stability can alter pharmacokinetics of a drug and increase its deposition in target tissues (Rocca et al., 2012). With these improvements, one may expect that NP can increase the efficiency of drug delivery to tumors beyond the level currently possible (~1% of the injected NP ending in the tumor) (Wilhelm et al., 2016).

1.3.1 Factors affecting drug loading in NP

1.3.1.1 Drug-polymer compatibility

Drug loading capacity of NP depends largely on the type and strength of interaction between the drug and polymer used in NP preparation, such as hydrogen bonding, electrostatic or hydrophobic interactions or polymer-ion coordination (X. Xu, Shan, & Pan, 2016). For example, a hydrophobic drug, mitoxantrone, was encapsulated in cholesterol-modified pullulan polymer and the drug loading capacity was found to be proportional to the degree of cholesterol substitution (4.45% with 3.11 substitution degree to 10.1% with 6.91 substitution degree) (Xiaojun Tao et al., 2016). This result was attributed to increased hydrophobic interactions between the aromatic structure of mitoxantrone and cholesterol. However, when the cholesterol was modified with carboxyethyl group, drug loading was lower (4.25%) than the formulation with unmodified cholesterol irrespective of the substitution degree. This shows that structural changes of polymers reduce the drug-polymer interaction, thereby drug loading capacity. NP systems with efficient drug loading rely on multiple modes of drug-polymer interactions (J. O. Kim, Kabanov, & Bronich, 2009; X. Xu et al., 2016).

Polymers with high molecular weights are usually chosen for NP preparation as they show relatively slow degradation rate and good control of drug release kinetics (Diab, Jaafar-Maalej, Fessi, & Maincent, 2012). Polymer composition needs to be optimized to get efficient drug loading. For example, theophylline was encapsulated in polyalkylcyanoacrylate NP, and the drug loading capacity was shown to increase with the monomer concentration (Radwan, 1995). Polymer crystallinity also affects drug loading capacity in micellar NP systems. Highly crystalline polymers

tightly pack within the micelle cores and hinder efficient drug incorporation, whereas amorphous regions of the core can better accommodate drug molecules (Shuai, Ai, Nasongkla, Kim, & Gao, 2004). Core crystallinity can be controlled by varying the building blocks in the copolymer and disrupting the crystalline order (Glavas, Olsén, Odelius, & Albertsson, 2013).

1.3.1.2 Drug loading approaches

Drug can be loaded in NP by (i) incorporation (drug is added during NP preparation and included within the NP matrix), (ii) adsorption/absorption (preformed NP are incubated in drug solution so that the drug adsorbs on the NP surface or gets absorbed in its core), and (iii) drug conjugation (drug is chemically conjugated to the polymer used for NP preparation) (Singh & Lillard, 2009; Soppimath, Aminabhavi, Kulkarni, & Rudzinski, 2001).

Typically, drug incorporation achieves higher drug loadings than the adsorption method (Radwan, 1995; Soppimath et al., 2001; Wilhelm et al., 2016). However, it also depends on the type of interaction between the loaded molecules and the polymers. For example, ovalbumin was either encapsulated in hydrophobic PLGA core of (3β -[N-(N',N'-Dimethylaminoethane)-carbamoyl] cholesterol hydrochloride, DC-Chol)-PLGA NP or adsorbed to the cholesterol surface via hydrophobic and charge interactions (L. Liu et al., 2016). The loading capacity of the encapsulated protein was 2.42% whereas that of the adsorbed protein was 2.87%. Moreover, small NP (and thus large surface area relative to the volume) show relatively high adsorption capacity (Kufleitner, Wagner, Worek, von Briesen, & Kreuter, 2010). Drug adsorbed to NP surface may not be well retained. However, it is desirable for the drugs that cannot tolerate harsh conditions such as heat or organic solvents, which are typically needed in drug encapsulation in the NP, for indications requiring rapid drug release, such as antidote therapy (Kufleitner et al., 2010) or for induction of quick immune responses (O'Hagan et al., 2001). Drug molecules can also be covalently conjugated to NP surface or to the polymer prior to NP preparation (Cholkar, Acharya, Trinh, & Singh, 2017; Dragojevic, Ryu, & Raucher, 2015; Khandare, Calderon, Dagia, & Haag, 2012). Drug-polymer conjugation is a good strategy for loading water soluble molecules (Soppimath et al., 2001). Doxorubicin, a water soluble anticancer drug, conjugated to the PLGA chain was loaded in PLGA-PEG micelles with a loading content of 2.18% (compared to 0.51% with free drug physically loaded in micelles) (Yoo & Park, 2001). In this case, free drug easily

escaped to the aqueous medium, whereas the PLGA-conjugated doxorubicin was forced to stay in the core during the copolymer assembly.

1.3.2 Factors affecting NP colloidal stability in circulation

1.3.2.1 Physicochemical properties of NP

The hydrophobicity and surface charge of NP have key roles in determining the NP colloidal stability in aqueous suspension by dictating the interparticle interactions. According to the Derjaguin–Landau–Verwey–Overbeek (DLVO) theory, the interaction between particles is a net result of van der Waals forces and electric double layer interaction (Chen, Smith, Ball, & Fairbrother, 2010). Van der Waals forces are attractive forces resulting from interactions between dipoles, induced or permanent, at the particles surface. On the contrary, electric double layer interactions are repulsive forces between similar charges on the NP surface and those tend to stabilize the colloidal system. The surface charge, sign and magnitude, depends on the NP composition and originates from ionizable or dissociable surface groups. Typically, as the surface charge of NP increases, the colloidal stability in aqueous suspension increases. For NP with amphoteric surface, the pH of the suspension determines the particles stability. At pHs near the isoelectric point (pH at which the charge becomes zero) the NP surface becomes almost neutral and particles tend to aggregate due to dominating van der Waals forces (Moore et al., 2015). Also, as the ionic strength of the suspension increases, counter ions compacts the electric double layer leading to loss of the repulsive forces and particles aggregation.

Macromolecules or polymers grafted or adsorbed to the NP surface can enhance the NP colloidal stability (Lourenco, Teixeira, Simões, & Gaspar, 1996). Nonionic polymers provide steric stabilization effect via their interpenetrating hydrophilic portions projecting to the solution phase avoiding the van der Waals attractive forces (Napper, 1977). This effect depends on the molecular weight, density and uniformity of polymer coating (Studart, Amstad, & Gauckler, 2007). Polymers with very high molecular weight, low concentration or non-uniform surface coating can rather lead to particle aggregation by bridging effect (Hogg, 2013) (McFarlane, Wagner, Kaler, & Lynch, 2010). Surface coating with charged macromolecules/polymers results in electrostatic repulsion forces in addition to the steric effect known as electrosteric stabilization. However, the pH and ionic strength of the suspension can affect the conformation of the surface polymer and the overall surface charge (Hotze, Phenrat, & Lowry, 2010).

According to the DLVO theory, colloidal stability should increase with increasing particle size due to increased surface repulsive forces (Wiese & Healy, 1970). However, some studies have shown either an opposite trend, with NP stability decreasing as size increases (Tsuruta, Lessa, & Carmona-Ribeiro, 1995) or no difference in stability with varying sizes (Elimelech & O'Melia, 1990).

1.3.2.2 Interaction with blood components in circulation

NP that show colloidal stability in aqueous suspensions can behave differently when introduced into circulation. Human blood has a complex mixture of proteins, lipids, amino acids, electrolytes and cells that interact with NP (Moore et al., 2015) (Lazzari et al., 2012). Adsorption of proteins and lipoproteins to the surface of NP forming a corona is largely dependent on the surface properties of NP. Serum proteins, mostly negatively charged, are known to adsorb strongly to positively charged NP (Jiang et al., 2006). Most importantly, the composition of the protein corona varies with the surface charge and composition affecting the colloidal stability. For example, polystyrene NP were functionalized with either non-ionic (PS-LUT), amine-modified (PS-LUT-NH₂) or carboxy-modified (PS-LUT-COOH) lutensol AT50, or with the anionic surfactant sodium dodecyl sulfate (PS-SDS) (Mohr et al., 2014). All particles showed similar size and polydispersity index in water. However, in human serum they aggregated differently, which was attributed to the different protein corona formation as analyzed using LC-MS. NP with slightly (PS-LUT) or highly (PS-LUT-COOH) negative surface charge underwent aggregation due to protein corona enriched with lipoproteins and coagulation proteins, respectively. In contrast, the slightly positively charged lutensol-stabilized NP (PS-LUT-NH₂) did not aggregate although they had similar protein adsorption profile as PS-LUT. This indicates that even with a similar protein corona, the surface charge and composition can still dictate the colloidal stability of NP. In addition, PS-SDS showed the highest aggregation state and this correlated with the highest protein adsorption particularly immunoglobulins, which may have caused particles bridging.

Geometry and roughness of NP also influences protein adsorption. The NP shape affects its curvature and surface area available for contact with proteins and roughness decrease the protein adsorption affinity. In one study, mesoporous silica nanoparticles with different shapes (spheres vs rod) and pore sizes were prepared, and the adsorption of serum proteins was evaluated (Ma, Bai, Wang, & Jiang, 2014). The binding rate of human serum albumin and globulin was lower for the

spherical particles with large pores and for the rod particles than spherical particles with small pores which had higher curvature. On the other hand, the binding rate of fibrinogen with rod-shape structure was highest to the rod-shaped particles, due to enhanced contact. Moreover, the conformation of the adsorbed proteins was affected upon contact with particles. The rod-shaped fibrinogen bended to adjust the surface curvature and thus lost some of its secondary structure, while the rigid globulin was not affected. In addition, proteins adsorb better to hydrophobic NP surfaces than hydrophilic ones (H. Gao & He, 2014). Other than the protein adsorption, electrolytes in the blood affect the NP colloidal stability by interfering with the electrostatic interactions (Picola et al., 2013).

1.3.3 Factors affecting drug release rate from NP

1.3.3.1 Drug and polymer properties

Drugs with high aqueous solubility show higher release rate than those with poor solubility. While doxorubicin is relatively water-soluble drug, its loading in liposomes via formation of sulfate salts decreases its solubility to a high extent and retards its drug release (Haran, Cohen, Bar, & Barenholz, 1993). In one study, doxorubicin loaded in liposomes either as phosphate or sulfate salts had differential release rate profiles (Fritze, Hens, Kimpfler, Schubert, & Peschka-Süss, 2006). At low pH, the phosphate salt showed higher release rate than the sulfate salt owing to higher solubility of the former.

Polymers with high crystallinity have reduced water permeability and chain mobility which retards the drug release from NP (Weinkauf & Paul, 1990) (Karavelidis, Karavas, Giliopoulos, Papadimitriou, & Bikiaris, 2011). Polymer hydrophobicity also affects its solubility and degradation rate. The release extent and rate of 5-fluorouracil from BPLP-co-PLGA NP with 50/50 lactide/glycolide ratio were much higher than that from BPLP-co-PLGA NP with 75/25 ratio (Hu et al., 2016). This was explained by the relatively high percentage of the hydrophobic lactide in BPLP-co-PLGA 75/25, leading to slow polymer hydration and thus slow hydrolysis and degradation. The mechanical strength of polymer can affect the drug release rate by affecting the tortuosity of the NP matrix (Kamaly, Yameen, Wu, & Farokhzad, 2016). Higher molecular weight polymers have lower elastic modulus and result in less-deformable matrices. On the other hand, polymers of low molecular weight form NP with deformable structure whose pores can connect to create channels under osmotic pressure and facilitate the release of incorporated drug molecules

(Saltzman, 2001). For liposomal formulations, lipid fluidity affects drug release rate. For example, cisplatin was loaded in liposomes prepared with phosphatidylcholines of varying phase transition temperatures (T_m) to evaluate *in vitro* cytotoxicity as well as pharmacokinetic analysis following IV administration in mice (Alavizadeh, Badiie, Golmohammadzadeh, & Jaafari, 2014). It was shown that the liposomes with lower T_m values had higher cytotoxicity and faster clearance from the circulation, which was attributed to higher cisplatin release with increased bilayer fluidity.

1.3.3.2 Drug loading and NP system properties

The drug release kinetics also depends on the way the drug is loaded in NP. Drugs adsorbed to NP surface will be governed by the drug desorption rate. For drugs entrapped within NP matrix, release will be governed either by drug diffusion or matrix degradation or both (Aguilar, 2013). In many polymeric NP systems, a large fraction of the loaded drug might be bound on the surface rather than entrapped inside the matrix. This results in high initial burst release of the drug due to easy desorption of the surface bound molecules (X.-Y. Lu, Wu, Li, & Chen, 2011). Crosslinking of the polymer forming the NP can retard the polymer's erosion and degradation; however, it may not control the diffusion of the physically entrapped drug. Core-crosslinked polymeric micelles prepared with mPEG-poly(N-(2-hydroxypropyl)methacrylamide) polymer circulated longer and had better tumor accumulation than the non-crosslinked ones owing to retarded core degradation upon crosslinking (Rijcken Cristianne, Talelli, van Nostrum Cornelus, Storm, & Hennink Wim, 2010). However, the drug-loaded crosslinked micelles showed burst release *in vitro* due to rapid drug diffusion that was not controlled by core crosslinking. On the other hand, chemical conjugation of drugs to the polymer forming the NP minimizes the burst release and usually offers sustained drug release, the rate of which is controlled by the cleavage of the conjugate (Crielaard et al., 2012) (Tong & Cheng, 2008). For liposomal formulations, the lipid concentration affects the drug loading and thus the drug release rate. Higher lipid/drug ratio forms liposomes with less drug loading capacity, which creates low concentration gradient of drug across the lipid membrane, hence slow drug release rate (Tsukamoto et al., 2013).

Coating the NP surface with polymers or lipids can control drug release given the interaction between the coat material and the drug retards the drug diffusion. Human serum albumin complexed on the surface of mitoxantrone-loaded pullulan NP offered steric hindrance and high binding affinity for mitoxantrone, delaying drug release (X. Tao et al., 2012). Similarly,

docetaxel-loaded PLGA NP coated by lecithin and DSPE showed attenuated drug release rate due to the lipid monolayer (L. Zhang et al., 2008).

Particle size might also affect the drug release profile. Smaller particles have larger surface area to volume ratio; therefore, entrapped drugs are closer to the surface and have higher rate of diffusion (Singh & Lillard, 2009). On the other hand, larger PLGA NP degraded faster due to a longer diffusion path of degradation products to the NP surface (Dunne, Corrigan, & Ramtoola, 2000). The long presence of degradation products within the matrix results in auto-catalytic degradation of the rest of the polymer. The effect of particle size was also seen with liposomes, where the drug (DB-67) encapsulated in liposomes of 103 nm released faster than from 146 nm liposomes of same composition (Liang, 2010).

1.3.4 New approaches for preparation of NP with high drug loading capacity and circulation stability

With the conventional NP preparation methods, low drug loading remains an issue despite various efforts to optimize formulation variables and types of polymers. Therefore, new formulation strategies have been explored to increase the drug loading capacity.

1.3.4.1 Drug Nanocrystals

Drug nanocrystals provide the highest possible drug content because almost the entire mass is the drug (Rocca et al., 2012). There are two methods for producing nanocrystals: bottom-up or top-down. In the bottom-up approach, drug molecules dissolved in organic solvents are precipitated into small particles in the nanometer size range. This is performed by adding an anti-solvent that is miscible with the drug solution but does not dissolve the drug. Here, nanoprecipitation using supercritical fluids, controlled rate of solvent evaporation, ultrasonic waves, spray drying or electro-spraying are used to induce drug nucleation (H.-K. Chan & Kwok, 2011). In top-down approach, large drug particles are broken down to small nanocrystals by wet milling or high-pressure homogenization with microfluidization or piston-gap homogenizers, which generates high shear stresses (Keck & Müller, 2006). Combinations of both bottom-up/top-down techniques are also used: for example, anti-solvent precipitation is used to produce large drug particles, which are then broken down to the nanometer size range by high pressure homogenization (Kipp, Joseph, Doty, & Rebbeck, 2001).

Nanocrystals may be desirable as they exclude excipients that can bring biological activities or immunological reactions (Kasai et al., 2012). However, in most cases nanocrystals with high surface energy can aggregate in biological media with high concentration of proteins and ions (L. Zhao, Shen, Ma, & Yan, 2017). Therefore, surface stabilization is typically needed. Charged surfactants such as sodium lauryl sulfate and sodium cholate coating can keep them separated by electrostatic repulsion. Non-ionic surfactants and polymeric stabilizers such as Pluronics, Polysorbates and polyvinyl alcohol are also used to provide steric hindrance against aggregation (Van Eerdenbrugh, Van den Mooter, & Augustijns, 2008). In addition, the surface of nanocrystals might need coating with protective polymers such as polyethylene glycol (PEG) to avoid opsonin binding and recognition by the RES (H. Zhang, Hu, Dai, Wang, & Zhang, 2015). This will provide prolonged circulation of the nanocrystals and facilitate tumor accumulation by the EPR effect. Cell specific ligands can be used in a minor fraction to decorate nanocrystal surface for targeted drug delivery (J. Xu et al., 2017) without affecting the drug loading (Fuhrmann, Gauthier, & Leroux, 2014).

One limitation of nanocrystal development is the size control. In order to take advantage of the leaky tumor vasculature the crystal size should be kept below 200 nm (Blanco, Shen, & Ferrari, 2015). Precise process control is required to achieve small, homogenous and reproducible particle size. Stability in circulation is another problem. Nanocrystals can either dissolve quickly in blood or aggregate over time. The rapid dissolution of nanocrystals can be predicted in a sink condition (L. Gao et al., 2011). When this happens, nanocrystals will dissolve before they circulate long enough to enable passive targeting and/or lose their surface ligands (Fuhrmann et al., 2014). Nanocrystals of drugs with solubility in the order of mg/mL are likely to face this problem (Merisko-Liversidge, Liversidge, & Cooper, 2003). Nanocrystals of drugs with intrinsic solubility in $\mu\text{g/mL}$ may take longer to dissolve depending on the dose (i.e. initial concentration in blood), due to poor local mixing upon injection and small initial volume of distribution (Y. Lu, Chen, Gemeinhart, Wu, & Li, 2015). Nanocrystals can grow in size by the phenomenon known as Ostwald ripening, where small crystals dissolve gradually and recrystallize into larger ones (Figure 1) (Y. Liu, Kathan, Saad, & Prud'homme, 2007).

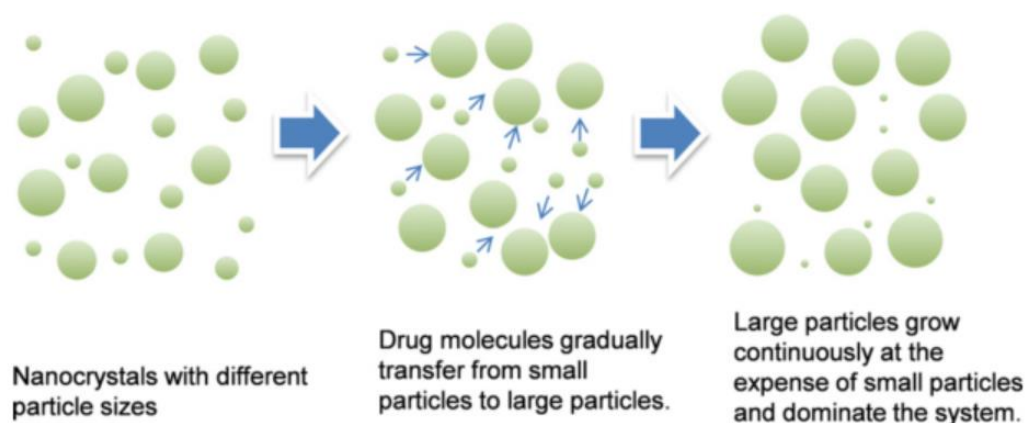


Figure 1: Schematic representation for Ostwald ripening. Reprinted from ref (Sun & Yeo, 2012), Copyright (2012), with permission from Elsevier.

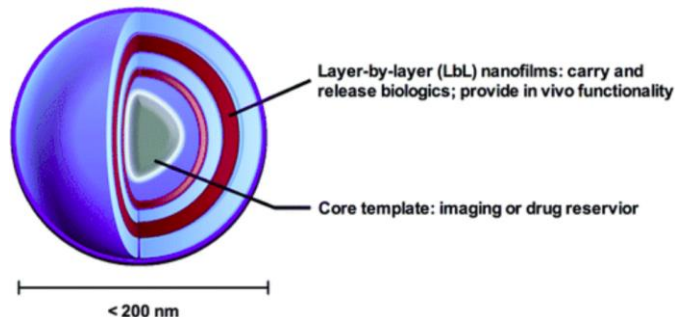
This agglomeration can occur in biological conditions due to the gradual shedding of the surface stabilizers and will reduce the bioavailability of the drug (Sun & Yeo, 2012). The erosion of surface stabilizers and polymers is likely due to the weak and dynamic nature of binding (Shen et al., 2016). A premature shedding of surface-bound targeting ligands can also reduce the targeting efficiency of nanocrystals (Sun & Yeo, 2012). Therefore, efforts are made to avoid the shedding of stabilizers and ligands from the nanocrystals surface and subsequent alteration in their biodistribution and pharmacokinetics. Surface stabilizers were chemically modified to possess greater affinity for the hydrophobic crystal surface (Fuhrmann et al., 2013). Alkane groups of different lengths and structures have been added to the polyester block of a copolymer via click chemistry and used to stabilize paclitaxel nanocrystals. Size stability of the formed nanocrystals depended on the branching of alkane groups and the number of branches. Another approach is to crosslink the polymer to the nanocrystal surface. Paclitaxel nanocrystals stabilized with chitosan were prepared by nano-comminution of the drug and polymer mixture using zirconia beads. Chitosan on the surface was then crosslinked with tripolyphosphate and further conjugated to folic acid as a targeting moiety (S. Kim & Lee, 2011). Although *in vivo* results are not available, *in vitro* release study shows that the crosslinking step significantly delayed the dissolution of nanocrystals (Fuhrmann et al., 2014).

1.3.4.2 Layer-by-layer assemblies

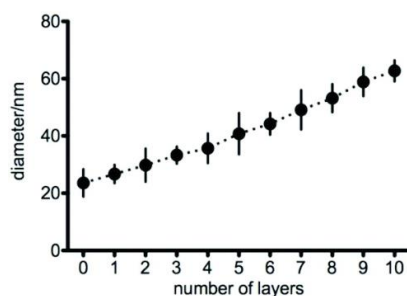
Layer-by-layer (LbL) assembly refers to sequential deposition of oppositely charged polyelectrolytes on a surface, forming a multi-layered film of few nanometers thickness.

Electrostatic binding is the main interaction between the alternating species, but hydrophobic interactions, hydrogen and covalent bonding are also reported (Such, Johnston, & Caruso, 2011). Due to the multitude of interactions, different kinds of polymers, macromolecules, nanoparticles and even cells have been coated on substrates by the LbL techniques (Richardson et al., 2016). Although this method of film deposition was initially proposed for planar substrates (Decher, Hong, & Schmitt, 1992), it has been later implemented for coating of solid drug particles for drug delivery (Caruso, Trau, Möhwald, & Renneberg, 2000; Qiu, Leporatti, Donath, & Möhwald, 2001). It has been shown that particulate systems of different sizes and dimensions can be coated by LbL technique as long as they have the basis of interactions for the first deposited layer (Hammond, 2012). A key feature of LbL assembly is that it is possible to fine-tune the properties of the resulting system by changing the composition and the number of assembled layers as well as the conditions during and post-assembly (such as pH and ionic strength to modulate their permeability) (Figure 2) (Richardson et al., 2016; Such et al., 2011). In addition, the LbL assembly is generally performed in mild aqueous conditions and, thus, suitable for processes involving sensitive proteins and macromolecules (Hammond, 2012).

(a)



(b)



(c)

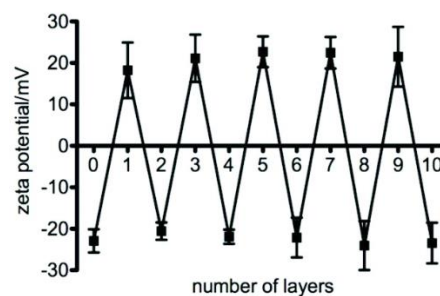


Figure 2: a) Schematic representation of LbL coated NP drug delivery systems, (b) The particle size growth curve of poly-L-lysine/dextran sulfate nanofilms deposited on gold NP (each layer is ~ 2 nm thick), and (c) The ζ -potential of LbL particle show complete reversal of charge after deposition of each poly-L-lysine or dextran sulfate layer. Reprinted with permission from ref (Poon, Lee, Morton, & Hammond, 2011). Copyright (2011) American Chemical Society.

LbL assembly has been used for constructing drug-loaded NP. Sacrificial templates such as CaCO_3 and mesoporous SiO_2 can be coated by LbL assembly and removed by dissolution. Drugs can be loaded in the resulting hollow capsules by manipulating the permeability of the formed shells (Yuri Lvov, Antipov, Mamedov, Möhwald, & Sukhorukov, 2001; Sukhorukov, Antipov, Voigt, Donath, & Möhwald, 2001). Polyelectrolytes and the formed complexes are sensitive to pH and ionic strength variations, so they can be made temporarily permeable for entrapping drug molecules. Alternatively, the drug can be mixed with the porous template during the layering process (De Koker et al., 2011). However, the sacrificial template methods have limitations such as low drug loading, harsh conditions required for template etching, and incomplete dissolution of the template (Mu, Zhong, Dong, Du, & Liu, 2012).

The LbL assembly technique can be used to coat solid drug cores, such as nanocrystals (Agarwal, Lvov, Sawant, & Torchilin, 2008). This method uses the drug itself as a template; thus, it need not be removed. LbL-coated nanocrystals have high drug loading, in addition to the functionality offered by the shell assembled on the surface. Some nanocrystals of hydrophobic drugs have intrinsic surface charge that allows binding of the first layered polyelectrolyte. If the surface charge is inadequate, a layer of a charged stabilizer that stably binds to the nanocrystal via non-electrostatic interactions, needs to be applied first (Polomska, Leroux, & Brambilla, 2017). LbL coated-nanocrystals can control drug dissolution rate and resist Ostwald ripening; therefore, it can circulate stably for prolonged time (Polomska, Leroux, et al., 2017). Moreover, the surface layer of the LbL assembly can be designed with functional groups that enables conjugation of targeting ligands (Cortez et al., 2007), stealth properties (Cheng, Yang, Chen, & Liu, 2012; Poon et al., 2011), or environment-responsive drug release (Delcea, Möhwald, & Skirtach, 2011). Polymers bound only via electrostatic interactions can be shed under physiological conditions; thus, multiple interactions or covalent bonding are more desirable (Polomska, Gauthier, & Leroux, 2017).

Drug may be involved in the LbL assembly as one of the assembled species. In nucleic acid delivery, negatively charged DNA/RNA strands are assembled alternatively with polycations yielding high loading and stability (Yu Lvov, Decher, & Sukhorukov, 1993; J. Zhang & Lynn, 2007). It is also possible to conjugate low molecular weight drugs to a polymer used for the LbL assembly via a degradable linkage (Ochs, Such, Yan, van Koeveden, & Caruso, 2010). Moreover, drugs with different physicochemical properties can be co-loaded in separate sets of layers for

combination therapy. With different drugs loaded in stratified shells, the LbL assembly may be used for sequential drug release (Wood, Chuang, Batten, Lynn, & Hammond, 2006). Positively charged lapatinib (P-gp inhibitor) was assembled as one of the LbL layers coating paclitaxel nanocrystals to overcome multidrug resistance (Vergara et al., 2012). Utilizing gold nanoparticles as a template core, DNA and siRNA were assembled in alternating layers of polyethyleneimine and a disulfide-containing poly(amido amine), respectively (Bishop, Tzeng, & Green, 2015). In another application, superparamagnetic iron oxide NP were included in the assembled multi-shell to enable magnetic-guided drug delivery (Mu et al., 2012).

1.3.4.3 Flash nanoprecipitation

Flash nanoprecipitation (FNP) can produce polymeric nanoparticles with high drug loading. In FNP, a water miscible organic solvent is used to dissolve a hydrophobic drug and an amphiphilic block copolymer such as poly(ethylene glycol)-*b*-poly(lactic-co-glycolic acid). The organic solution is injected at a high rate into a water stream in a confined space such as impingement jet mixers or multi inlet vortex mixers (Figure 3) (Suzanne M. D'Addio & Prud'homme, 2011). Rapid and turbulent mixing causes high supersaturation followed by coprecipitation of the drug and copolymer into NP with uniform size distributions and high drug loadings (up to 50%) (L. Zhao et al., 2017; Zhu, 2014). The NP core is the hydrophobic portion of the copolymer and the drug, while the hydrophilic portion forms a corona facing outside and protecting the NP from aggregation (Pustulka et al., 2013).

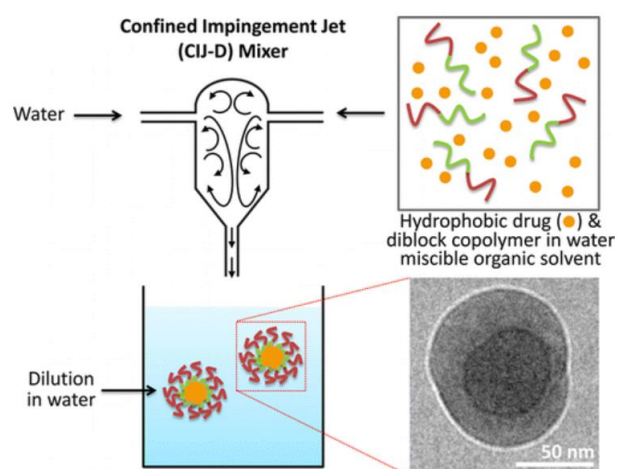


Figure 3: Schematic representation for the preparation of drug-loaded polymeric NP using FNP. Reprinted with permission from ref (Pustulka et al., 2013). Copyright (2013) American Chemical Society.

FNP is a simple and continuous process that requires minimal energy and is highly scalable with production rates of over 1000 kg NP per day (Sosa et al., 2016). FNP was used to prepare NP made solely of β -carotene (a model hydrophobic drug) with a size of 55 nm. However, the formed NP suspension was stable only for 4 h (Han et al., 2012). Therefore, a block copolymer is used as steric stabilizer for maintaining NP stability. Moreover, a functionalized copolymer can be used to produce NP with tailored surface for active targeting (Suzanne Marie D'Addio, 2012; Pinkerton et al., 2015).

A critical factor for successful FNP is the rapid mixing between the organic and aqueous phases (in order of milliseconds). In addition, the relative rates of drug nucleation and copolymer self-assembly control the NP size. Faster drug nucleation results in large unstable particles that easily precipitate, whereas faster copolymer assembly results in small NP size with a large population of drug-free micelles (Tang & Prud'homme, 2016). Therefore, for optimal drug loading, drug nucleation should be followed by copolymer self-assembly fast enough to kinetically trap drug nuclei. Achieving high level of supersaturation during mixing is a key to rapid nucleation. This needs optimization of the type of organic solvents, solvent/anti-solvent ratio and the drug concentration (Suzanne M. D'Addio & Prud'homme, 2011).

FNP can only be used for highly hydrophobic drugs with logP greater than 6 such as itraconazole and odanacatib (Varun Kumar, Wang, Riebe, Tung, & Prud'homme, 2009; Tang & Prud'homme, 2016). Paclitaxel, known for its hydrophobicity and low water solubility, formed NP of ~ 100 nm size and 55 %w/w loading using PLGA-b-PEG. However, NP grew in size to several micrometers in less than 2 h post- preparation (Zhu, 2014). This indicates that paclitaxel solubility in the solvent/anti-solvent mixture was sufficiently high, so it dissolved out of the NP core and recrystallized (Ostwald ripening). Changing the solvent/anti-solvent ratio to decrease the drug solubility is not always feasible. The type and volume of the organic solvent are limited by the drug solubility, miscibility with water, ease of removal and toxicity considerations. Increasing the water volume is also undesirable because it dilutes the product and thus needs further concentration steps. Drug solubility can be modified by chemical conjugation of a hydrophobic moiety. Paclitaxel conjugated to ethoxysilicate became sufficiently hydrophobic and formed stable NP with PLGA-b-PEG via FNP with over 50 %w/w loading of active paclitaxel (Han et al., 2015; Zhu, 2014). However, chemical conjugation requires reactive sites on the drug molecules and the new linkage should be easily cleaved regenerating the original drug in the body. Moreover, the

prodrug is considered a new chemical entity and needs approval as such by the Food and Drug Administration (FDA) (Tang & Prud'homme, 2016). An alternative approach is to co-precipitate the drug with both a hydrophobic cosolute and the amphiphilic copolymer. The cosolute has higher supersaturation; thus, it nucleates first to induce heterogeneous drug nucleation. This controls the number and size of drug nuclei. The drug should have high affinity for the cosolute so that it remains dispersed within the NP core and avoids recrystallization. This approach is beneficial for combination delivery or theranostic purposes, where multiple drugs or dyes are co-precipitated, respectively (Suzanne Marie D'Addio, 2012; Pinkerton et al., 2015). For weakly hydrophobic ionizable drugs, in-situ complexation with a hydrophobic counter-ion during the mixing step can create a salt with low solubility for stable encapsulation (V Kumar, 2011).

1.3.4.4 Nanoscale coordination networks

Nanoscale coordination networks or metal-organic frameworks (NMOFs) are hybrid networks of metal ions and organic polydentate ligands formed by coordination-directed self-assembly (Huxford, Della Rocca, & Lin, 2010). The bridging ligands are carboxylates, phosphonates or sulfonates (Ferey, 2008). NMOFs possess high porosity with large surface area for encapsulating large amounts of drugs. The structure of the ligand can be changed to accommodate the physicochemical properties of a particular drug allowing high drug loading capacity (Horcajada et al., 2010). NMOFs are biodegradable due to the labile metal-ligand bonding unlike conventional inorganic nanoparticles that often remain in the body for extended periods causing long-term toxicities (Huxford et al., 2010; J. Zhao et al., 2017). The synthesis of NMOFs is mild and involves simple mixing of the precursor solutions, which induces separation of the self-assembled NP. Temperature and/or surfactants can be additionally adjusted to control the rate of particle nucleation and growth (Della Rocca, Liu, & Lin, 2011).

For drug loading in NMOFs, the drug is either incorporated during synthesis or loaded into prepared networks via the highly porous structure. Drug molecules can also be grafted to the functional groups of these polymers after synthesis. In the direct incorporation approach, the drug will serve as a bridging ligand connecting the metal ions. This method results in high drug loading and uniform drug distribution in the NP with minimal use of inactive excipients (Della Rocca et al., 2011). Methotrexate, possessing two carboxylic acid groups capable of interacting with metal ions, was used as the bridging ligand to prepare NMOFs with a drug loading capacity of 79 % w/w

(Huxford, deKrafft, Boyle, Liu, & Lin, 2012). Disuccinatocisplatin, a cisplatin prodrug, was also used as the bridging ligand for Tb^{3+} ions, and their NMOFs were precipitated from aqueous solution of their mixture by the addition of a poor solvent (Figure 4) (Rieter, Pott, Taylor, & Lin, 2008). However, individual tuning of the physicochemical properties of the NMOFs is required depending on the drug's properties. In the post-synthesis drug loading, the drug can be bound to the NP via either non-covalent or covalent binding. The pore size needs to be larger than the drug molecules to enable drug diffusion. In addition, the relative affinity of the drug for the solvent and the porous frameworks as well as their contact time need to be adjusted to maximize drug loading (Horcajada et al., 2008). Ibuprofen was loaded with this method into frameworks of chromium terephthalate reaching a drug loading capacity of ~58 %w/w (Horcajada et al., 2006). Iron-carboxylate NMOFs were used to load a doxorubicin, busulfan, azidothymidine triphosphate and cidofovir by incubation in saturated solution of each drug (Horcajada et al., 2010). The NMOFs acted as molecular sponges resulting in loading contents of 29, 25.5, 41.5 and 42 %w/w, respectively. However, non-covalent drug binding may result in premature drug release during subsequent processing steps. Covalent drug binding offers better stability against premature drug release (Della Rocca et al., 2011). Covalent binding requires the presence of functional groups within the framework that can bind to drug molecules. Amino-functionalized Iron terephthalate NMOFs were prepared by incorporating 2-amino terephthalic acid during preparation (Taylor-Pashow, Della Rocca, Xie, Tran, & Lin, 2009). This enabled post-synthetic loading of a cisplatin prodrug, ethoxysuccinato-cisplatin, via carbonyldiimidazole chemistry. However, this method creates a prodrug; therefore, the cleavage of the formed bond under physiological conditions to recover the drug's activity needs to be confirmed. In addition, non-uniform drug loading may occur as the surface functional groups are more accessible for interaction with the drug molecules (Della Rocca et al., 2011).

Most of the metal ions used for preparation of NMOFs act as contrast agents. Therefore, NMOFs are important platforms for theranostic applications (Rowe, Thamm, Kraft, & Boyes, 2009; J. Zhao et al., 2017). However, instability is a major issue of NMOFs because they can dissolve upon high dilution in physiological conditions and prematurely release the drug. The particles can be coated with silica to improve dispersibility in water and retard the drug release. In addition, the silanol groups of silica shell can allow surface functionalization of the particles. Silyl derived c(RGDfK) was used to decorate the surface of silica coated NMOFs to improve their

cellular uptake by binding to $\alpha_v\beta_3$ integrin upregulated in many angiogenic cancers (Figure 4) (Huxford et al., 2010; Rieter et al., 2008). Organic polymers such as polyethylene glycol and poly(acrylic acid), and lipids were also used to coat the NMOFs for improving stability. The polymer/lipid will bind to the framework surface via coordination with vacant metal orbitals (Rowe, Chang, et al., 2009; Rowe, Thamm, et al., 2009), hydrophobic interactions (Huxford et al., 2012; D. Liu, Poon, Lu, He, & Lin, 2014) or covalent binding to the bridging ligands (D. Zhao et al., 2011).

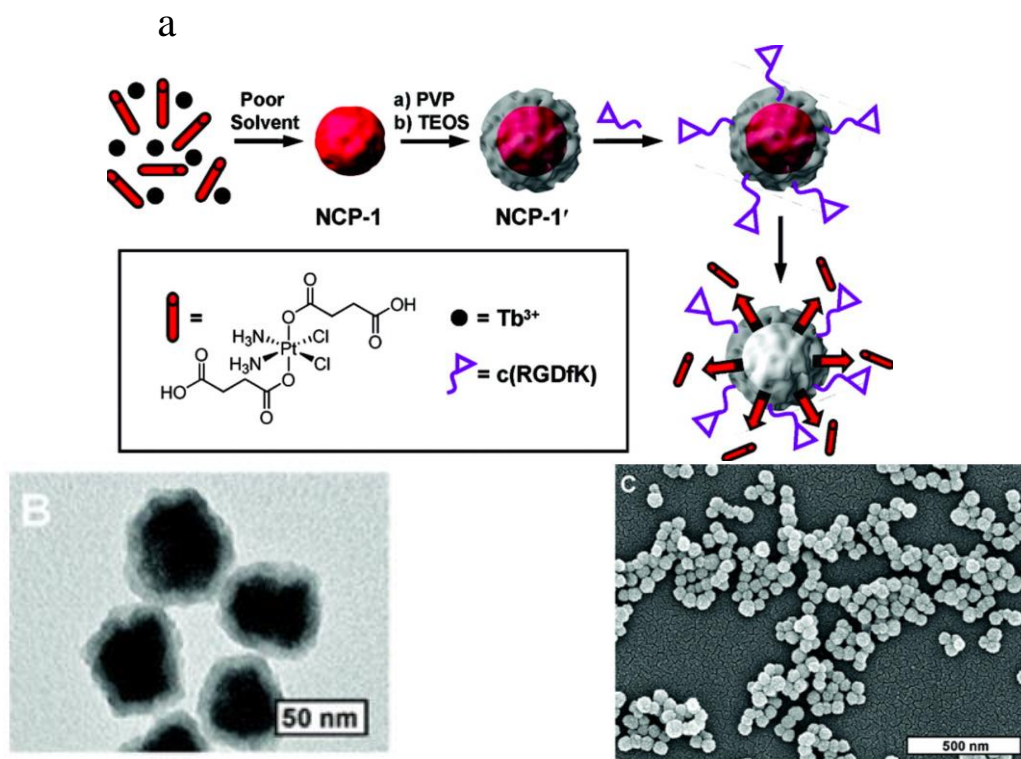


Figure 4: (a) Schematic for the synthesis of NMOF (NCP-1) of Tb^{3+} with disuccinatocisplatin (a cisplatin prodrug), followed by coating with silica shell (NCP-1') and conjugation to cRGDfk (PVP, polyvinylpyrrolidone; TEOS, tetraethylorthosilicate), (b) TEM and (c) SEM images of coated NCP-1'. Adapted with permission from ref (Rieter et al., 2008). Copyright (2008) American Chemical Society.

1.4 Conclusions

For clinical translation of an NP drug delivery system, it is critical that the NP carry a large amount of drug and maintain good stability during circulation. The high drug loading capacity will reduce the dose of NP and toxicities of excipients. The NP stability during circulation will ensure that the drug remains within the NP, taking advantage of its transport mechanism in reaching its

intended target site. Many of the studied NP systems fail to fulfill both criteria. And this is responsible at least partly for recent failure of leading NP products in clinical trials. Despite efforts made to overcome these limitations by NP preparation approaches such as drug nanocrystals, LbL assemblies, FNP and NMOFs, achieving both high drug loading and circulation stability in the same system is challenging. Therefore, it is necessary to integrate successful preparation techniques to develop NP systems with both increased drug loading capacity and circulation stability.

1.5 References

- Agarwal, A., Lvov, Y., Sawant, R., & Torchilin, V. (2008). Stable nanocolloids of poorly soluble drugs with high drug content prepared using the combination of sonication and layer-by-layer technology. *Journal of Controlled Release*, *128*(3), 255-260.
- Aguilar, Z. P. (2013). Chapter 5 - Targeted Drug Delivery. In Z. P. Aguilar (Ed.), *Nanomaterials for Medical Applications* (pp. 181-234): Elsevier.
- Alavizadeh, S. H., Badiie, A., Golmohammadzadeh, S., & Jaafari, M. R. (2014). The influence of phospholipid on the physicochemical properties and anti-tumor efficacy of liposomes encapsulating cisplatin in mice bearing C26 colon carcinoma. *International Journal of Pharmaceutics*, *473*(1), 326-333.
- Alexis, F., Pridgen, E., Molnar, L. K., & Farokhzad, O. C. (2008). Factors Affecting the Clearance and Biodistribution of Polymeric Nanoparticles. *Molecular Pharmaceutics*, *5*(4), 505-515. doi: 10.1021/mp800051m
- Allouche, J. (2013). Synthesis of Organic and Bioorganic Nanoparticles: An Overview of the Preparation Methods. In R. Brayner, F. Fiévet & T. Coradin (Eds.), *Nanomaterials: A Danger or a Promise? A Chemical and Biological Perspective* (pp. 27-74). London: Springer London.
- Andresen, T. L., Jensen, S. S., & Jørgensen, K. (2005). Advanced strategies in liposomal cancer therapy: Problems and prospects of active and tumor specific drug release. *Progress in Lipid Research*, *44*(1), 68-97. doi: <https://doi.org/10.1016/j.plipres.2004.12.001>
- Ao, L., Reichel, D., Hu, D., Jeong, H., Kim, K. B., Bae, Y., & Lee, W. (2015). Polymer Micelle Formulations of Proteasome Inhibitor Carfilzomib for Improved Metabolic Stability and Anticancer Efficacy in Human Multiple Myeloma and Lung Cancer Cell Lines. *The Journal of Pharmacology and Experimental Therapeutics*, *355*(2), 168-173. doi: 10.1124/jpet.115.226993
- Bae, Y. H., & Park, K. (2011). Targeted drug delivery to tumors: Myths, reality and possibility. *Journal of Controlled Release*, *153*(3), 198-205. doi: 10.1016/j.jconrel.2011.06.001
- Banerjee, D., & Sengupta, S. (2011). Chapter 12 - Nanoparticles in Cancer Chemotherapy. In V. Antonio (Ed.), *Progress in Molecular Biology and Translational Science* (Vol. Volume 104, pp. 489-507): Academic Press.
- Banissi, C., Ghiringhelli, F., Chen, L., & Carpentier, A. F. (2009). Treg depletion with a low-dose metronomic temozolomide regimen in a rat glioma model. *Cancer Immunology, Immunotherapy*, *58*(10), 1627-1634. doi: 10.1007/s00262-009-0671-1
- Bishop, C. J., Tzeng, S. Y., & Green, J. J. (2015). Degradable Polymer-Coated Gold Nanoparticles for Co-Delivery of DNA and siRNA. *Acta biomaterialia*, *11*, 393-403. doi: 10.1016/j.actbio.2014.09.020
- Blanco, E., Shen, H., & Ferrari, M. (2015). Principles of nanoparticle design for overcoming biological barriers to drug delivery. [Research]. *Nat Biotech*, *33*(9), 941-951. doi: 10.1038/nbt.3330
- Brannon-Peppas, L., & Blanchette, J. O. (2004). Nanoparticle and targeted systems for cancer therapy. *Advanced Drug Delivery Reviews*, *56*(11), 1649-1659.
- Brigger, I., Dubernet, C., & Couvreur, P. (2002). Nanoparticles in cancer therapy and diagnosis. *Advanced Drug Delivery Reviews*, *54*(5), 631-651. doi: 10.1016/S0169-409X(02)00044-3
- Browder, T., Butterfield, C. E., Kräling, B. M., Shi, B., Marshall, B., O'Reilly, M. S., & Folkman, J. (2000). Antiangiogenic Scheduling of Chemotherapy Improves Efficacy against Experimental Drug-resistant Cancer. *Cancer Research*, *60*(7), 1878.

- Caruso, F., Trau, D., Möhwald, H., & Renneberg, R. (2000). Enzyme Encapsulation in Layer-by-Layer Engineered Polymer Multilayer Capsules. *Langmuir*, 16(4), 1485-1488. doi: 10.1021/la991161n
- Chan, H.-K., & Kwok, P. C. L. (2011). Production methods for nanodrug particles using the bottom-up approach. *Advanced Drug Delivery Reviews*, 63(6), 406-416. doi: 10.1016/j.addr.2011.03.011
- Chan, T.-S., Hsu, C.-C., Pai, V. C., Liao, W.-Y., Huang, S.-S., Tan, K.-T., . . . Tsai, K. K. (2016). Metronomic chemotherapy prevents therapy-induced stromal activation and induction of tumor-initiating cells. *The Journal of experimental medicine*, 213(13), 2967-2988. doi: 10.1084/jem.20151665
- Chen, K. L., Smith, B. A., Ball, W. P., & Fairbrother, D. H. (2010). Assessing the colloidal properties of engineered nanoparticles in water: case studies from fullerene C60 nanoparticles and carbon nanotubes. *Environmental Chemistry*, 7(1), 10-27. doi: 10.1071/en09112
- Cheng, L., Yang, K., Chen, Q., & Liu, Z. (2012). Organic Stealth Nanoparticles for Highly Effective in Vivo Near-Infrared Photothermal Therapy of Cancer. *ACS Nano*, 6(6), 5605-5613. doi: 10.1021/nn301539m
- Cho, K., Wang, X., Nie, S., Chen, Z., & Shin, D. M. (2008). Therapeutic Nanoparticles for Drug Delivery in Cancer. [10.1158/1078-0432.CCR-07-1441]. *Clinical Cancer Research*, 14(5), 1310.
- Choi, H. S., Liu, W., Misra, P., Tanaka, E., Zimmer, J. P., Ipe, B. I., . . . Frangioni, J. V. (2007). Renal Clearance of Nanoparticles. *Nature biotechnology*, 25(10), 1165-1170. doi: 10.1038/nbt1340
- Cholkar, K., Acharya, G., Trinh, H. M., & Singh, G. (2017). Chapter 1 - Therapeutic Applications of Polymeric Materials *Emerging Nanotechnologies for Diagnostics, Drug Delivery and Medical Devices* (pp. 1-19). Boston: Elsevier.
- Cortez, C., Tomaskovic-Crook, E., Johnston, A. P. R., Scott, A. M., Nice, E. C., Heath, J. K., & Caruso, F. (2007). Influence of Size, Surface, Cell Line, and Kinetic Properties on the Specific Binding of A33 Antigen-Targeted Multilayered Particles and Capsules to Colorectal Cancer Cells. *ACS Nano*, 1(2), 93-102. doi: 10.1021/nn700060m
- Crielaard, B. J., Rijcken, C. J. F., Quan, L., van der Wal, S., Altintas, I., van der Pot, M., . . . Storm, G. (2012). Glucocorticoid-loaded core-cross-linked polymeric micelles with tailorable release kinetics for targeted therapy of rheumatoid arthritis. *Angewandte Chemie (International ed. in English)*, 51(29), 7254-7258. doi: 10.1002/anie.201202713
- D'Addio, S. M. (2012). *Tuberculosis Therapeutics: Engineering of Nanomedicinal Systems For Local Delivery of Targeted Drug Cocktails*. (Ph.D.), Princeton University, Ann Arbor.
- D'Addio, S. M., & Prud'homme, R. K. (2011). Controlling drug nanoparticle formation by rapid precipitation. *Advanced Drug Delivery Reviews*, 63(6), 417-426. doi: <https://doi.org/10.1016/j.addr.2011.04.005>
- De Koker, S., De Cock, L. J., Rivera-Gil, P., Parak, W. J., Auzély Velty, R., Vervaet, C., . . . De Geest, B. G. (2011). Polymeric multilayer capsules delivering biotherapeutics. *Advanced Drug Delivery Reviews*, 63(9), 748-761. doi: <https://doi.org/10.1016/j.addr.2011.03.014>
- Decher, G., Hong, J. D., & Schmitt, J. (1992). Buildup of ultrathin multilayer films by a self-assembly process: III. Consecutively alternating adsorption of anionic and cationic polyelectrolytes on charged surfaces. *Thin Solid Films*, 210, 831-835. doi: 10.1016/0040-6090(92)90417-A

- Delcea, M., Möhwald, H., & Skirtach, A. G. (2011). Stimuli-responsive LbL capsules and nanoshells for drug delivery. *Advanced Drug Delivery Reviews*, 63(9), 730-747. doi: <https://doi.org/10.1016/j.addr.2011.03.010>
- Della Rocca, J., Liu, D., & Lin, W. (2011). Nanoscale Metal–Organic Frameworks for Biomedical Imaging and Drug Delivery. *Accounts of Chemical Research*, 44(10), 957-968. doi: 10.1021/ar200028a
- Desai, N. (2008). Nab technology: A drug delivery platform utilising endothelial gp60 receptor-based transport and tumour-derived SPARC for targeting drug delivery report., 2007/2008, 37-41.
- Diab, R., Jaafar-Maalej, C., Fessi, H., & Maincent, P. (2012). Engineered Nanoparticulate Drug Delivery Systems: The Next Frontier for Oral Administration? *The AAPS Journal*, 14(4), 688-702. doi: 10.1208/s12248-012-9377-y
- Dragojevic, S., Ryu, J., & Raucher, D. (2015). Polymer-Based Prodrugs: Improving Tumor Targeting and the Solubility of Small Molecule Drugs in Cancer Therapy. *Molecules*, 20(12), 19804.
- Dunne, M., Corrigan, I., & Ramtoola, Z. (2000). Influence of particle size and dissolution conditions on the degradation properties of polylactide-co-glycolide particles. *Biomaterials*, 21(16), 1659-1668.
- Elimelech, M., & O'Melia, C. R. (1990). Effect of particle size on collision efficiency in the deposition of Brownian particles with electrostatic energy barriers. *Langmuir*, 6(6), 1153-1163. doi: 10.1021/la00096a023
- Ellerhorst, J. A., Bedikian, A., Ring, S., Buzaid, A. C., Eton, O., & Legha, S. S. (1999). Phase II trial of doxil for patients with metastatic melanoma refractory to frontline therapy. *Oncol Rep*, 6(5), 1097-1099.
- Ferey, G. (2008). Hybrid porous solids: past, present, future. [10.1039/B618320B]. *Chemical Society Reviews*, 37(1), 191-214. doi: 10.1039/b618320b
- Fritze, A., Hens, F., Kimpfler, A., Schubert, R., & Peschka-Süss, R. (2006). Remote loading of doxorubicin into liposomes driven by a transmembrane phosphate gradient. *Biochimica et Biophysica Acta (BBA) - Biomembranes*, 1758(10), 1633-1640. doi: <https://doi.org/10.1016/j.bbamem.2006.05.028>
- Fuhrmann, K., Gauthier, M. A., & Leroux, J.-C. (2014). Targeting of Injectable Drug Nanocrystals. *Molecular Pharmaceutics*, 11(6), 1762-1771. doi: 10.1021/mp5001247
- Fuhrmann, K., Połomska, A., Aeberli, C., Castagner, B., Gauthier, M. A., & Leroux, J.-C. (2013). Modular Design of Redox-Responsive Stabilizers for Nanocrystals. *ACS Nano*, 7(9), 8243-8250. doi: 10.1021/nn4037317
- Gao, H., & He, Q. (2014). The interaction of nanoparticles with plasma proteins and the consequent influence on nanoparticles behavior. *Expert Opinion on Drug Delivery*, 11(3), 409-420. doi: 10.1517/17425247.2014.877442
- Gao, L., Liu, G., Wang, X., Liu, F., Xu, Y., & Ma, J. (2011). Preparation of a chemically stable quercetin formulation using nanosuspension technology. *International Journal of Pharmaceutics*, 404(1), 231-237. doi: 10.1016/j.ijpharm.2010.11.009
- Garcia, A. A., Kempf, R. A., Rogers, M., & Muggia, F. M. (1998). A phase II study of Doxil (liposomal doxorubicin): Lack of activity in poor prognosis soft tissue sarcomas. *Annals of Oncology*, 9(10), 1131-1133. doi: 10.1023/a:1008439013169

- Ghiringhelli, F., Menard, C., Puig, P. E., Ladoire, S., Roux, S., Martin, F., . . . Chauffert, B. (2007). Metronomic cyclophosphamide regimen selectively depletes CD4+CD25+ regulatory T cells and restores T and NK effector functions in end stage cancer patients. *Cancer Immunology, Immunotherapy*, 56(5), 641-648. doi: 10.1007/s00262-006-0225-8
- Glavas, L., Olsén, P., Odelius, K., & Albertsson, A.-C. (2013). Achieving Micelle Control through Core Crystallinity. *Biomacromolecules*, 14(11), 4150-4156. doi: 10.1021/bm401312j
- Hamaguchi, T., Kato, K., Yasui, H., Morizane, C., Ikeda, M., Ueno, H., . . . Matsumura, Y. (2007). A phase I and pharmacokinetic study of NK105, a paclitaxel-incorporating micellar nanoparticle formulation. *British Journal of Cancer*, 97(2), 170-176. doi: 10.1038/sj.bjc.6603855
- Hammond, P. T. (2012). Building biomedical materials layer-by-layer. *Materials Today*, 15(5), 196-206. doi: [https://doi.org/10.1016/S1369-7021\(12\)70090-1](https://doi.org/10.1016/S1369-7021(12)70090-1)
- Han, J., Michel, A. R., Lee, H. S., Kalscheuer, S., Wohl, A., Hoye, T. R., . . . Macosko, C. W. (2015). Nanoparticles Containing High Loads of Paclitaxel Silicate Prodrugs: Formulation, Drug Release, and Anti-cancer Efficacy. *Molecular Pharmaceutics*, 12(12), 4329-4335. doi: 10.1021/acs.molpharmaceut.5b00530
- Han, J., Zhu, Z., Qian, H., Wohl, A. R., Beaman, C. J., Hoye, T. R., & Macosko, C. W. (2012). A simple confined impingement jets mixer for flash nanoprecipitation. *Journal of Pharmaceutical Sciences*, 101(10), 4018-4023. doi: <https://doi.org/10.1002/jps.23259>
- Haran, G., Cohen, R., Bar, L. K., & Barenholz, Y. (1993). Transmembrane ammonium sulfate gradients in liposomes produce efficient and stable entrapment of amphipathic weak bases. *Biochimica et Biophysica Acta (BBA) - Biomembranes*, 1151(2), 201-215. doi: [https://doi.org/10.1016/0005-2736\(93\)90105-9](https://doi.org/10.1016/0005-2736(93)90105-9)
- Hogg, R. (2013). Bridging Flocculation by Polymers. *KONA Powder and Particle Journal*, 30, 3-14. doi: 10.14356/kona.2013005
- Horcajada, P., Chalati, T., Serre, C., Gillet, B., Sebrie, C., Baati, T., . . . Gref, R. (2010). Porous metal-organic-framework nanoscale carriers as a potential platform for drug delivery and imaging. [10.1038/nmat2608]. *Nat Mater*, 9(2), 172-178.
- Horcajada, P., Serre, C., Maurin, G., Ramsahye, N. A., Balas, F., Vallet-Regí, M., . . . Férey, G. (2008). Flexible Porous Metal-Organic Frameworks for a Controlled Drug Delivery. *Journal of the American Chemical Society*, 130(21), 6774-6780. doi: 10.1021/ja710973k
- Horcajada, P., Serre, C., Vallet-Regí, M., Sebban, M., Taulelle, F., & Férey, G. (2006). Metal–Organic Frameworks as Efficient Materials for Drug Delivery. *Angewandte Chemie International Edition*, 45(36), 5974-5978. doi: 10.1002/anie.200601878
- Hotze, E. M., Phenrat, T., & Lowry, G. V. (2010). Nanoparticle Aggregation: Challenges to Understanding Transport and Reactivity in the Environment. *Journal of Environmental Quality*, 39(6), 1909-1924. doi: 10.2134/jeq2009.0462
- Hu, J., Guo, J., Xie, Z., Shan, D., Gerhard, E., Qian, G., & Yang, J. (2016). Fluorescence imaging enabled poly(lactide-co-glycolide). *Acta biomaterialia*, 29, 307-319. doi: 10.1016/j.actbio.2015.10.010
- Huxford, R. C., deKrafft, K. E., Boyle, W. S., Liu, D., & Lin, W. (2012). Lipid-Coated Nanoscale Coordination Polymers for Targeted Delivery of Antifolates to Cancer Cells. *Chemical science (Royal Society of Chemistry : 2010)*, 3(1), 10.1039/C1031SC00499A. doi: 10.1039/c1sc00499a

- Huxford, R. C., Della Rocca, J., & Lin, W. (2010). Metal–organic frameworks as potential drug carriers. *Current Opinion in Chemical Biology*, *14*(2), 262-268. doi: <https://doi.org/10.1016/j.cbpa.2009.12.012>
- Iyer, A. K., Khaled, G., Fang, J., & Maeda, H. (2006). Exploiting the enhanced permeability and retention effect for tumor targeting. *Drug Discovery Today*, *11*(17), 812-818. doi: <https://doi.org/10.1016/j.drudis.2006.07.005>
- Jiang, X., Dai, H., Leong, K. W., Goh, S.-H., Mao, H.-Q., & Yang, Y.-Y. (2006). Chitosan-g-PEG/DNA complexes deliver gene to the rat liver via intrabiliary and intraportal infusions. *The Journal of Gene Medicine*, *8*(4), 477-487. doi: 10.1002/jgm.868
- Jyoti, A., Fugit, K. D., Sethi, P., McGarry, R. C., Anderson, B. D., & Upreti, M. (2015). An in vitro assessment of liposomal topotecan simulating metronomic chemotherapy in combination with radiation in tumor-endothelial spheroids. *Scientific Reports*, *5*, 15236-15236. doi: 10.1038/srep15236
- Kamaly, N., Yameen, B., Wu, J., & Farokhzad, O. C. (2016). Degradable Controlled-Release Polymers and Polymeric Nanoparticles: Mechanisms of Controlling Drug Release. *Chemical Reviews*, *116*(4), 2602-2663. doi: 10.1021/acs.chemrev.5b00346
- Karavelidis, V., Karavas, E., Giliopoulos, D., Papadimitriou, S., & Bikiaris, D. (2011). Evaluating the effects of crystallinity in new biocompatible polyester nanocarriers on drug release behavior. *International Journal of Nanomedicine*, *6*, 3021-3032. doi: 10.2147/ijn.s26016
- Kareva, I., Waxman, D. J., & Lakka Klement, G. (2015). Metronomic chemotherapy: an attractive alternative to maximum tolerated dose therapy that can activate anti-tumor immunity and minimize therapeutic resistance. *Cancer letters*, *358*(2), 100-106. doi: 10.1016/j.canlet.2014.12.039
- Kasai, H., Murakami, T., Ikuta, Y., Koseki, Y., Baba, K., Oikawa, H., . . . Hashida, M. (2012). Creation of Pure Nanodrugs and Their Anticancer Properties. *Angewandte Chemie International Edition*, *51*(41), 10315-10318. doi: 10.1002/anie.201204596
- Keck, C. M., & Müller, R. H. (2006). Drug nanocrystals of poorly soluble drugs produced by high pressure homogenisation. *European Journal of Pharmaceutics and Biopharmaceutics*, *62*(1), 3-16. doi: <http://dx.doi.org/10.1016/j.ejpb.2005.05.009>
- Khandare, J., Calderon, M., Dagia, N. M., & Haag, R. (2012). Multifunctional dendritic polymers in nanomedicine: opportunities and challenges. [10.1039/C1CS15242D]. *Chemical Society Reviews*, *41*(7), 2824-2848. doi: 10.1039/c1cs15242d
- Kim, J. O., Kabanov, A. V., & Bronich, T. K. (2009). Polymer micelles with cross-linked polyanion core for delivery of a cationic drug doxorubicin. *Journal of Controlled Release*, *138*(3), 197-204. doi: <http://dx.doi.org/10.1016/j.jconrel.2009.04.019>
- Kim, S., & Lee, J. (2011). Folate-targeted drug-delivery systems prepared by nano-comminution. *Drug Development and Industrial Pharmacy*, *37*(2), 131-138. doi: 10.3109/03639045.2010.496788
- Kipp, J. E. W., Joseph, C. T., Doty, M. J., & Rebbeck, C. L. (2001). US Patent Patent No. Klement, G., Baruchel, S., Rak, J., Man, S., Clark, K., Hicklin, D. J., . . . Kerbel, R. S. (2000). Continuous low-dose therapy with vinblastine and VEGF receptor-2 antibody induces sustained tumor regression without overt toxicity. [Research Support, Non-U S Gov't Research Support, U S Gov't, P H S]. *J Clin Invest*, *105*(8).

- Kufleitner, J., Wagner, S., Worek, F., von Briesen, H., & Kreuter, J. (2010). Adsorption of obidoxime onto human serum albumin nanoparticles: Drug loading, particle size and drug release. *Journal of Microencapsulation*, 27(6), 506-513. doi: 10.3109/02652041003681406
- Kumar, V. (2011). *Polymeric and lipid nanoparticles for therapeutics delivery*. (Ph.D.), Princeton University, Ann Arbor.
- Kumar, V., Wang, L., Riebe, M., Tung, H.-H., & Prud'homme, R. K. (2009). Formulation and Stability of Itraconazole and Odanacatib Nanoparticles: Governing Physical Parameters. *Molecular Pharmaceutics*, 6(4), 1118-1124. doi: 10.1021/mp900002t
- Laine, G. A., Hossain, S. H., Solis, R. T., & Adams, S. C. (1995). Polyethylene Glycol Nephrotoxicity Secondary to Prolonged High-Dose Intravenous Lorazepam. *Annals of Pharmacotherapy*, 29(11), 1110-1114. doi: doi:10.1177/106002809502901107
- Lazzari, S., Moscatelli, D., Codari, F., Salmona, M., Morbidelli, M., & Diomedea, L. (2012). Colloidal stability of polymeric nanoparticles in biological fluids. *Journal of nanoparticle research : an interdisciplinary forum for nanoscale science and technology*, 14(6), 920-920. doi: 10.1007/s11051-012-0920-7
- Li, S.-D., & Huang, L. (2008). Pharmacokinetics and Biodistribution of Nanoparticles. *Molecular Pharmaceutics*, 5(4), 496-504. doi: 10.1021/mp800049w
- Li, S.-D., & Huang, L. (2010). Stealth Nanoparticles: High Density but Sheddable PEG is a Key for Tumor Targeting. *Journal of controlled release : official journal of the Controlled Release Society*, 145(3), 178-181. doi: 10.1016/j.jconrel.2010.03.016
- Liang, Y. (2010). *Drug release and pharmacokinetic properties of liposomal DB-67*. (Master of Science), University of Kentucky Retrieved from https://uknowledge.uky.edu/gradschool_theses/17
- Liu, D., Poon, C., Lu, K., He, C., & Lin, W. (2014). Self-assembled nanoscale coordination polymers with trigger release properties for effective anticancer therapy. [Article]. 5, 4182. doi: 10.1038/ncomms5182
- Liu, K. C., & Yeo, Y. (2014). Extracellular stability of nanoparticulate drug carriers. *Archives of Pharmacol Research*, 37(1), 16-23. doi: 10.1007/s12272-013-0286-0
- Liu, L., Ma, P., Wang, H., Zhang, C., Sun, H., Wang, C., . . . Ma, G. (2016). Immune responses to vaccines delivered by encapsulation into and/or adsorption onto cationic lipid-PLGA hybrid nanoparticles. *Journal of Controlled Release*, 225, 230-239. doi: 10.1016/j.jconrel.2016.01.050
- Liu, Y., Kathan, K., Saad, W., & Prud'homme, R. K. (2007). Ostwald Ripening of beta-Carotene Nanoparticles. *Physical Review Letters*, 98(3), 036102.
- Lourenco, C., Teixeira, M., Simões, S., & Gaspar, R. (1996). Steric stabilization of nanoparticles: Size and surface properties. *International Journal of Pharmaceutics*, 138(1), 1-12. doi: [https://doi.org/10.1016/0378-5173\(96\)04486-9](https://doi.org/10.1016/0378-5173(96)04486-9)
- Lu, X.-Y., Wu, D.-C., Li, Z.-J., & Chen, G.-Q. (2011). Chapter 7 - Polymer Nanoparticles. In A. Villaverde (Ed.), *Progress in Molecular Biology and Translational Science* (Vol. 104, pp. 299-323): Academic Press.
- Lu, Y., Chen, Y., Gemeinhart, R. A., Wu, W., & Li, T. (2015). Developing nanocrystals for cancer treatment. *Nanomedicine*, 10(16), 2537-2552. doi: 10.2217/nmm.15.73
- Lvov, Y., Antipov, A. A., Mamedov, A., Möhwald, H., & Sukhorukov, G. B. (2001). Urease Encapsulation in Nanoorganized Microshells. *Nano Letters*, 1(3), 125-128. doi: 10.1021/nl0100015

- Lvov, Y., Decher, G., & Sukhorukov, G. (1993). Assembly of thin films by means of successive deposition of alternate layers of DNA and poly(allylamine). *Macromolecules*, *26*(20), 5396-5399. doi: 10.1021/ma00072a016
- Ma, Z., Bai, J., Wang, Y., & Jiang, X. (2014). Impact of Shape and Pore Size of Mesoporous Silica Nanoparticles on Serum Protein Adsorption and RBCs Hemolysis. *Acs Applied Materials & Interfaces*, *6*(4), 2431-2438. doi: 10.1021/am404860q
- Malam, Y., Loizidou, M., & Seifalian, A. M. (2009). Liposomes and nanoparticles: nanosized vehicles for drug delivery in cancer. *Trends in Pharmacological Sciences*, *30*(11), 592-599. doi: <https://doi.org/10.1016/j.tips.2009.08.004>
- Matsumura, Y., & Maeda, H. (1986). A New Concept for Macromolecular Therapeutics in Cancer Chemotherapy: Mechanism of Tumor-tropic Accumulation of Proteins and the Antitumor Agent Smancs. *Cancer Research*, *46*(12 Part 1), 6387.
- McFarlane, N. L., Wagner, N. J., Kaler, E. W., & Lynch, M. L. (2010). Poly(ethylene oxide) (PEO) and Poly(vinyl pyrrolidone) (PVP) Induce Different Changes in the Colloid Stability of Nanoparticles. *Langmuir*, *26*(17), 13823-13830. doi: 10.1021/la101907s
- Merisko-Liversidge, E., Liversidge, G. G., & Cooper, E. R. (2003). Nanosizing: a formulation approach for poorly-water-soluble compounds. *European Journal of Pharmaceutical Sciences*, *18*(2), 113-120. doi: [http://dx.doi.org/10.1016/S0928-0987\(02\)00251-8](http://dx.doi.org/10.1016/S0928-0987(02)00251-8)
- Miele, E., Spinelli, G. P., Miele, E., Tomao, F., & Tomao, S. (2009). Albumin-bound formulation of paclitaxel (Abraxane®) ABI-007 in the treatment of breast cancer. *International Journal of Nanomedicine*, *4*, 99-105.
- Mohr, K., Sommer, M., Baier, G., Schöttler, S., Okwieka, P., Tenzer, S., . . . Meyer, R. G. (2014). Aggregation Behavior of Polystyrene-Nanoparticles in Human Blood Serum and its Impact on the in vivo Distribution in Mice. *Journal of Nanomedicine & Nanotechnology*, *5*(2).
- Moore, T. L., Rodriguez-Lorenzo, L., Hirsch, V., Balog, S., Urban, D., Jud, C., . . . Petri-Fink, A. (2015). Nanoparticle colloidal stability in cell culture media and impact on cellular interactions. [10.1039/C4CS00487F]. *Chemical Society Reviews*, *44*(17), 6287-6305. doi: 10.1039/c4cs00487f
- Mu, B., Zhong, W., Dong, Y., Du, P., & Liu, P. (2012). Encapsulation of drug microparticles with self-assembled Fe₃O₄/alginate hybrid multilayers for targeted controlled release. *Journal of Biomedical Materials Research Part B: Applied Biomaterials*, *100B*(3), 825-831. doi: 10.1002/jbm.b.32646
- Napper, D. H. (1977). Steric stabilization. *Journal of Colloid and Interface Science*, *58*(2), 390-407. doi: [https://doi.org/10.1016/0021-9797\(77\)90150-3](https://doi.org/10.1016/0021-9797(77)90150-3)
- O'Hagan, D., Singh, M., Ugozzoli, M., Wild, C., Barnett, S., Chen, M., . . . Ulmer, J. B. (2001). Induction of Potent Immune Responses by Cationic Microparticles with Adsorbed Human Immunodeficiency Virus DNA Vaccines. *Journal of Virology*, *75*(19), 9037-9043. doi: 10.1128/jvi.75.19.9037-9043.2001
- Ochs, C. J., Such, G. K., Yan, Y., van Koeveerden, M. P., & Caruso, F. (2010). Biodegradable Click Capsules with Engineered Drug-Loaded Multilayers. *ACS Nano*, *4*(3), 1653-1663. doi: 10.1021/nn9014278
- Park, J. E., Chun, S. E., Reichel, D., Min, J. S., Lee, S. C., Han, S., . . . Lee, W. (2017). Polymer micelle formulation for the proteasome inhibitor drug carfilzomib: Anticancer efficacy and pharmacokinetic studies in mice. *PLoS ONE*, *12*(3), e0173247. doi: 10.1371/journal.pone.0173247

- Picola, I. P. D., Busson, K. A. N., Casé, A. H., Nasário, F. D., Tiera, V. A. d. O., Taboga, S. R., . . . Tiera, M. J. (2013). Effect of ionic strength solution on the stability of chitosan–DNA nanoparticles. *Journal of Experimental Nanoscience*, 8(5), 703-716. doi: 10.1080/17458080.2011.602120
- Pinkerton, N. M., Gindy, M. E., Calero-DdelC, V. L., Wolfson, T., Pagels, R. F., Adler, D., . . . Prud'homme, R. K. (2015). Single-Step Assembly of Multi-Modal Imaging Nanocarriers: MRI and Long-Wavelength Fluorescence Imaging. *Advanced healthcare materials*, 4(9), 1376-1385. doi: 10.1002/adhm.201400766
- Polomska, A., Gauthier, M. A., & Leroux, J.-C. (2017). In Vitro and In Vivo Evaluation of PEGylated Layer-by-Layer Polyelectrolyte-Coated Paclitaxel Nanocrystals. *Small*, 13(2), 1602066-n/a. doi: 10.1002/sml.201602066
- Polomska, A., Leroux, J.-C., & Brambilla, D. (2017). Layer-by-Layer Coating of Solid Drug Cores: A Versatile Method to Improve Stability, Control Release and Tune Surface Properties. *Macromolecular Bioscience*, 17(1), 1600228-n/a. doi: 10.1002/mabi.201600228
- Poon, Z., Lee, J. B., Morton, S. W., & Hammond, P. T. (2011). Controlling in Vivo Stability and Biodistribution in Electrostatically Assembled Nanoparticles for Systemic Delivery. *Nano Letters*, 11(5), 2096-2103. doi: 10.1021/nl200636r
- Pustulka, K. M., Wohl, A. R., Lee, H. S., Michel, A. R., Han, J., Hoyer, T. R., . . . Macosko, C. W. (2013). Flash Nanoprecipitation: Particle Structure and Stability. *Molecular Pharmaceutics*, 10(11), 4367-4377. doi: 10.1021/mp400337f
- Qiu, X., Leporatti, S., Donath, E., & Möhwald, H. (2001). Studies on the Drug Release Properties of Polysaccharide Multilayers Encapsulated Ibuprofen Microparticles. *Langmuir*, 17(17), 5375-5380. doi: 10.1021/la010201w
- Radwan, M. A. (1995). In Vitro Evaluation of Polyisobutylcyanoacrylate Nanoparticles as a Controlled Drug Carrier for Theophylline. *Drug Development and Industrial Pharmacy*, 21(20), 2371-2375. doi: 10.3109/03639049509070875
- Richardson, J. J., Cui, J., Björnmalm, M., Braunger, J. A., Ejima, H., & Caruso, F. (2016). Innovation in Layer-by-Layer Assembly. *Chemical Reviews*, 116(23), 14828-14867. doi: 10.1021/acs.chemrev.6b00627
- Rieter, W. J., Pott, K. M., Taylor, K. M., & Lin, W. (2008). Nanoscale coordination polymers for platinum-based anticancer drug delivery. [Research Support, N I H , Extramural Research Support, Non-U S Gov't Research Support, U S Gov't, Non-P H S]. *J Am Chem Soc*, 130(35), 11584-11585.
- Rijcken Cristianne, J. F., Talelli, M., van Nostrum Cornelus, F., Storm, G., & Hennink Wim, E. (2010). Therapeutic Nanomedicine: Cross linked micelles with transiently linked drugs – a versatile drug delivery system *European Journal of Nanomedicine* (Vol. 3, pp. 19).
- Rocca, J. D., Liu, D., & Lin, W. (2012). Are high drug loading nanoparticles the next step forward for chemotherapy? *Nanomedicine (London, England)*, 7(3), 303-305. doi: 10.2217/nnm.11.191
- Rowe, M. D., Chang, C.-C., Thamm, D. H., Kraft, S. L., Harmon, J. F., Vogt, A. P., . . . Boyes, S. G. (2009). Tuning the Magnetic Resonance Imaging Properties of Positive Contrast Agent Nanoparticles by Surface Modification with RAFT Polymers. *Langmuir*, 25(16), 9487-9499. doi: 10.1021/la900730b

- Rowe, M. D., Thamm, D. H., Kraft, S. L., & Boyes, S. G. (2009). Polymer-Modified Gadolinium Metal-Organic Framework Nanoparticles Used as Multifunctional Nanomedicines for the Targeted Imaging and Treatment of Cancer. *Biomacromolecules*, *10*(4), 983-993. doi: 10.1021/bm900043e
- Saltzman, W. M. (2001). *Drug Delivery : Engineering Principles for Drug Therapy*. Cary, UNITED STATES: Oxford University Press USA - OSO.
- Shah, A. B., Rejniak, K. A., & Gevertz, J. L. (2016). Limiting the development of anti-cancer drug resistance in a spatial model of micrometastases. *Mathematical biosciences and engineering : MBE*, *13*(6), 1185-1206. doi: 10.3934/mbe.2016038
- Shen, G., Xing, R., Zhang, N., Chen, C., Ma, G., & Yan, X. (2016). Interfacial Cohesion and Assembly of Bioadhesive Molecules for Design of Long-Term Stable Hydrophobic Nanodrugs toward Effective Anticancer Therapy. *ACS Nano*, *10*(6), 5720-5729. doi: 10.1021/acsnano.5b07276
- Shuai, X., Ai, H., Nasongkla, N., Kim, S., & Gao, J. (2004). Micellar carriers based on block copolymers of poly(ϵ -caprolactone) and poly(ethylene glycol) for doxorubicin delivery. *Journal of Controlled Release*, *98*(3), 415-426. doi: 10.1016/j.jconrel.2004.06.003
- Singh, R., & Lillard, J. W. (2009). Nanoparticle-based targeted drug delivery. *Experimental and molecular pathology*, *86*(3), 215-223. doi: 10.1016/j.yexmp.2008.12.004
- Soppimath, K. S., Aminabhavi, T. M., Kulkarni, A. R., & Rudzinski, W. E. (2001). Biodegradable polymeric nanoparticles as drug delivery devices. *Journal of Controlled Release*, *70*(1-2), 1-20. doi: https://doi.org/10.1016/S0168-3659(00)00339-4
- Sosa, C., Liu, R., Tang, C., Qu, F., Niu, S., Bazant, M. Z., . . . Priestley, R. D. (2016). Soft Multifaced and Patchy Colloids by Constrained Volume Self-Assembly. *Macromolecules*, *49*(9), 3580-3585. doi: 10.1021/acs.macromol.6b00708
- Studart, A. R., Amstad, E., & Gauckler, L. J. (2007). Colloidal Stabilization of Nanoparticles in Concentrated Suspensions. *Langmuir*, *23*(3), 1081-1090. doi: 10.1021/la062042s
- Such, G. K., Johnston, A. P. R., & Caruso, F. (2011). Engineered hydrogen-bonded polymer multilayers: from assembly to biomedical applications. [10.1039/C0CS00001A]. *Chemical Society Reviews*, *40*(1), 19-29. doi: 10.1039/c0cs00001a
- Sukhorukov, G. B., Antipov, A. A., Voigt, A., Donath, E., & Möhwald, H. (2001). pH-Controlled Macromolecule Encapsulation in and Release from Polyelectrolyte Multilayer Nanocapsules. *Macromolecular Rapid Communications*, *22*(1), 44-46. doi: 10.1002/1521-3927(20010101)22:1<44::aid-marc44>3.0.co;2-u
- Sun, B., & Yeo, Y. (2012). Nanocrystals for the parenteral delivery of poorly water-soluble drugs. *Current Opinion in Solid State and Materials Science*, *16*(6), 295-301. doi: <http://dx.doi.org/10.1016/j.cossms.2012.10.004>
- Tang, C., & Prud'homme, R. K. (2016). Targeted Theragnostic Nanoparticles Via Flash Nanoprecipitation: Principles of Material Selection. In C. Vauthier & G. Ponchel (Eds.), *Polymer Nanoparticles for Nanomedicines: A Guide for their Design, Preparation and Development* (pp. 55-85). Cham: Springer International Publishing.
- Tao, X., Jin, S., Wu, D., Ling, K., Yuan, L., Lin, P., . . . Yang, X. (2016). Effects of Particle Hydrophobicity, Surface Charge, Media pH Value and Complexation with Human Serum Albumin on Drug Release Behavior of Mitoxantrone-Loaded Pullulan Nanoparticles. *Nanomaterials*, *6*(1). doi: 10.3390/nano6010002

- Tao, X., Zhang, Q., Ling, K., Chen, Y., Yang, W., Gao, F., & Shi, G. (2012). Effect of pullulan nanoparticle surface charges on HSA complexation and drug release behavior of HSA-bound nanoparticles. [Research Support, Non-U.S. Gov't]. *PLoS ONE*, 7(11), e49304. doi: 10.1371/journal.pone.0049304
- Taylor-Pashow, K. M. L., Della Rocca, J., Xie, Z., Tran, S., & Lin, W. (2009). Postsynthetic Modifications of Iron-Carboxylate Nanoscale Metal–Organic Frameworks for Imaging and Drug Delivery. *Journal of the American Chemical Society*, 131(40), 14261-14263. doi: 10.1021/ja906198y
- Tong, R., & Cheng, J. (2008). Paclitaxel-Initiated, Controlled Polymerization of Lactide for the Formulation of Polymeric Nanoparticulate Delivery Vehicles. *Angewandte Chemie International Edition*, 47(26), 4830-4834. doi: 10.1002/anie.200800491
- Tsukamoto, T., Hironaka, K., Fujisawa, T., Yamaguchi, D., Tahara, K., Tozuka, Y., & Takeuchi, H. (2013). Preparation of bromfenac-loaded liposomes modified with chitosan for ophthalmic drug delivery and evaluation of physicochemical properties and drug release profile. *Asian Journal of Pharmaceutical Sciences*, 8(2), 104-109. doi: <https://doi.org/10.1016/j.ajps.2013.07.013>
- Tsuruta, L. R., Lessa, M. M., & Carmona-Ribeiro, A. M. (1995). Effect of Particle Size on Colloid Stability of Bilayer-Covered Polystyrene Microspheres. *Journal of Colloid and Interface Science*, 175(2), 470-475. doi: <https://doi.org/10.1006/jcis.1995.1477>
- Van Eerdenbrugh, B., Van den Mooter, G., & Augustijns, P. (2008). Top-down production of drug nanocrystals: Nanosuspension stabilization, miniaturization and transformation into solid products. *International Journal of Pharmaceutics*, 364(1), 64-75. doi: <http://dx.doi.org/10.1016/j.ijpharm.2008.07.023>
- Vergara, D., Bellomo, C., Zhang, X., Vergaro, V., Tinelli, A., Lorusso, V., . . . Maffia, M. (2012). Lapatinib/Paclitaxel polyelectrolyte nanocapsules for overcoming multidrug resistance in ovarian cancer. *Nanomedicine: Nanotechnology, Biology and Medicine*, 8(6), 891-899. doi: <https://doi.org/10.1016/j.nano.2011.10.014>
- Weinkauff, D. H., & Paul, D. R. (1990). Effects of Structural Order on Barrier Properties *Barrier Polymers and Structures* (Vol. 423, pp. 60-91): American Chemical Society.
- Wiese, G. R., & Healy, T. W. (1970). Effect of particle size on colloid stability. [10.1039/TF9706600490]. *Transactions of the Faraday Society*, 66(0), 490-499. doi: 10.1039/TF9706600490
- Wilhelm, S., Tavares, A. J., Dai, Q., Ohta, S., Audet, J., Dvorak, H. F., & Chan, W. C. W. (2016). Analysis of nanoparticle delivery to tumours. [Perspective]. *Nature Reviews Materials*, 1, 16014. doi: 10.1038/natrevmats.2016.14
- Wood, K. C., Chuang, H. F., Batten, R. D., Lynn, D. M., & Hammond, P. T. (2006). Controlling interlayer diffusion to achieve sustained, multiagent delivery from layer-by-layer thin films. *Proceedings of the National Academy of Sciences*, 103(27), 10207-10212. doi: 10.1073/pnas.0602884103
- Xu, J., Shen, X., Jia, L., Xu, Z., Zhou, T., Li, X., . . . Zhu, T. (2017). Facile synthesis of folic acid-conjugated fluorapatite nanocrystals for targeted cancer cell fluorescence imaging. *Materials Letters*, 203, 37-41. doi: <http://dx.doi.org/10.1016/j.matlet.2017.05.102>
- Xu, X., Shan, G. R., & Pan, P. (2016). Controlled co-delivery of hydrophilic and hydrophobic drugs from thermosensitive and crystallizable copolymer nanoparticles. *Journal of Applied Polymer Science*, 133(42), n/a-n/a. doi: 10.1002/app.44132

- Yoo, H. S., & Park, T. G. (2001). Biodegradable polymeric micelles composed of doxorubicin conjugated PLGA–PEG block copolymer. *Journal of Controlled Release*, 70(1), 63-70. doi: [http://dx.doi.org/10.1016/S0168-3659\(00\)00340-0](http://dx.doi.org/10.1016/S0168-3659(00)00340-0)
- Zhang, H., Hu, H., Dai, W., Wang, X., & Zhang, Q. (2015). Effects of PEGylated paclitaxel nanocrystals on breast cancer and its lung metastasis. [Research Support, Non-U S Gov't]. *Nanoscale*, 7(24), 10790-10800.
- Zhang, J., & Lynn, D. M. (2007). Ultrathin Multilayered Films Assembled from “Charge-Shifting” Cationic Polymers: Extended, Long-Term Release of Plasmid DNA from Surfaces. *Advanced Materials*, 19(23), 4218-4223. doi: 10.1002/adma.200701028
- Zhang, L., Chan, J. M., Gu, F. X., Rhee, J.-W., Wang, A. Z., Radovic-Moreno, A. F., . . . Farokhzad, O. C. (2008). Self-Assembled Lipid–Polymer Hybrid Nanoparticles: A Robust Drug Delivery Platform. *ACS Nano*, 2(8), 1696-1702. doi: 10.1021/nn800275r
- Zhao, D., Tan, S., Yuan, D., Lu, W., Rezenom, Y. H., Jiang, H., . . . Zhou, H.-C. (2011). Surface Functionalization of Porous Coordination Nanocages Via Click Chemistry and Their Application in Drug Delivery. *Advanced Materials*, 23(1), 90-93. doi: 10.1002/adma.201003012
- Zhao, J., Yang, Y., Han, X., Liang, C., Liu, J., Song, X., . . . Liu, Z. (2017). Redox-Sensitive Nanoscale Coordination Polymers for Drug Delivery and Cancer Theranostics. *Acs Applied Materials & Interfaces*, 9(28), 23555-23563. doi: 10.1021/acsami.7b07535
- Zhao, L., Shen, G., Ma, G., & Yan, X. (2017). Engineering and delivery of nanocolloids of hydrophobic drugs. *Advances in Colloid and Interface Science*. doi: <https://doi.org/10.1016/j.cis.2017.04.008>
- Zhu, Z. (2014). Flash Nanoprecipitation: Prediction and Enhancement of Particle Stability via Drug Structure. *Molecular Pharmaceutics*, 11(3), 776-786. doi: 10.1021/mp500025e

CHAPTER 2. PREPARATION OF NANOCORE FORMULATION STABILIZED BY TA/Fe³⁺ INTERFACIAL ASSEMBLIES

A version of this chapter will be submitted for review.

2.1 Introduction

Nanoprecipitation of hydrophobic drug molecules results in high drug loading nanocarriers. However, the main limitation of the formed particles is their susceptibility to Ostwald ripening in aqueous conditions and potential aggregation. Most of the polymers used to stabilize such particles can easily desorb from the surface and lose their function. A polymer with high binding affinity for the precipitated drug NP can resist desorption in aqueous conditions and result in a more stable nanocarrier. Due to the intrinsic affinity for solid surface, polyphenols were employed to coat nanoparticles providing reactive platforms for further functionalization with ligands (Abouelmagd, Meng, Kim, Hyun, & Yeo, 2016; Park et al., 2014). Camptothecin nanocrystals stabilized by a polydopamine layer was recently reported and showed high aqueous dispersibility and stability in contrast to the naked crystals that precipitated within 24 h (Zhan, Jagtiani, & Liang, 2017). The polydopamine layer was also used to mediate grafting of a tumor targeting peptide to the surface of the nanocrystals, thereby enhancing their cellular uptake. The catechol groups in polydopamine undergo Michael addition or Schiff's base reaction with amine or thiol terminated compounds. However, a major limitation of polydopamine coatings is the potential residual neuroactivity of dopamine in the human body, which might hinder the clinical translation of such systems (Gao et al., 2006). Another polyphenol explored for surface coatings is tannic acid (TA), which deposits efficiently on solid surfaces via oxidation-induced oligomerization to form colorless coats (Sileika, Barrett, Zhang, Lau, & Messersmith, 2013). The large number of galloyl groups in TA molecules can interact with different molecules by hydrogen bonding and hydrophobic interactions; therefore, TA coating serves as a versatile platform for surface functionalization (Abouelmagd et al., 2016; Liang et al., 2016). Recently, Caruso *et al.* (Ejima et al., 2013) reported the use of TA coordination complexes with Fe³⁺ ion as an efficient and rapid tool for coating a variety of substrates (Figure 5a-c). Each TA molecule can interact with several Fe³⁺ centers, evidenced by immediate formation of dark blue color. TA-Fe³⁺ complexes deposited on a solid surface form an instantaneous stable

film. There are three possible coordination states between Fe^{3+} and TA: mono-, bis- or tris-complexes (Figure 5d), which are assembled and disassembled at different pHs. Therefore, TA- Fe^{3+} complexes provide pH-sensitive surface layer (Ejima et al., 2013).

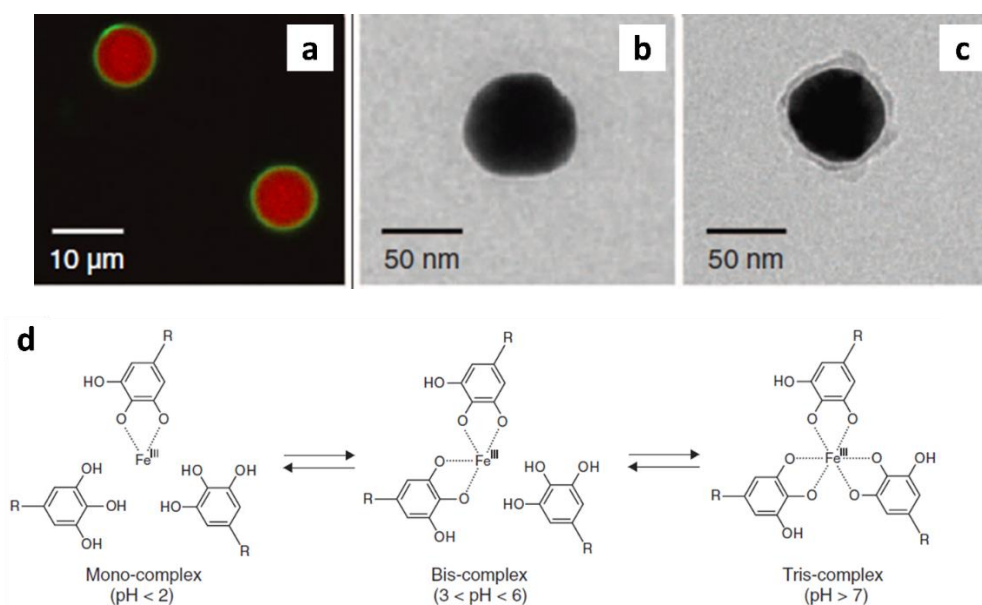


Figure 5: TA- Fe^{3+} is an efficient tool for coating a variety of substrates. (a) Confocal laser scanning microscopy image of CaCO_3 particles (red) coated with TA- Fe^{3+} films (green), (b and c) TEM images of Au NP before (b) and after (c) coating with a TA- Fe^{3+} film, and (d) The dominant TA- Fe^{3+} complexation state depends on pH (R represents the remainder of the TA molecule). From ref (Ejima et al., 2013). Reprinted with permission from AAAS.

Due to the instantaneous assembly of TA- Fe^{3+} films, these coordination complexes were used in combination with nanoprecipitation methods for preparation of NP with high drug loading and long-term colloidal stability. Yan *et al.* (Shen et al., 2016) induced precipitation of paclitaxel by antisolvent addition in the presence of TA and Fe^{3+} . The formed paclitaxel nuclei were rapidly captured by TA, which in turn instantaneously complexed with Fe^{3+} in a one-pot preparation method (Figure 6a). The interfacial assembly of TA- Fe^{3+} complexes on the paclitaxel nanocores surfaces restrained Ostwald ripening. The surface-stabilized nanocores, PTX@TA- Fe^{3+} , had an average size of 100 nm (Figure 6b), with a drug loading capacity up to 80%. They were stable in aqueous suspension for over 6 months without crystallization or aggregation. Each paclitaxel molecule has 21 hydrogen bonding sites that allowed strong anchoring of TA on paclitaxel nanocores formed upon precipitation (Figure 6c). Using a dissipative particle dynamics simulation, they showed that the TA- Fe^{3+} complexation state would affect the particle stability. The bis-

complex is the most favorable for stably covering the surface as it provides the balance between TA-Fe³⁺ complexation and their supramolecular interaction for interfacial assembly (Figure 6d). To prove the importance of Fe³⁺ complexation, PTX@TA-Fe³⁺ was compared to particles prepared similarly but in the absence of Fe³⁺. The nanocores stabilized by TA alone were stable only for 1 h and did not prevent Ostwald ripening. This is because TA alone formed a monolayer that could not efficiently cover PTX surface, while TA-Fe³⁺ deposits in a supramolecular structure. PTX@TA-Fe³⁺ accumulated and was retained in the MCF-7 tumor resulting in superior antitumor activity compared to the commercial formulation Taxol®.

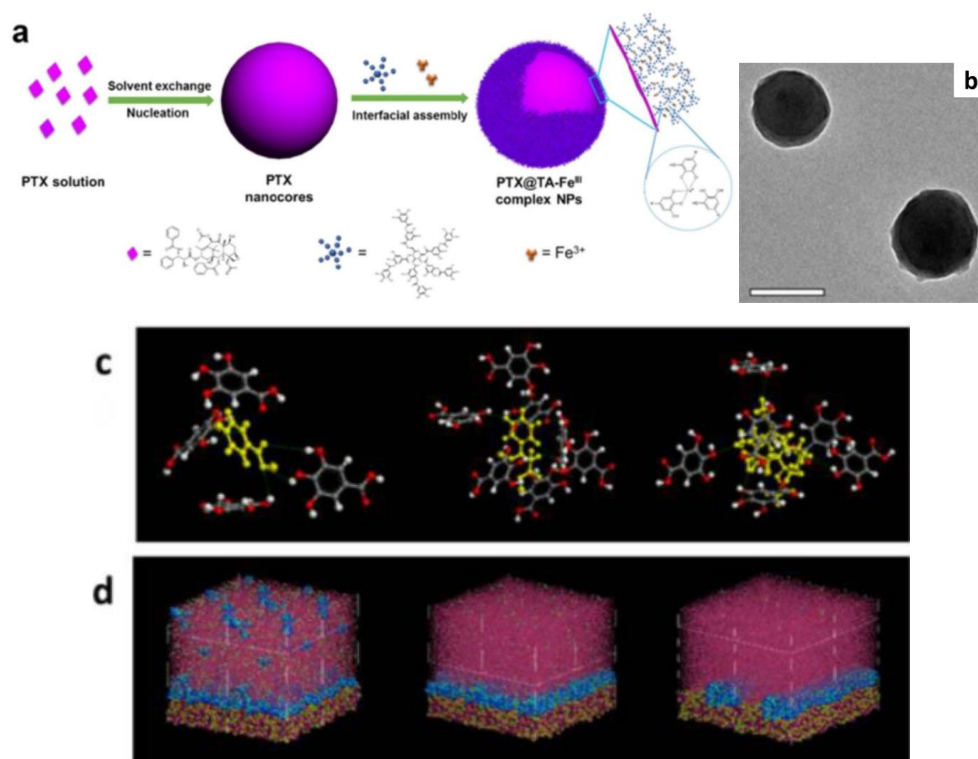


Figure 6: (a) Schematic for the general procedure for fabrication of PTX@TA-Fe³⁺ nanoparticles, (b) Morphology of PTX@TA-Fe³⁺ nanoparticles shown by TEM (scale bar 100 nm), (c) TA anchors onto the surface of preformed PTX nanocores via multiple hydrogen binding sites, and (d) Dissipative particle dynamics simulation of the TA assembly process (Middle: bis-complex with tight multilayer structure of TA molecules deposited on the PTX surface, Right: tris-complex with compacted TA aggregates deposited on the PTX surface, Left: mono-complex with TA molecules no longer covering the whole PTX surface, and PTX molecules are exposed to the solvent. Adapted with permission from ref (Shen et al., 2016). Copyright (2016) American Chemical Society.

The same group recently reported the use of the interfacial cohesive assembly for delivering the hydrophobic photosensitizer drug, Chlorin e6 (Ce6) (Liu et al., 2017). The NP,

Ce6@TA-Fe³⁺, had 65% drug loading and was ~60 nm in size. The aggregation of Ce6 within the nanocore resulted in fluorescence quenching, which was gradually recovered after particle internalization into cells due to release of Ce6 in the cytoplasm. This indicated that Ce6@TA-Fe³⁺ would efficiently protect Ce6 in circulation and allow NP accumulation in tumor before Ce6 release within the cells cytoplasm. Ce6 has 13 potential sites for hydrogen bonds formation (Pubchem), which most likely allowed the efficient TA-Fe³⁺ interfacial assembly. Therefore, hydrophobic drugs with structures that allow for TA binding, via hydrogen bonding or other possible interactions such as hydrophobic interactions and π - π stacking, would be good candidates for the preparation of nanocores. Given the versatility of interactions offered by TA, the TA-Fe³⁺-stabilized NP can further modified with functional ligands to achieve targeting, stimuli-responsiveness or controlled drug release.

Excipients used for NP preparation are required to be inactive, so they do not pose any unintended side effects (Vauthier & Ponchel, 2017). However, most excipients used in pharmaceutical preparations cannot be assumed completely inert (Milić, Čalija, & Đorđević, 2017). Although nanocores stabilized by TA-Fe³⁺ interfacial assemblies are promising as high drug loading NP (Shen et al., 2016), the fraction of TA included in the formulation is still high (~ 50%). Therefore, it is important to identify the functions of TA and its potential influence on the patients' health as well as on the efficacy of the nanocarrier formulation.

TA is a polyphenolic compound extracted from plants and has been used for decades as a flavoring agent in food industry and a clarifying agent in wine industry (FDA, 1977). TA has been used based on the astringent taste and the ability to interact with proteins and precipitate them. TA is considered a GRAS (Generally Regarded as Safe) substance by the FDA where its hydrolysis products, glucose and quinic acid, are consumed naturally in many foods ("GRAS substances database," 1977). TA has also been utilized in various biomedical applications. In 1925, TA was first used to treat burn wounds due to the ability to crosslink collagen and denatured protein in the denuded skin leading to pain relief and accelerated healing process (Heijmen, du Pont, Middelkoop, Kreis, & Hoekstra, 1997; Hupkens, Boxma, & Dokter, 1995; Lindsay, 1927). TA also possesses mucoadhesive and hemostatic functions, which make it a good candidate for treating gastro-esophageal reflux diseases (Shin, Kim, Shim, Yang, & Lee, 2016; Shin et al., 2015). Antibacterial, antifungal and antiviral effects of TA have also been reported (Dong et al., 2017; Scalbert, 1991; von Martius, Hammer, & Locher, 2012). TA inhibits microbial enzymes, interferes with microbial

metabolism and deprives bacterial cells from iron by chelation (Scalbert, 1991). The phenolic hydroxyl groups of TA interact with viral proteins and inactivate viruses (Konishi & Hotta, 1979). Orłowski *et al.* prepared TA-modified silver nanoparticles and showed that they effectively treated Herpes Simplex virus type-2 both *in vitro* and *in vivo* (Orłowski *et al.*, 2014). TA binding to viral surface glycoproteins facilitated the attachment of silver nanoparticles and thus enhanced the antiviral activity of silver. The hydroxyl scavenging activity and efficient iron chelation make TA a well-known antioxidant (K Sah, Kumar, Subramanian, & Devasagayam, 1995; Lopes, Schulman, & Hermes-Lima, 1999). This antioxidant activity in turn protects DNA from oxidative stress damage, which makes TA anti-carcinogenic and anti-mutagenic as well (Khan, Ahmad, & Hadi, 2000; Lopes *et al.*, 1999). In addition, TA can potentially provide the anti-carcinogenic effect by interfering with carcinogen binding to tissue DNA or modulating the enzymatic pathways involved in carcinogen activation and/or detoxification (Krajka-Kuźniak & Baer-Dubowska, 2003; Mukhtar *et al.*, 1988). TA was also proved to inhibit the CXCL12/CXCR4 interaction, suppressing tumor cell migration and angiogenesis (Chen *et al.*, 2003). These properties increased the interest in using TA for NP preparation. TA was encapsulated in NP by FNP via forming coordination complexes with Fe(III) (Tang, Amin, Messersmith, Anthony, & Prud'homme, 2015). The NP were taken up by fibroblasts with low cytotoxicity yet high antioxidant activity. TA was found to modulate the activity and signaling pathways of EGFR, a transmembrane glycoprotein involved in progression of several tumors (Yang, Wei, Zhang, Chen, & Chen, 2006). This inspired the formulation of TA NP conjugated to EGFR antibody for EGFR targeting (Aguilera *et al.*, 2016). The targeted TA NP showed high toxicity to the tested cancer cells (A-431 cells), while they were non-toxic to fibroblasts. A study by Sahiner *et al.* (Sahiner, Sagbas, & Aktas, 2015) also showed that polymerized TA had a favorable safety profile in fibroblast cell line. The literature supports that TA is a safe material and can be considered a natural remedy. Its use in combination with chemotherapeutic agents can improve the overall therapeutic efficiency without posing toxicity issues.

The aim of this study was to prepare high drug loading NP with colloidal stability. We optimized the preparation scheme for nanocore formulations stabilized with TA/Fe³⁺ interfacial assemblies using different drugs to show reproducibility. The ability to load two drugs in a controllable ratio in the nanocore formulation was shown. The drug loading and colloidal stability of the nanocores were evaluated.

2.2 Materials and Methods

2.2.1 Materials

PTX was a gift of Samyang Biopharm (Seoul, Korea). Camptothecin (CPT) was purchased from Enzo Life Sciences. Carfilzomib (CFZ) was purchased from Shenzhen Chemical Co. LTD. (Shanghai, China). Tannic acid (TA) and Iron chloride (FeCl_3) was purchased from Sigma Aldrich. Pierce BCA protein assay kit was purchased from Thermo Scientific (NY, USA). All other materials were of analytical grade.

2.2.2 TA/ Fe^{3+} -stabilized nanocore preparation

(Figure 7)

For PTX nanocore (PTX-pTA), PTX was mixed with TA in 20 μL ethanol at a molar ratio of 2. For CPT nanocore (CPT-pTA), CPT was mixed with TA in 20 μL dimethyl sulfoxide (DMSO) at a molar ratio of 4.9. To the drug and TA mixture, 980 μl water containing 100 μg FeCl_3 (final molar ratio of TA: Fe^{3+} is 1.1) was added. Probe-sonication at 40% amplitude for 5 min (1s on/1s off pulse) was applied while keeping the suspension cooled over ice to avoid overheating. For CFZ nanocore (CFZ-pTA), CFZ was mixed with TA in 30 μL ethanol at a molar ratio of 2.4. To this mixture, 10 mL water containing 100 μg FeCl_3 (final molar ratio of TA: Fe^{3+} is 1.1) was added and mixed briefly without sonication. For the drug-co-loaded nanocore, PTX-CFZ-pTA, a mixture of CFZ and PTX in ethanol was used and proceeded the same as for CFZ-pTA nanocore preparation. All particles were centrifuged (at 43,400 rcf for 20 min at 4 °C) to remove excess TA, FeCl_3 and un-entrapped drug. The pellets were suspended in water and stored at 4°C for further characterization. The CFZ nanoclusters in absence of pTA were prepared by adding water to CFZ solution in ethanol at same concentration and volume ratio used in CFZ-pTA.

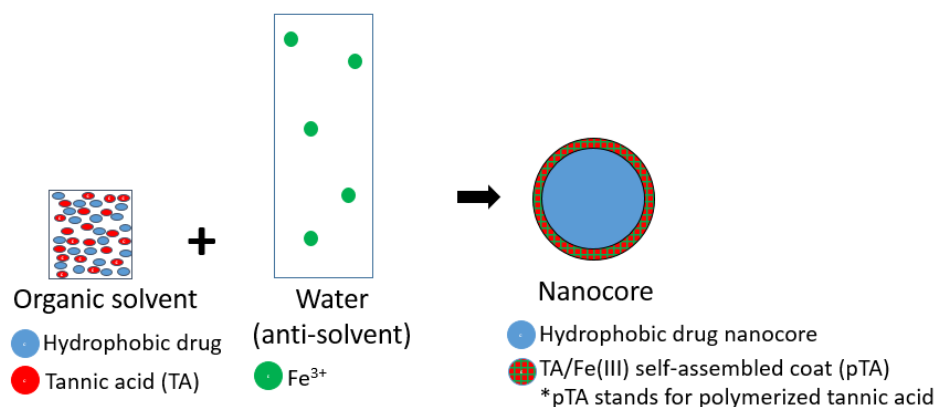


Figure 7: Schematic for preparation of TA/Fe³⁺-stabilized nanocore

2.2.3 TA/Fe³⁺-stabilized nanocore characterization

2.2.3.1 Particle size and surface charge

The hydrodynamic diameter (*z-ave*), polydispersity index (PDI) and zeta potential of particles were measured by dynamic light scattering (DLS) in sodium phosphate buffer (10 mM, pH 7.4) using a Zetasizer Nano-ZS90 (Malvern Instruments, Worcestershire, UK).

2.2.3.2 Morphology

Particles morphology was examined using transmission electron microscopy (TEM). Aqueous suspension of freshly prepared particles was mounted on a carbon coated copper grid (400 mesh), negatively stained with 1% uranyl acetate and allowed to dry in air. The dried grid was examined under an FEI Tecnai T20 transmission electron microscope (OR, USA). CFZ-pTA was used to visualize the core-shell structure of the particles. The core was etched by incubating the particles in PBS containing 0.2% tween 80 for 6 h. Particles were collected by centrifugation and pellet was resuspended in water then mounted on the grid and processed as above.

2.2.3.3 Drug loading capacity

Drug loading capacity in the nanocores was determined using C18 reversed phase HPLC (25 cm × 4.6 mm, particle size: 5 μm). Nanocores of premeasured mass were mixed (at a concentration of ~ 50 ug/ml) with ethylenediaminetetraacetic acid solution (EDTA) (100 mM, pH 7.4), urea solution (5M) and acetonitrile. EDTA was used to intercalate Fe³⁺ from pTA and destabilize the particles, urea was used to disrupt hydrogen bonds between TA and the drug, and

acetonitrile was used to extract the drug. The mixture was filtered on 0.45 μm syringe filter prior to analysis. used to extract the drug. The mixture was filtered on 0.45 μm syringe filter prior to analysis. For PTX, the mobile phase consisted of a mixture of acetonitrile and water (50:50) run at a flow rate of 1 mL/min. For CFZ, similar mixture containing 0.05% trifluoroacetic acid was run in a gradient from 60-20% of water at 0.7 mL/min. PTX and CFZ were detected with UV detector at wavelength of 227 nm and 210 nm, respectively.

2.2.3.4 Tannic acid content

The content of tannic acid in CFZ-pTA was estimated by the bicinchoninic acid (BCA) assay (Pierce® BCA assay kit). 0.1 mg CFZ-pTA was suspended in 100 μL water and treated with 100 μL of 0.1 N HCl to dissolve TA. Working BCA reagent was and mixed with the samples in 8:1 v/v ratio at 37 °C for 30 min. The UV absorbance of the solution was read at 570 nm using SpectraMax M3 microplate reader (Molecular Device, Sunnyvale, CA). TA standards were prepared and treated similarly to construct a calibration curve. To exclude interference from CFZ, CFZ solution (at similar concentration in the tested particles as determined by HPLC) was treated similarly and the resulting signals was subtracted from the CFZ-pTA samples reading.

2.2.3.5 Colloidal stability of nanocores in serum-containing medium

PTX-pTA or CFZ-pTA (at concentration equivalent to 60 $\mu\text{g}/\text{mL}$ drug, n=3 per group) were incubated in 50% fetal bovine serum (FBS) in PBS at 37 °C for 24 h with periodical measurement of their particle size using Zetasizer.

2.3 Results

2.3.1 Preparation and characterization of TA/ Fe^{3+} -stabilized nanocores

The successful formation of NP was indicated by the blue color formation which corresponds to the coordination interaction between TA and Fe^{3+} . The prepared nanocores were labeled PTX-pTA, CFZ-pTA and CPT-pTA, referring to drug-rich nano-cores coated with interfacially assembled polymerized TA. The z-average of the nanocores measured by DLS was less than 200 nm (Table 1). The surface was negatively charged due to the numerous hydroxyl groups of TA, which indicates successful assembly of TA on the nanocore surface. TEM images showed spherical particles with smaller size (50-100 nm) than the size measured by DLS (Figure

8). This is most likely due to some NP aggregation induced in the aqueous medium. By adding water to a highly concentrated solution of CFZ in ethanol (in absence of TA and FeCl_3), spherical CFZ nanoclusters separated from the solution (Figure 9a). CFZ nanoclusters had z-average of 161 ± 11 nm and zeta potential of 17 ± 8 mV when measured in water using DLS. Upon addition of phosphate buffer, the bare CFZ nanoclusters showed almost neutral charge and aggregated.

The drug loading capacity in the PTX-pTA and CFZ-pTA nanocores were around 50% w/w, as measured by HPLC (Table 1). The TA content in the CFZ-pTA nanocores was estimated as 49 ± 7 wt% according to the BCA assay. To visualize pTA capsule, CFZ-pTA nanocore was etched with tween solution that can actively dissolve CFZ in the core without affecting the pTA shell. The etched particles showed a collapsed structure with empty core (Figure 9b).

Table 1: Particle size, zeta potential and drug content of nanocores (Size and charge measured in 10 mM phosphate buffer, pH 7.4).

	PTX-pTA	CPT-pTA	CFZ-pTA
Particle size (nm)	172 ± 9	176 ± 16	164 ± 9
Zeta potential (mV)	-31 ± 3	-27 ± 7	-25 ± 0
Drug loading (%w/w)	54 ± 10	ND	51 ± 1

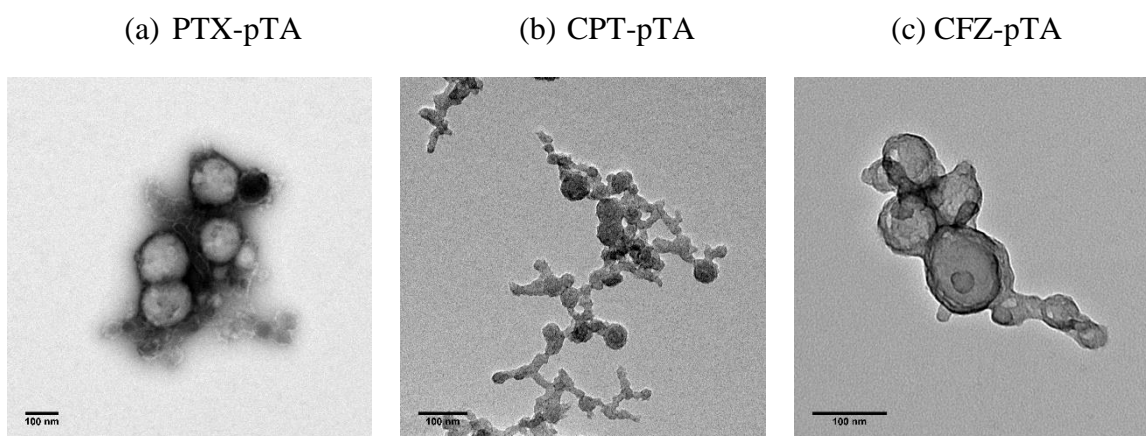


Figure 8: TEM images of nanocores of different drugs (Scale bar: 100 nm).

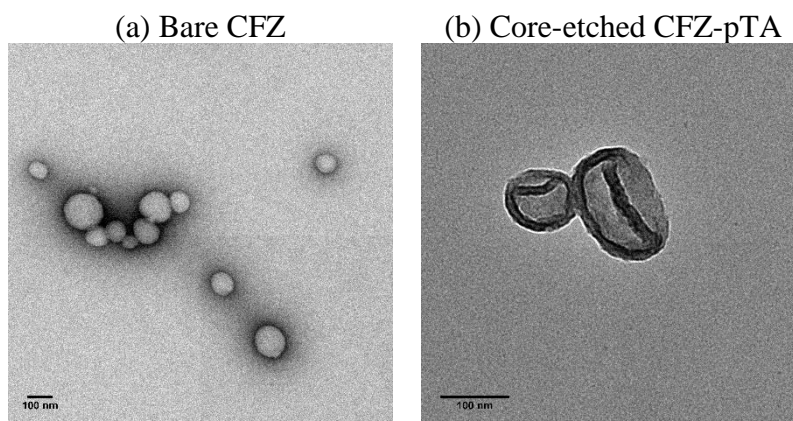


Figure 9: TEM image of (a) bare CFZ nanoclusters and (b) core-etched CFZ-pTA (Scale bar: 100 nm).

2.3.2 Colloidal stability of TA/Fe³⁺-stabilized nanocores

PTX-pTA or CFZ-pTA nanocores were incubated in 50% FBS at 37°C and inspected at different time points with respect to the size. Particle size was stable over 24 h (Figure 10a and b). Alternatively, the stability of nanocores in serum was estimated from the morphology. CFZ-pTA was incubated in FBS for 24 h and imaged by TEM. CFZ-pTA maintained the spherical structure with similar size to fresh particles (Figure 10c). This indicates that TA/Fe³⁺-stabilized nanocores remain stable in serum without disintegration or aggregation.

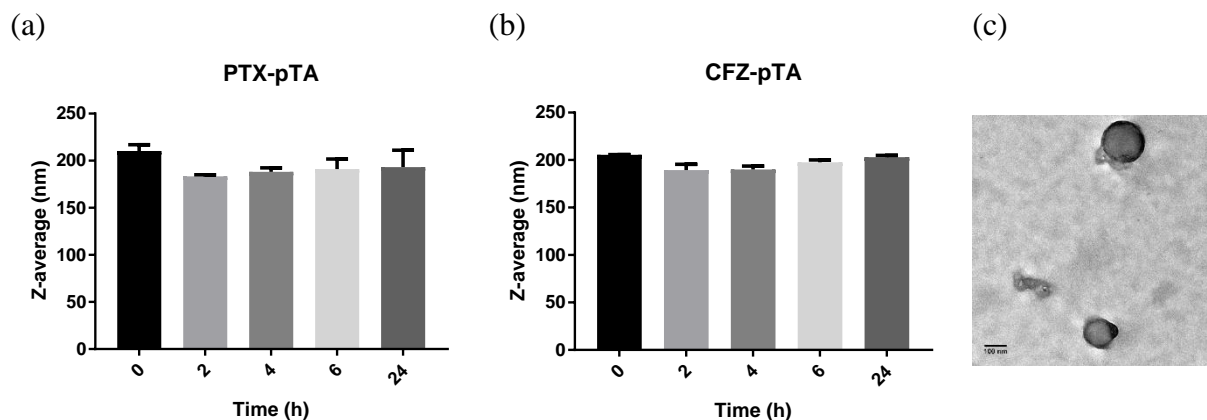


Figure 10: Colloidal stability of nanocores: Z-average of (a) PTX-pTA and (b) CFZ-pTA nanocores incubated in 50% FBS at 60 $\mu\text{g/mL}$ of drug equivalent concentration, measured by DLS at different time points, and (c) TEM image of CFZ-pTA after 24 h incubation in FBS (Scale bar = 100 nm).

2.3.3 Co-loading drugs in TA/Fe³⁺-stabilized nanocores

An ethanolic mixture of PTX, CFZ and TA was mixed with an aqueous solution of FeCl₃ to form nanocores with an average size of 177 ± 27 nm and zeta potential of -16 ± 1 mV, referred to as PTX-CFZ-pTA. TEM images of the formed nanocores showed spherical particles with no free PTX or CFZ crystals, indicating that both drugs were successfully encapsulated in the TA/Fe³⁺-stabilized nanocores (Figure 11a). PTX and CFZ were loaded with high contents (up to 40% and 60% w/w respectively). The ratio of loaded CFZ/PTX was proportional to the feed ratio of CFZ/PTX (Figure 11b).

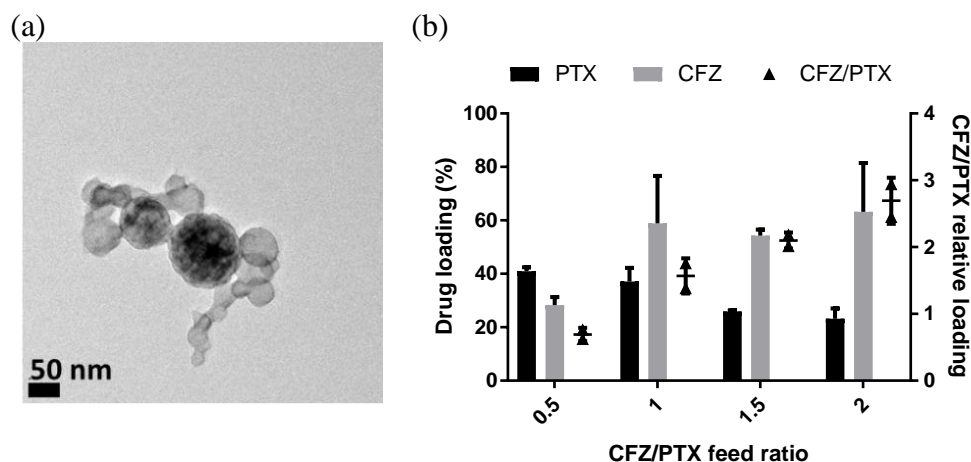


Figure 11: Co-loading drugs in TA/Fe³⁺-stabilized nanocore: (a) TEM image of PTX-CFZ-pTA and (b) Drug loading capacity and the ratio of PTX and CFZ loading in PTX-CFZ-pTA nanocores at different starting feed ratios.

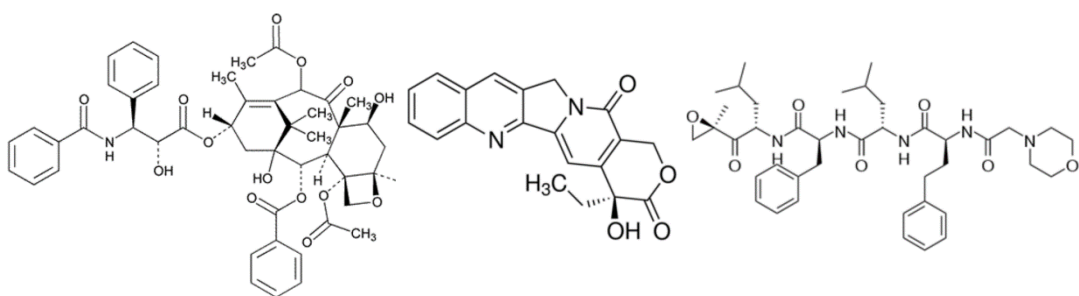
2.4 Discussion

The use of NP for delivering chemotherapeutics has been pursued for decades (Cheng, Al Zaki, Hui, Muzykantov, & Tsourkas, 2012). The main roles for NP are loading drugs and retaining them; however, many of the studied systems fail to meet these criteria. An NP system that loads drugs at high capacity and maintain stability in circulation can enhance drugs accumulation at the tumor site via the EPR effect and increase the clinical efficacy (Bae & Park, 2011). TA is a polyphenol from natural origin and can form coordination complexes with Fe³⁺ ions that stabilize the interface between drug rich core droplets and aqueous solution. Due to the instantaneous assembly of TA-Fe³⁺ films on interfaces, these complexes were used in combination with nanoprecipitation methods for preparation of NP with high paclitaxel loading and colloidal stability (Shen et al., 2016).

Hydrophobic drugs with low solubility can form highly supersaturated solutions upon addition of water as a miscible antisolvent to their solutions (Myerson, 1999). The drug concentration used, type of solvent to solubilize the drug and the solvent/antisolvent ratio vary based on the drug's solubility characteristics. The high supersaturation is usually followed by separation of drug nanoclusters from the mixture followed by crystal growth (Myerson, 1999). For TA to act as a good stabilizer that halts the crystal growth and avoids Ostwald ripening, it should anchor rapidly and efficiently to the surface of the separated drug nanoclusters (Sun & Yeo, 2012). This was offered by the hydrophobic and hydrogen bonding moieties possessed by the three model compounds that allowed interaction with the catechol and pyrogallol moieties in TA. Following the TA anchoring to the surface, TA polymerizes into a supramolecular structure complexed with the Fe^{3+} ions via coordination bonds (Ejima et al., 2013). The polymerized TA- Fe^{3+} assemblies were referred to in the text as 'pTA'.

PTX nanocores prepared in (Shen et al., 2016) was reproduced with some modifications in the order of mixing. The original method describes the addition of PTX ethanolic solution to water (anti-solvent) followed by TA and Fe^{3+} addition. By following this procedure, aggregation was observed, most likely because the rate of crystal growth was faster than the rate of TA and Fe^{3+} addition and complexation. The order of the addition was reversed in this study, with an aqueous solution of FeCl_3 added to the concentrated ethanolic mixture of PTX and TA. This prevented the formation of PTX aggregates and allowed instantaneous coating of the formed PTX nuclei with the TA/ Fe^{3+} assemblies. The same approach was used for preparing CFZ and CPT nanocores, with variations in the solvent type and anti-solvent volume. CPT was dissolved in DMSO instead of ethanol. For CFZ the volume of added water was 10 times more than those of PTX and CPT. While PTX and CPT nanocores required vigorous sonication to avoid aggregation, CFZ nanocore was formed by simple mixing of the anti-solvent. Those drugs have different molecular weights; however, they share the poor aqueous solubility and the large number of hydrogen bonding groups as well as aromatic rings capable of hydrophobic interactions (Table 2).

Table 2: Molecular weights, solubility and chemical structures of model drugs used.

Model drug	PTX	CPT	CFZ
Molecular weight (g/mol)	853.91	348.35	719.91
Solubility ($\mu\text{g/mL}$)	0.3-30	1.2-3.8	0.7-3.6
Structure			
Reference	(Abouelmagd, Sun, Chang, Ku, & Yeo, 2015)	(Schneider et al., 2008; Zhan, Zhou, et al., 2017)	

In case of CFZ, the nucleation was spontaneous upon supersaturation and did not require sonication assistance in contrast to PTX and CPT. However, CFZ nanoclusters immediately aggregated in PB where the high ion concentration screened the surface positive charge and avoided the particles repulsion. However, CFZ-pTA was stable in PB which indicates strong anchoring of the TA-Fe³⁺ assemblies on the surface.

The nanocores possessed a core-shell structure (Figure 9b), with the cores being formed solely of drug and thus offering high drug loading capacity. The drug content quantified in case of PTX-pTA and CFZ-pTA nanocores was at least 50% w/w of the NP. The nanocore formulation avoids Ostwald ripening due to the strong interaction of TA with drug molecules that can maintain the NP colloidal stability and avoid premature drug release. The stability of nanocores in serum was tested by monitoring their size, using DLS, over time as well as examining their morphology, using TEM. Nanocores maintained its size and did not aggregate in FBS for 24 h (Figure 10a and b). This result indicates that the pTA assemblies efficiently covered the drug in the core to avoid crystal growth and Ostwald ripening. TEM images taken after 24 h incubation in FBS showed that CFZ-pTA maintained its structure without size increase or aggregation (Figure 10c). It also

showed a fully swollen core indicating that the pTA coat strongly anchored to the CFZ core avoiding rapid CFZ dissolution.

Multi-drug-loaded NP will help synchronize the biodistribution and pharmacokinetics of multiple drugs so that they can exert synergistic effects on the same cell populations (Hu, Aryal, & Zhang, 2010) (Ashley et al., 2016). Like the single drug-loaded nanocores, the addition of an anti-solvent to a solution of two drug mixture in presence of TA and Fe^{3+} resulted in multi-drug-loaded nanocores (PTX-CFZ-pTA). Typically, PTX requires high power sonication to form small nuclei during nanocore preparation. However, the presence of CFZ helped form PTX-CFZ-pTA nanocores without sonication. It is likely that the facile nucleation of CFZ has induced simultaneous PTX nucleation, which may also have helped to co-load both PTX and CFZ in same nanocores rather than individual population of each drug. This is also indicated by the proportional increase in relative CFZ/PTX loading contents with the feed ratio of CFZ/PTX (Figure 11b).

2.5 Conclusions

In summary, TA/ Fe^{3+} interfacial assemblies successfully formed to encapsulate drug nuclei and make spherical nanocores, as evidenced by size and morphology of PTX-pTA, CFZ-pTA and CPT-pTA nanocores. The nanocores had high drug loading capacity and loaded 2 drugs in a controllable ratio. The TA/ Fe^{3+} assemblies covered the drug in the core to avoid Ostwald ripening and prevent aggregation. Strong interaction between the drug and TA helped maintain the drug in the nanocores for 24 h in 50% FBS.

2.6 References

- Abouelmagd, S. A., Meng, F., Kim, B.-K., Hyun, H., & Yeo, Y. (2016). Tannic Acid-Mediated Surface Functionalization of Polymeric Nanoparticles. *ACS Biomaterials Science & Engineering*, 2(12), 2294-2303. doi: 10.1021/acsbiomaterials.6b00497
- Abouelmagd, S. A., Sun, B., Chang, A. C., Ku, Y. J., & Yeo, Y. (2015). Release Kinetics Study of Poorly Water-Soluble Drugs from Nanoparticles: Are We Doing It Right? *Molecular Pharmaceutics*, 12(3), 997-1003. doi: 10.1021/mp500817h
- Aguilera, J. R., Venegas, V., Oliva, J. M., Sayagues, M. J., de Miguel, M., Sanchez-Alcazar, J. A., . . . Zaderenko, A. P. (2016). Targeted multifunctional tannic acid nanoparticles. [10.1039/C5RA19405A]. *RSC Advances*, 6(9), 7279-7287. doi: 10.1039/c5ra19405a
- Ashley, J. D., Quinlan, C. J., Schroeder, V. A., Suckow, M. A., Pizzuti, V. J., Kiziltepe, T., & Bilgicer, B. (2016). Dual Carfilzomib and Doxorubicin-Loaded Liposomal Nanoparticles for Synergistic Efficacy in Multiple Myeloma. [Research Support, U S Gov't, Non-P H S Research Support, Non-U S Gov't]. *Mol Cancer Ther*, 15(7), 1452-1459.
- Bae, Y. H., & Park, K. (2011). Targeted drug delivery to tumors: Myths, reality and possibility. *Journal of Controlled Release*, 153(3), 198-205. doi: 10.1016/j.jconrel.2011.06.001
- Chen, X., Beutler, J. A., McCloud, T. G., Loehfelm, A., Yang, L., Dong, H.-F., . . . Howard, O. M. Z. (2003). Tannic Acid Is an Inhibitor of CXCL12 (SDF-1 α)/CXCR4 with Antiangiogenic Activity. *Clinical Cancer Research*, 9(8), 3115.
- Cheng, Z., Al Zaki, A., Hui, J. Z., Muzykantov, V. R., & Tsourkas, A. (2012). Multifunctional nanoparticles: cost versus benefit of adding targeting and imaging capabilities. [Research Support, N.I.H., Extramural Review]. *Science*, 338(6109), 903-910. doi: 10.1126/science.1226338
- Dong, G., Liu, H., Yu, X., Zhang, X., Lu, H., Zhou, T., & Cao, J. (2017). Antimicrobial and anti-biofilm activity of tannic acid against *Staphylococcus aureus*. *Natural Product Research*, 1-4. doi: 10.1080/14786419.2017.1366485
- Ejima, H., Richardson, J. J., Liang, K., Best, J. P., van Koeverden, M. P., Such, G. K., . . . Caruso, F. (2013). One-Step Assembly of Coordination Complexes for Versatile Film and Particle Engineering. [10.1126/science.1237265]. *Science*, 341(6142), 154.
- FDA. (1977). *Evaluation of the health aspects of tannic acid as a food ingredient*. (223-75-2004). Department of Health, Education and Welfare: Retrieved from https://www.faseb.org/Portals/2/PDFs/LSRO_Legacy_Reports/1977_SCOGS-48%20Tannic%20Acid.pdf.
- Gao, J., Kim, Y. M., Coe, H., Zern, B., Sheppard, B., & Wang, Y. (2006). A neuroinductive biomaterial based on dopamine. *Proceedings of the National Academy of Sciences of the United States of America*, 103(45), 16681-16686. doi: 10.1073/pnas.0606237103
- GRAS substances database. (1977). Retrieved October 26th 2017, from FDA <https://www.fda.gov/Food/IngredientsPackagingLabeling/GRAS/SCOGS/ucm261485.htm>
- Heijmen, F. H., du Pont, J. S., Middelkoop, E., Kreis, R. W., & Hoekstra, M. J. (1997). Cross-linking of dermal sheep collagen with tannic acid. *Biomaterials*, 18(10), 749-754. doi: [https://doi.org/10.1016/S0142-9612\(96\)00202-5](https://doi.org/10.1016/S0142-9612(96)00202-5)
- Hu, C. M., Aryal, S., & Zhang, L. (2010). Nanoparticle-assisted combination therapies for effective cancer treatment. [Review]. *Ther Deliv*, 1(2), 323-334.

- Hupkens, P., Boxma, H., & Dokter, J. (1995). Tannic acid as a topical agent in burns: historical considerations and implications for new developments. *Burns*, 21(1), 57-61. doi: [https://doi.org/10.1016/0305-4179\(95\)90784-W](https://doi.org/10.1016/0305-4179(95)90784-W)
- K Sah, N., Kumar, S., Subramanian, M., & Devasagayam, T. P. A. (1995). *Variation in the modulation of superoxide-induced singlestrand breaks in plasmid pBR322 DNA by biological antioxidants* (Vol. 35).
- Khan, N. S., Ahmad, A., & Hadi, S. M. (2000). Anti-oxidant, pro-oxidant properties of tannic acid and its binding to DNA. *Chemico-Biological Interactions*, 125(3), 177-189. doi: [https://doi.org/10.1016/S0009-2797\(00\)00143-5](https://doi.org/10.1016/S0009-2797(00)00143-5)
- Konishi, E., & Hotta, S. (1979). Effects of Tannic Acid and Its Related Compounds upon Chikungunya Virus. *Microbiology and Immunology*, 23(7), 659-667. doi: 10.1111/j.1348-0421.1979.tb00507.x
- Krajka-Kuźniak, V., & Baer-Dubowska, W. (2003). The effects of tannic acid on cytochrome P450 and phase II enzymes in mouse liver and kidney. *Toxicology Letters*, 143(2), 209-216. doi: [https://doi.org/10.1016/S0378-4274\(03\)00177-2](https://doi.org/10.1016/S0378-4274(03)00177-2)
- Laboratories, L. Carfilzomib, Free Base, >99%, from <https://www.lclabs.com/products/c-3022-carfilzomib-free-base>
- Liang, H., Pei, Y., Li, J., Xiong, W., He, Y., Liu, S., . . . Li, B. (2016). pH-Degradable antioxidant nanoparticles based on hydrogen-bonded tannic acid assembly. [10.1039/C6RA02527G]. *RSC Advances*, 6(37), 31374-31385. doi: 10.1039/c6ra02527g
- Lindsay, J. C. (1927). TANNIC ACID TREATMENT OF BURNS. *Canadian Medical Association Journal*, 17(1), 86-86.
- Liu, Y., Ma, K., Jiao, T., Xing, R., Shen, G., & Yan, X. (2017). Water-Insoluble Photosensitizer Nanocolloids Stabilized by Supramolecular Interfacial Assembly towards Photodynamic Therapy. *Scientific Reports*, 7, 42978. doi: 10.1038/srep42978
- Lopes, G. K. B., Schulman, H. M., & Hermes-Lima, M. (1999). Polyphenol tannic acid inhibits hydroxyl radical formation from Fenton reaction by complexing ferrous ions. This study is dedicated to the memory of Botany Professor Luiz F.G. Labouriau (1921–1996). *Biochimica et Biophysica Acta (BBA) - General Subjects*, 1472(1), 142-152. doi: [https://doi.org/10.1016/S0304-4165\(99\)00117-8](https://doi.org/10.1016/S0304-4165(99)00117-8)
- Milić, J., Čalića, B., & Đorđević, S. M. (2017). Chapter 4 - Diversity and Functionality of Excipients for Micro/Nanosized Drug Carriers *Microsized and Nanosized Carriers for Nonsteroidal Anti-Inflammatory Drugs* (pp. 95-132). Boston: Academic Press.
- Mukhtar, H., Das, M., Khan, W. A., Wang, Z. Y., Bik, D. P., & Bickers, D. R. (1988). Exceptional activity of tannic acid among naturally occurring plant phenols in protecting against 7,12-dimethylbenz(a)anthracene-, benzo(a)pyrene-, 3-methylcholanthrene-, and N-methyl-N-nitrosourea-induced skin tumorigenesis in mice. *Cancer Research*, 48(9), 2361.
- Myerson, A. S. (1999). Crystallization Basics. In A. S. Myerson (Ed.), *Molecular Modeling Applications in Crystallization* (pp. 55-105). Cambridge: Cambridge University Press.
- Orłowski, P., Tomaszewska, E., Gniadek, M., Baska, P., Nowakowska, J., Sokolowska, J., . . . Krzyzowska, M. (2014). Tannic Acid Modified Silver Nanoparticles Show Antiviral Activity in Herpes Simplex Virus Type 2 Infection. *PLoS ONE*, 9(8), e104113. doi: 10.1371/journal.pone.0104113

- Park, J., Brust, T. F., Lee, H. J., Lee, S. C., Watts, V. J., & Yeo, Y. (2014). Polydopamine-Based Simple and Versatile Surface Modification of Polymeric Nano Drug Carriers. *ACS Nano*, 8(4), 3347-3356. doi: 10.1021/nn405809c
- Pubchem. National Center for Biotechnology Information. CID=5479494. Retrieved Nov. 29, 2018 <https://pubchem.ncbi.nlm.nih.gov/compound/5479494>
- Sahiner, N., Sagbas, S., & Aktas, N. (2015). Single step natural poly(tannic acid) particle preparation as multitasking biomaterial. *Materials Science and Engineering: C*, 49(Supplement C), 824-834. doi: <https://doi.org/10.1016/j.msec.2015.01.076>
- Scalbert, A. (1991). Antimicrobial properties of tannins. *Phytochemistry*, 30(12), 3875-3883. doi: [https://doi.org/10.1016/0031-9422\(91\)83426-L](https://doi.org/10.1016/0031-9422(91)83426-L)
- Schneider, T., Zhao, H., Jackson, J. K., Chapman, G. H., Dykes, J., & Häfeli, U. O. (2008). Use of hydrodynamic flow focusing for the generation of biodegradable camptothecin-loaded polymer microspheres. *Journal of Pharmaceutical Sciences*, 97(11), 4943-4954. doi: <https://doi.org/10.1002/jps.21344>
- Shen, G., Xing, R., Zhang, N., Chen, C., Ma, G., & Yan, X. (2016). Interfacial Cohesion and Assembly of Bioadhesive Molecules for Design of Long-Term Stable Hydrophobic Nanodrugs toward Effective Anticancer Therapy. *ACS Nano*, 10(6), 5720-5729. doi: 10.1021/acsnano.5b07276
- Shin, M., Kim, K., Shim, W., Yang, J. W., & Lee, H. (2016). Tannic Acid as a Degradable Mucoadhesive Compound. *ACS Biomaterials Science & Engineering*, 2(4), 687-696. doi: 10.1021/acsbmaterials.6b00051
- Shin, M., Ryu, J. H., Park, J. P., Kim, K., Yang, J. W., & Lee, H. (2015). DNA/Tannic Acid Hybrid Gel Exhibiting Biodegradability, Extensibility, Tissue Adhesiveness, and Hemostatic Ability. *Advanced Functional Materials*, 25(8), 1270-1278. doi: 10.1002/adfm.201403992
- Sileika, T. S., Barrett, D. G., Zhang, R., Lau, K. H. A., & Messersmith, P. B. (2013). Colorless Multifunctional Coatings Inspired by Polyphenols Found in Tea, Chocolate, and Wine. *Angewandte Chemie International Edition*, 52(41), 10766-10770. doi: 10.1002/anie.201304922
- Sun, B., & Yeo, Y. (2012). Nanocrystals for the parenteral delivery of poorly water-soluble drugs. *Current Opinion in Solid State and Materials Science*, 16(6), 295-301. doi: <http://dx.doi.org/10.1016/j.cossms.2012.10.004>
- Tang, C., Amin, D., Messersmith, P. B., Anthony, J. E., & Prud'homme, R. K. (2015). Polymer Directed Self-Assembly of pH-Responsive Antioxidant Nanoparticles. *Langmuir*, 31(12), 3612-3620. doi: 10.1021/acs.langmuir.5b00213
- Vauthier, C., & Ponchel, G. (2017). Polymer Nanoparticles for Nanomedicines. A Guide for their Design, Preparation and Development. *Anticancer Res*, 37(3), 1544.
- von Martius, S., Hammer, K. A., & Locher, C. (2012). Chemical characteristics and antimicrobial effects of some Eucalyptus kinos. *Journal of Ethnopharmacology*, 144(2), 293-299. doi: <https://doi.org/10.1016/j.jep.2012.09.011>
- Yang, E. B., Wei, L., Zhang, K., Chen, Y. Z., & Chen, W. N. (2006). Tannic Acid, a Potent Inhibitor of Epidermal Growth Factor Receptor Tyrosine Kinase. *The Journal of Biochemistry*, 139(3), 495-502. doi: 10.1093/jb/mvj050
- Zhan, H., Jagtiani, T., & Liang, J. F. (2017). A new targeted delivery approach by functionalizing drug nanocrystals through polydopamine coating. *European Journal of Pharmaceutics and Biopharmaceutics*, 114, 221-229. doi: 10.1016/j.ejpb.2017.01.020

Zhan, H., Zhou, X., Cao, Y., Jagtiani, T., Chang, T.-L., & Liang, J. F. (2017). Anti-cancer activity of camptothecin nanocrystals decorated by silver nanoparticles. [10.1039/C7TB00134G]. *Journal of Materials Chemistry B*, 5(14), 2692-2701. doi: 10.1039/c7tb00134g

CHAPTER 3. SURFACE FUNCTIONALIZATION OF NANOCORE FORMULATIONS

A version of this chapter will be submitted for review.

3.1 Introduction

The surface of NP is decorated with molecules and ligands to provide NP with added functionality. Surface functionalization can improve the NP-target cell interaction, avoid the NP recognition by the immune system and control the payload release. NP surface modification requires chemically reactive sites on the NP surface, and usually includes coupling agents that need to be removed in exhaustive purification steps. Due to the natural affinity for solid surface, polyphenols was employed to coat nanoparticles providing reactive platforms for simple functionalization with ligands (Abouelmagd, Meng, Kim, Hyun, & Yeo, 2016; Park et al., 2014). Tannic acid (TA), which deposits efficiently on surfaces via oxidation-induced oligomerization (Sileika, Barrett, Zhang, Lau, & Messersmith, 2013) possesses catechol and galloyl groups that can interact with different molecules by hydrogen bonding and hydrophobic interactions. In a study done with PLGA NP, surface coating with TA enabled functionalizing the surface with a small molecule, fluoresceinamine; a synthetic polymer, folate-conjugated PEG; a polysaccharide, chitosan; and a protein, albumin (Abouelmagd et al., 2016). It was shown that the surface bound ligands maintained their functionality. In addition, compounds with planar polycyclic aromatic structures (doxorubicin, proflavine and rhodamine B) showed high binding affinity for the TA coat (Abouelmagd et al., 2016). Therefore, drugs with similar heteroaromatic structures can be easily loaded to NP surface via the TA platform. The polyphenolic structure of TA enabled efficient hydrogen bonding with the phosphate groups in the DNA backbone; therefore, the TA layer is used as a molecular glue to bind to DNA (Shin et al., 2015). The hydrolysis of ester bonds in TA structure allowed the release of DNA.

In this chapter, the TA/Fe³⁺ assemblies on the surface of nanocores were used to functionalize the surface with albumin, quinic acid derivative and plasmid DNA. The ability of TA to interact with molecules via hydrogen bonding, hydrophobic interaction, and electrostatic

interactions is expected to help functionalize the surface of nanocores with ligands. The functionality of the ligands after surface modification is evaluated.

3.2 Materials and Methods

3.2.1 Materials

Firefly luciferase-expressing plasmid DNA and enhanced green fluorescent protein (EGFP)-expressing plasmid DNA were replicated in DH5- α competent *Escherichia coli* (Feng et al., 2014). Quinic acid derivative (QA-NH₂) was synthesized as previously reported (Xu et al., 2018). Branched polyethyleneimine (BPEI, MW: 25 kDa) and 2-hydroxypropyl- β -cyclodextrin and human serum albumin ($\geq 96\%$ agarose gel electrophoresis) were purchased from Sigma-Aldrich (St. Louis, MO, USA). Lipofectamine™2000 was purchased from Invitrogen (Carlsbad, CA, USA). Methoxy Polyethylene Glycol Amine (mPEG-NH₂, MW: 2000 Da) was purchased from Nanocs (NY, USA). Mouse recombinant E-selectin was purchased from Biolegend (CA, USA). PEG dimethylacrylate (PEGDA, MW: 3400 Da) was purchased from Alfa Aesar (MA, USA). Coomassie Brilliant blue G-250 protein stain and sodium dodecyl sulfate-acrylamide gel electrophoresis (SDS-PAGE) reagents were purchased from Bio-Rad (CA, USA). (3-(4,5-Dimethylthiazol-2-yl)- 2,5- diphenyltetrazolium bromide) (MTT) was purchased from Invitrogen (Eugene, OR, USA).

3.2.2 Surface decoration of nanocore with plasmid DNA

PTX-pTA was prepared as described in chapter 2, then incubated with 0.2 μ g plasmid DNA (pDNA) at RT for 30 min at various PTX-pTA/pDNA ratio (volumes were made equal with water). Loading dye was added to a final concentration of 1x to the prepared mixtures and the whole volume (18 μ L) was loaded into wells of 1% agarose gel (containing 0.2 μ g/mL ethidium bromide, EtBr). Gel electrophoresis was run in 0.5x TAE buffer at 120 V for 30 min then the gel image was captured under UV light (wavelength 302 nm) using Azure C300 (Dublin, CA, USA). BPEI bound to 0.2 μ g pDNA at 20 times weight ratio was ran with the samples as a positive control. Blank pTA, equivalent to the highest PTX-pTA amount used, was ran to exclude the NP interference with the image.

3.2.2.1 Stability of pDNA binding to PTX-pTA

pDNA-bound PTX-pTA (PTX-pTA-pDNA) was prepared by incubating PTX-pTA with 0.2 μg pDNA at RT for 30 min at PTX-pTA/DNA weight ratio of 160. The mixture was then challenged with DNase, heparin, 50% FBS, 10 mM PB (pH 7.4), 5 M urea or saline. For DNase and heparin: DNase/reaction buffer mixture (equivalent to 1.5 DNase units) was added to PTX-pTA-pDNA and incubated for 15 min followed by addition of stop solution. Heparin solution in PBS was added to a final concentration of 4 mg/mL, and mixture incubated for 2 hours. Alternatively, the PTX-pTA-pDNA mixture was challenged with heparin only. For 50% FBS, 10 mM PB (pH 7.4), 5 M urea or saline: 100% FBS, 20 mM PB, 10 M urea, or 1.8% sodium chloride (NaCl) solution were added to the NP suspension in equal volume, respectively, and incubated for 2 hours. The treated samples, each equivalent to 0.2 μg pDNA, were loaded into wells of 1% agarose gel for electrophoresis. As a negative control to the sample treated with FBS, 50% FBS was loaded into one well and ran with the samples.

3.2.2.2 Cell uptake/interaction of PTX-pTA-pDNA

Nile red doped PTX-pTA (PTX*-pTA) were prepared by dissolving Nile red in the PTX/TA mixture used for preparing the nanocores at a concentration of 0.37 % w/w. The amount of Nile red incorporated was measured based on the fluorescence intensity ($\lambda_{\text{ex}}/\lambda_{\text{em}}$: 550nm/640 nm) of Nile red after dissolving the nanocores in acetonitrile. NCI/ADR-RES cells were seeded in 24 well plate at a density of 50,000 cells per well. After 24 hours, the medium was replaced with 500 μL of fresh serum-containing medium containing either PTX*-pTA, PTX*-pTA-pDNA (samples were brought to equal fluorescence with unlabeled corresponding particles, and particles concentration was 22 $\mu\text{g}/\text{mL}$), or free Nile red (at equivalent fluorescence to the particles). After 4 h incubation with the treatments, cells were washed with PBS twice and then collected in 300 μL PBS for analysis using flow cytometer (Accuri C6, BD Biosciences, San Jose, CA).

Cell interaction of PTX*-pTA and PTX*-pTA-pDNA was also observed with confocal microscopy. NCI/ADR-RES cells were seeded in 35 mm glass bottom dish with 14 mm micro-well, at a density of 300,000 cells per dish. After 24 hours, the medium was replaced with 1 mL of fresh serum-containing medium containing PTX*-pTA, PTX*-pTA-pDNA, which were brought to equal fluorescence with unlabeled corresponding particles making particles concentration 22 $\mu\text{g}/\text{mL}$, or free Nile red (at equivalent fluorescence to the particles). After 4 h

incubation with the treatments, cells were washed with PBS twice then fixed by adding 4% paraformaldehyde for 10 min. Cells were incubated with Hoechst dye (5 $\mu\text{g}/\text{mL}$) for 5 min for nuclear staining. After washing, cells were imaged using a Nikon-A1R confocal microscope (Nikon America Inc., NY, USA). Cell nuclei were detected with $\lambda_{\text{ex}}/\lambda_{\text{em}}$ of 407 nm/425-475 nm, and fluorescent nanocores were detected with $\lambda_{\text{ex}}/\lambda_{\text{em}}$ of 560 nm/595 nm.

3.2.2.3 Cytotoxicity of PTX-pTA in NCI/ADR-RES cells

NCI/ADR-RES cells were seeded in a 96 well plate at a density of 10,000 cells per well. After 24 h incubation, the cell culture medium was replaced with fresh medium containing PTX-pTA at various PTX-equivalent concentrations. After 4 h of incubation, cell viability was evaluated by the MTT assay. Culture medium was replaced with 100 μL of fresh medium and 15 μL of MTT solution (5 mg/mL), and cells were incubated for 4 h. The formazan crystals were dissolved by addition of 100 μL of stop/solubilizing solution (50 % DMF, 20% SDS and 0.02% acetic acid) and the absorbance was read at the wavelength of 562 nm using a SpectraMax M3 microplate reader (Molecular Device, Sunnyvale, CA). The cell viability percentage was calculated by normalizing the measured absorbance to that of control cells that did not receive treatments.

3.2.2.4 *In vitro* transfection of PTX-pTA-pDNA

NCI/ADR-RES ovarian cancer cells (ATCC, Manassas, VA, USA) were grown in RPMI medium supplemented with 10% FBS and 1% penicillin / streptomycin. Cells were seeded in 24 well plate at a density of 50,000 cells per well. After 24 hours, the medium was replaced with 500 μL of fresh serum-containing medium containing either PTX-pTA-pDNA or lipofectamine bound-pDNA (prepared by incubation with EGFP-expressing pDNA for 30 min at RT) equivalent to 0.2 μg pDNA per well. PTX-pTA and lipofectamine concentrations were 72 and 1.4 $\mu\text{g}/\text{mL}$, respectively. After 4 h incubation, treatments were washed, and fresh medium was added to the cells. Cells were imaged using Cytation-3 imaging system (Biotek, VT, USA), 24 and 48 h post-transfection. EGFP was detected with $\lambda_{\text{ex}}/\lambda_{\text{em}}$ of 488 nm/505-555 nm. Finally, cells were washed with PBS, and collected in 300 μL PBS for analysis of EGFP expression using flow cytometer (Accuri C6, BD Biosciences, San Jose, CA).

3.2.2.5 Stability of DNA binding to PTX-pTA in medium and acetate buffer

PTX-pTA-pDNA was prepared by incubating PTX-pTA with 0.2 μg pDNA at RT for 30 min at PTX-pTA/DNA weight ratio of 160. The mixture was then separately challenged by adding equal volume of serum-containing RPMI medium or 100 mM acetate buffer (pH 5) and incubating for 3 h. The treated samples, each equivalent to 0.2 μg pDNA, were loaded into wells of 1% agarose gel for electrophoresis. BPEI bound to 0.2 μg pDNA at 20 times weight ratio was run with the samples as a positive control.

3.2.3 Surface decoration of nanocore with quinic acid derivative

Quinic acid derivative (QA-NH₂) was synthesized according to the previously published method (Amoozgar, Park, Lin, Weidle, & Yeo, 2013). PTX-pTA nanocores were incubated with QA-NH₂ solution in water (2 mg/mL) at a weight ratio of 1:1, with rotation at RT for 1 h, followed by centrifugation for particles collection and wash. The collected supernatant was used for indirectly quantifying the amount of bound QA-NH₂. The particle size and zeta potential were measured in 10 mM PB (pH 7.4) via DLS (Malvern Zetasizer Nano-ZS90). For QA-NH₂ quantification, C18 reversed phase HPLC (25 cm \times 4.6 mm, particle size: 5 μm) was used. The mobile phase was acetonitrile/water (1:9) and QA-NH₂ was detected with UV detector at wavelength of 254 nm. Control particles, PTX-pTA-PEG, were prepared by incubating PTX-pTA with PEG-NH₂ (MWt=2000) solution in water and treated as above. Rhodamine B doped PTX-pTA (PTX*-pTA) were prepared by dissolving rhodamine B in the PTX/TA mixture used for preparing the nanocores at a concentration of 1.2 % w/w.

3.2.3.1 Binding of PTX-pTA-QA to immobilized E-selectin

Mouse recombinant E-selectin or human serum albumin (0.1 μg in 100 μL) were added to 96-well enzyme-linked immunosorbent assay (ELISA) plates and incubated at 4°C overnight. The wells were washed with PBS and incubated with 1% albumin for 2 h at RT (to block non-specific interactions). Albumin was removed and washed.

For direct measurement of NP binding to E-selectin (measuring fluorescence of bound NP), 100 μL of rhodamine-doped PTX-pTA-QA or PTX-pTA-PEG nanocores (100 $\mu\text{g}/\text{mL}$) were added in the wells for 1 h at RT. The wells were washed with PBS and then well contents were dissolved in water/acetonitrile mixture. Fluorescence was measured using plate reader ($\lambda_{\text{ex}}/\lambda_{\text{em}}$ of 550

nm/580 nm). Percentage of fluorescence remaining in the wells relative to the initial particles fluorescence was calculated.

For indirect measurement of NP binding to E-selectin (HL-60 binding inhibition assay): 200 μ L of PTX-pTA, PTX-pTA-QA or PTX-pTA-PEG nanocores (500 μ g/mL) were added in the wells for 2.5 h at 37 °C. The treatments were washed with PBS and replaced with HL-60 cells in RPMI medium (50,000 cells per well). After 2 h incubation, the unbound HL-60 cells were removed by washing with PBS. Remaining bound cells were suspended in 300 μ L PBS and counted using flow cytometry.

3.2.4 Surface decoration with human serum albumin

CFZ-pTA nanocores were incubated in human serum albumin (HSA) solution in water at 1:2 weight ratio with mild rotation at RT for 4 h. The particles were centrifuged (at 43,400 rcf for 20 min at 4°C) to remove unadsorbed albumin, this step was repeated twice. The pellet was suspended in water and stored at 4 °C for further characterization. The albumin coated particles were called CFZ-pTA-alb.

3.2.4.1 Physico-chemical characterization of CFZ-pTA-alb

Particle size and zeta potential were measured in 10 mM PB (pH 7.4) via DLS (Malvern Zetasizer Nano-ZS90) and particles morphology was examined using TEM. CFZ content was determined using HPLC as described in chapter 2. Albumin content was determined using SDS-PAGE. CFZ-pTA-alb with a premeasured mass or standard albumin solutions were mixed with 4X sample buffer (a mixture of laemmli and β -mercaptoethanol) at a volume ratio of 3:1 and heated at 95 °C for 5 min. The samples were loaded on a 12% polyacrylamide gel and resolved with electrophoresis at 120 V for 30 min. The gel was stained with QC Colloidal Coomassie Stain and imaged with Azure C300 (Dublin, CA, USA). The densitometry function of the AzureSpot Analysis Software was used to quantify the albumin band intensity. The albumin content was determined by comparing the band intensities of CFZ-pTA-alb samples and standard albumin solutions. For colloidal stability testing, CFZ-pTA-alb (at concentration equivalent to 60 μ g/mL CFZ) was incubated in 50% FBS in PBS at 37 °C for 24 h with periodical measurement of particle size using Zetasizer.

3.2.4.2 *In vitro* release study

CFZ-pTA or CFZ-pTA-alb equivalent to 10 µg of CFZ were suspended in 0.25 mL of 10% PEG dimethylacrylate (PEGDA, 3400 Da) solution in PBS. The suspensions were illuminated under UV (365 nm) for 10 min in the presence of 25 µL of irgacure solution (20% w/v in methanol) to crosslink PEGDA. The crosslinked PEGDA matrix was briefly rinsed with water to remove free particles and 1 mL of RPMI-1640 medium supplemented with 10% FBS was added as a release medium. The matrices were then incubated at 37 °C on an orbital shaker and at predetermined time points the whole release medium was sampled for HPLC analysis and replaced with 1 mL of fresh medium for further incubation.

3.2.4.3 *In vitro* cytotoxicity study

B16F10 mouse melanoma cells (ATCC, USA) or HCC-1937 (triple negative breast cancer) (ATCC, USA) were grown in RPMI or DMEM medium, respectively, containing 10% FBS and penicillin (100 IU/mL) and streptomycin (100 µg/mL). Cells were seeded in a 96 well plate at a density of 4,000 cells per well. After 24 h incubation, the cell culture medium was replaced with fresh medium containing CFZ (solution in dimethyl sulfoxide (DMSO)), CFZ-pTA or CFZ-pTA-alb with the final drug concentration ranging from 10 to 800 nM. For continuous treatment, the cells were incubated with the treatment for 72 h. For pulse treatment, cells were incubated with the treatment for 2 h then washed and incubated with drug-free medium for additional 70 h. Cell viability was evaluated by the MTT assay. Culture medium was replaced with 100 µL of fresh medium and 15 µL of MTT solution (5 mg/mL), and cells were incubated for 4 h. The formazan crystals were dissolved by addition of 100 µL of stop/solubilizing solution (50 % DMF, 20% SDS and 0.02% acetic acid) and the absorbance was read at wavelength of 562 nm using a SpectraMax M3 microplate reader (Molecular Device, Sunnyvale, CA). The cell viability percentage was calculated by normalizing the measured absorbance to that of control cells that did not receive treatments.

3.2.4.4 *In vitro* metabolic stability

Metabolic stability of different CFZ formulations (CFZ-CD, CFZ dissolved in 10 mM citrate buffer (pH 3.1) containing 20% (w/v) 2-hydroxypropyl-β-cyclodextrin), CFZ-pTA and CFZ-pTA-alb) was tested. Whole blood and liver were collected from a C57BL/6 male mice. The

liver was washed with cold PBS (pH 7.4), and then homogenized in cold PBS (at 1:5 ratio of liver weight (g) to PBS volume (mL)). Aliquots of liver homogenate (20 mg) were pre-incubated at 37 °C for 1 min before the addition of CFZ formulations at a final CFZ concentration of 93 µM (n=3 per group). The treatments were incubated at 37 °C for 60 min. For CFZ extraction from the liver tissue, 1 mL of triton-x (0.5% in water) was added to each sample and vortexed for 2 min followed by addition of 3 mL of tert-Butyl methyl ether (TBME) containing 2.5 µg of paclitaxel as an internal standard and mixed on a rotating shaker for 40 min. The mixture was then centrifuged at 4,500 rcf for 15 minutes and the organic layer was separated and transferred to a glass vial to be dried under vacuum. The dried samples were reconstituted in 100 µL of DMSO filtered through 0.45 µm syringe filter and analyzed with HPLC. An individual standard curve was prepared by spiking CFZ in liver homogenates to yield the final concentrations of 100, 50, 25, 12.5, 6.25, 3.125 and 1.56 µg/mL and processed in the same way as the samples. The whole blood was collected into heparinized tube and kept on ice until the assay was performed. CFZ formulations were added to blood aliquots at a final concentration of 67 µM (n=3 per group). The aliquots (100 µL) were incubated at 37 °C for 30 min, then 200 µL triton-x was added and vortexed for 10 min followed by addition of 600 µL of acetonitrile to precipitate proteins. The mixture was bath sonicated for 10 min then centrifuged at 4500 rcf for 30 min, and the supernatant was filtered over 0.45 µm membrane filter. Standard CFZ concentrations were treated similarly. Standards and samples were analyzed using HPLC.

3.3 Results

3.3.1 Surface decoration of nanocore with plasmid DNA

PTX-pTA was incubated with pDNA at different weight ratios to determine the minimum PTX-pTA/pDNA ratio required for binding. At a weight ratio of 109 and lower, pDNA bound to some extent to PTX-pTA but not completely as shown by the dragging bands in Figure 12c-f. At a weight ratio of 160, pDNA bound efficiently to the nanocore surface, as indicated by no band appearance in the gel (Figure 12i). The weight ratio of 160 was therefore considered as the optimal PTX-pTA/pDNA binding ratio and used in next experiments. PTX-pTA with pDNA bound to the surface was called PTX-pTA-pDNA and had a size of 184 nm and surface charge of -31 mV as

measured by DLS in 10 mM PB (pH 7.4), which is similar to the size and charge of bare PTX-pTA.

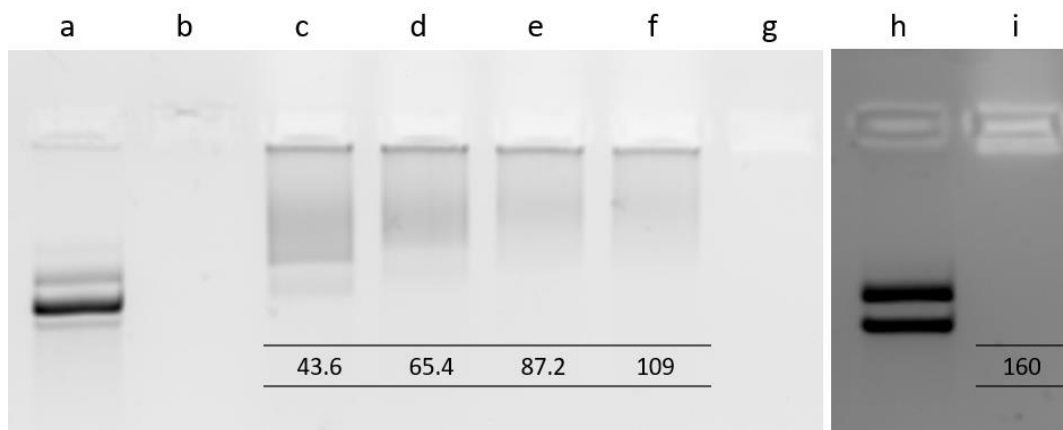


Figure 12: pDNA binding to PTX-pTA surface: (a and h) free pDNA (negative control), (b) BPEI-bound pDNA (positive control), (c-f and i) PTX-pTA mixture with pDNA at different PTX-pTA/pDNA weight ratio as indicated on the gel image below the lanes, and (g) blank pTA without pDNA. (h and i were ran in a separate gel)

3.3.1.1 Stability of pDNA binding to PTX-pTA

PTX-pTA-pDNA was challenged with different treatments to assess the stability and nature of pDNA binding. As shown in Figure 13c, PTX-pTA-pDNA was resistant to heparin, indicating that negatively charged molecules do not destabilize the pDNA/pTA complex. The PTX-pTA-pDNA was also stable in PB and saline (Figure 13f and h, respectively), consistent with the fact that the interaction between pDNA and PTX-pTA did not rely on ionic interactions. After challenging PTX-pTA-pDNA with DNase, it was incubated with heparin for 2 h to release digested DNA fragment that were still bound to the nanocore surface. However, PTX-pTA-pDNA showed high stability to this treatment suggesting that although the pDNA was bound to the surface, its interaction with pTA attenuated the access of DNase. In 50% FBS, PTX-pTA-pDNA displayed a smeared band (Figure 13e) which was attributed to the FBS components as shown by the negative control (Figure 13i). Therefore, the stability of PTX-pTA-pDNA in the presence of serum components was confirmed. Most importantly, in the presence of 5M urea, PTX-pTA-pDNA showed a smeared band (Figure 13g) due to the release of bound pDNA, suggesting that the nature of pDNA-pTA binding is, at least in part, hydrogen bonding.

It is noteworthy that although the pDNA solution used for running this experiment showed some degradation (Smear band in Figure 13a), PTX-pTA could still efficiently bind it indicating that it is capable of binding nucleic acids of shorter strands than pDNA as well.

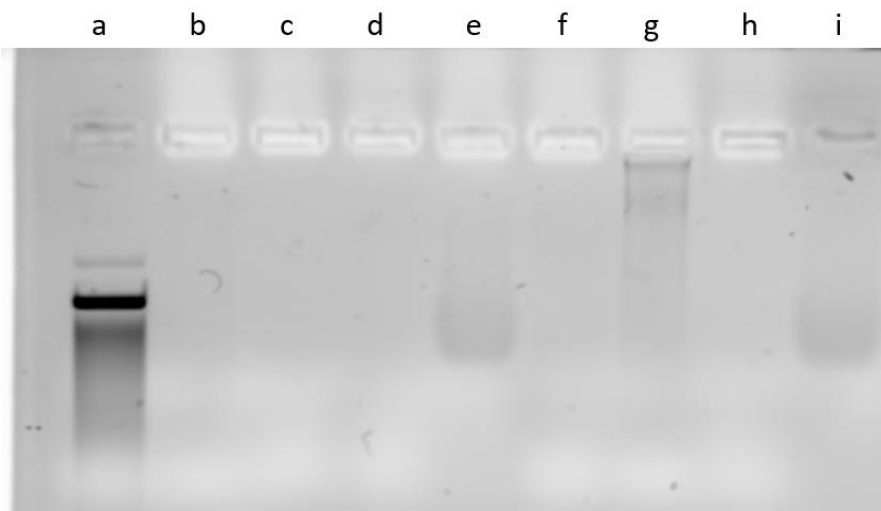


Figure 13: Stability of pDNA binding to PTX-pTA upon challenging: (a) free pDNA (negative control), (b) PTX-pTA-pDNA (unchallenged), (c-h) PTX-pTA-pDNA challenged with heparin (c), DNase and heparin (d), 50% FBS (e), 10 mM PB (f), 5 M urea (g) or saline (h), and (i) 50% FBS (without pDNA) run as a control.

3.3.1.2 Cell uptake/interaction of PTX-pTA-pDNA

For PTX-pTA-pDNA to efficiently deliver its pDNA payload it should first enter the cells. NCI/ADR-RES ovarian cancer cells were used to study the cell uptake of PTX-pTA-pDNA. This is a multi-drug resistant cell line owing to overexpression of P-glycoprotein (NIH); therefore, PTX cytotoxicity would be avoided and would not interfere with the results.

To evaluate the cell uptake of PTX-pTA-pDNA, fluorescently labeled particles (PTX*-pTA) were prepared by doping a small quantity of Nile red into the organic phase. Owing to the hydrophobicity of Nile red, it is expected to reside in the core with PTX. In a previous study (Shen et al., 2016), Nile red doping was used similarly to track the cell uptake of hydrophobic drugs in TA-coated cores. The pDNA binding was confirmed by gel retardation assay, with pDNA remaining in the well after binding to PTX*-pTA similar to the non-labeled PTX-pTA (Figure 14a). PTX*-pTA or PTX*-pTA-pDNA (at a concentration of 22 $\mu\text{g}/\text{mL}$) were incubated with NCI/ADR-RES cells for 4 h. Free Nile red was also tested in parallel to ensure that the incorporated Nile red represents the nanocores. Confocal microscope images showed high fluorescence signals

associated with the cells after incubation with PTX*-pTA or PTX*-pTA-pDNA (Figure 14b). In contrast, cells incubated with equivalent free nile red also showed diffuse signals, which was less intense than those with nanocores. This confirms that the fluorescence signals of PTX*-pTA and PTX*-pTA-pDNA represent the particles but not free nile red leached-out. This result was quantified by flow cytometry analysis (Figure 14c).

To confirm that the cell interaction of nanocore particles with NCI/ADR-RES was not driven by cytotoxicity, cell viability under similar treatment was evaluated. The cell mitochondrial activity was determined using the MTT assay and showed that cells maintained their viability at all tested concentrations (Figure 15). NCI/ADR-RES cells were exposed for 4 h to PTX-pTA particles at different PTX-equivalent concentrations. The cells tolerated PTX-pTA equivalent to PTX 56.68 μ M with no sign of toxicity.

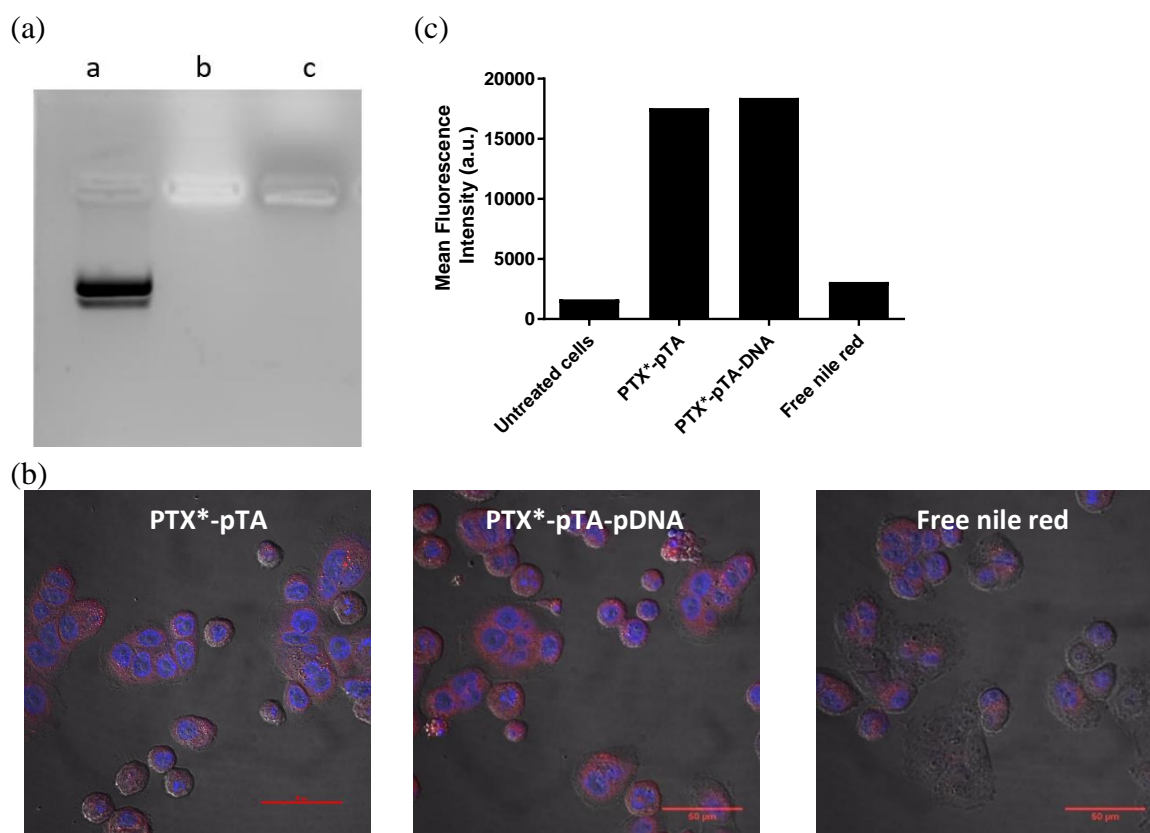


Figure 14: Cell interaction of PTX-pTA-pDNA with NCI/ADR-RES: (a) efficient pDNA binding to nile red labeled PTX*-pTA was confirmed by gel retardation assay (a: free pDNA, b: PTX-pTA, and c: PTX*-pTA, all wells were loaded with 0.2 μ g of pDNA), cell interaction was (b) visualized by confocal microscopy imaging of PTX*-pTA, PTX*-pTA-pDNA and free nile red (negative control), 4 h after incubation with NCI/ADR-RES cells. (Blue= nuclei stained with Hoechst dye and red= nanocores labeled with nile red) (Scale bar= 50 μ m), and (c) quantified by flow cytometry analysis.

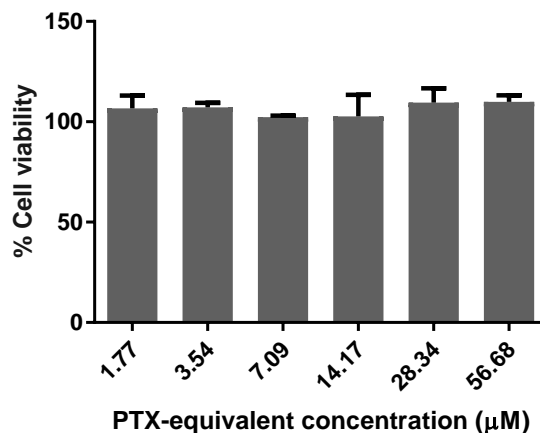


Figure 15: Viability of NCI/ADR-RES cells after incubation with PTX-pTA at different PTX-equivalent concentrations (μM) for 4 hours as determined with MTT assay.

3.3.1.3 *In vitro* transfection of PTX-pTA-pDNA

The *in vitro* transfection efficiency of PTX-pTA-pDNA in NCI/ADR-RES cells was tested. Lipofectamine is a cationic liposomal formulation considered as a benchmark transfection agent. EGFP-expressing pDNA was used such that successful cell transfection will result in EGFP expression that can be detected by fluorescence microscopy and flow cytometry. Cells were treated with either PTX-pTA-pDNA or lipofectamine-pDNA for 4 h, rinsed and incubated for another 24 and 48 h before imaging. PTX-pTA-pDNA did not transfect the cells with no detectable green fluorescence (Figure 16b), in contrast to Lipofectamine (Figure 16a). This was further confirmed by flow cytometry at the end of 48 h, where Lipofectamine complex showed significant EGFP expression but PTX-pTA-pDNA showed no difference from the untreated cells (Figure 17).

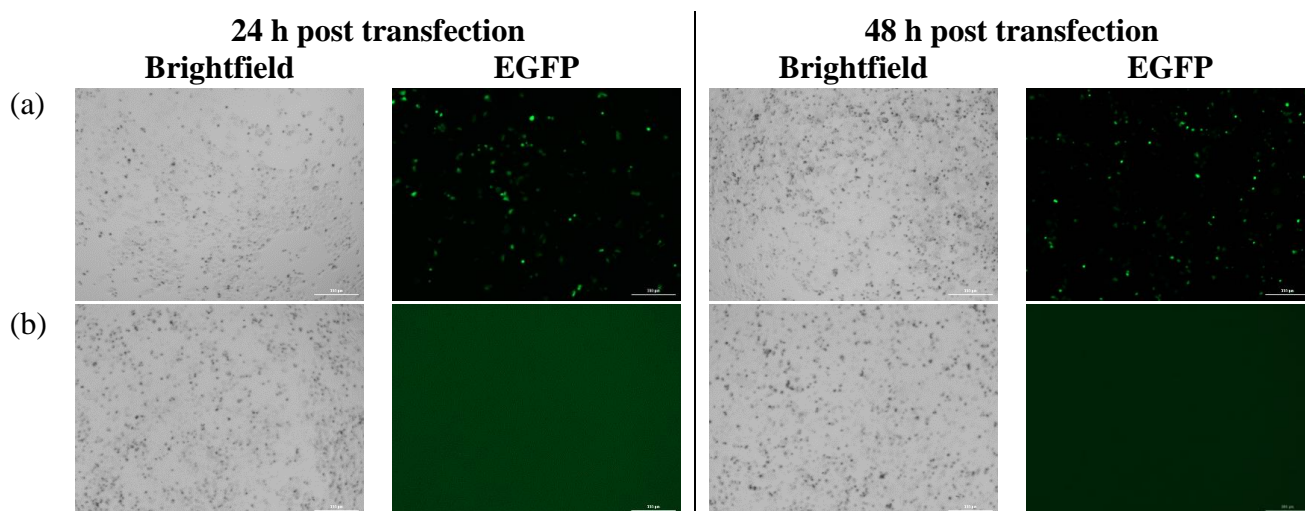


Figure 16: *In vitro* transfection of EGFP-expressing pDNA (green) bound to (a) lipofectamine (positive control) or (b) PTX-pTA nanocore, 24 and 48 h after treatment to NCI/ADR-RES cells (treatment was done for 4 h followed by wash and media replacement), imaged by Cytation-3 imaging system. (Scale bar = 300 μ m)

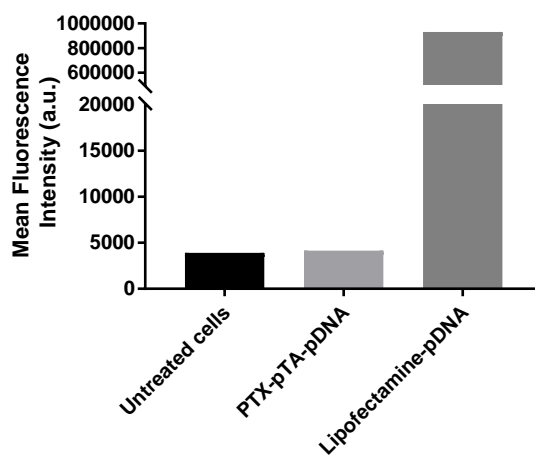


Figure 17: Quantitative analysis of EGFP expression 48 h after *in vitro* transfection of EGFP-expressing pDNA via lipofectamine (positive control) or PTX-pTA nanocore in NCI/ADR-RES cells (treatment was done for 4 h followed by wash and media replacement), analyzed by flow cytometry. Untreated cells were analyzed as a negative control.

3.3.1.4 Stability of pDNA binding to PTX-pTA in medium and acetate buffer

To understand why the transfection with PTX-pTA-pDNA was unsuccessful, the stability of pDNA binding was tested in RPMI medium supplemented with 10% FBS (similar to that used in the transfection experiment) and in acetate buffer of pH 5, by gel retardation assay. As shown

in Figure 18, pDNA stayed well bound to PTX-pTA nanocore in both FBS-supplemented medium and acetate buffer (lanes e and g, respectively). The stability in FBS-supplemented medium excludes the possibility of pDNA release prior to the cell uptake of the particles. The stability in pH 5 acetate buffer suggests that pDNA remained bound to PTX-pTA in acidic pH and could not escape the endosomal compartment and reach the nucleus for transfection.

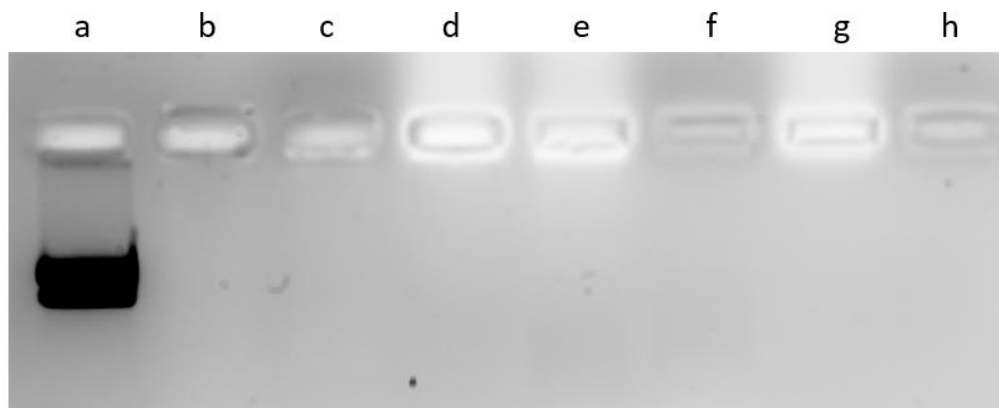


Figure 18: Stability of pDNA binding to PTX-pTA in serum-containing RPMI medium and in 100 mM acetate buffer (pH 5): (a) free pDNA (negative control), (b) BPEI-bound pDNA (positive control), (c) BPEI-bound pDNA challenged with complete medium, (d) PTX-pTA-pDNA, (e) PTX-pTA-pDNA challenged with complete medium, (f) complete medium (negative control), (g) PTX-pTA-pDNA challenged with acetate buffer and (h) acetate buffer (negative control).

3.3.2 Surface decoration of nanocore with quinic acid derivative

Quinic acid (QA) has a structural similarity with sialyl Lewis-x (sLe^x), a carbohydrate structure expressed on leukocytes surface (Munro et al., 1992). Therefore it has the ability to bind to E-selectin, overexpressed on the endothelium supplying various metastatic tumors (Brodt et al., 1997; Fox, Turner, Gatter, & Harris, 1995; Nguyen et al., 1997). We previously reported a quinic acid derivative (QA-NH₂) bound to NP surface to have increased NP interaction with selectin-expressing endothelial cells (Amoozgar et al., 2013; Xu et al., 2018) and NP delivery to tumors (Xu et al., 2018). We hypothesized that the QA-NH₂ can bind to the surface of nanocores by interacting with TA via hydrogen bonding and hydrophobic interactions. PTX-pTA nanocores were incubated with QA-NH₂, and the extent of QA-NH₂ binding was determined indirectly by quantifying the unbound molecules remaining in solution. QA-NH₂ constituted $9.1 \pm 1.4\%$ of the nanocore mass, which corresponded to 4.4 ± 0.7 QA-NH₂ molecule/nm². The particles were named PTX-pTA-QA and had z-average and zeta-potential of 168 ± 6 nm and -21 ± 3 mV, respectively,

as measured with DLS. The reduction in surface charge from bare PTX-pTA (-31 ± 3 nm) indicates partial shielding of TA hydroxyl groups with QA-NH₂.

3.3.2.1 Binding of PTX-pTA-QA to immobilized E-selectin

The functionality of QA bound to the surface of PTX-pTA nanocores was tested by the method described by Shamay *et al.* (Shamay *et al.*, 2016). PTX-pTA-PEG, PTX-pTA covered with PEG to shield sticky pTA surface, was used as a negative control. Rhodamine-labeled nanocores were incubated in a recombinant E-selectin-coated plate. Albumin-coated plate was used as a control plate. The binding of nanocores to E-selectin- or albumin-coated plates was estimated by incubating the particles in each well for 1 h, washing, and measuring the remaining fluorescence in the well. PTX-pTA-QA bound to the E-selectin-coated surface to a similar extent as PTX-pTA-PEG. Their binding to albumin-coated surface was similar, indicating that the binding to either surface was non-specific (Figure 19a).

Alternatively, the binding of PTX-pTA-QA to the E-selectin-coated surface was tested indirectly via the HL-60 binding inhibition assay. HL-60 is a promyelocytic cell line that expresses sLe^x and thus binds to the E-selectin-expressing endothelial cells. HL-60 binding to E-selectin would be reduced, if E-selectin was preoccupied by PTX-pTA-QA. The E-selectin coated wells were pretreated with nanocores (PTX-pTA, PTX-pTA-QA or PTX-pTA-PEG), and the number of HL-60 cells that could bind afterwards was counted using flow cytometry. Control wells were directly treated with HL-60 cells without prior NP treatment as a positive control. As shown by Figure 19b, both bare PTX-pTA and PTX-pTA-QA significantly reduced HL-60 binding from the control, but PTX-pTA-PEG did not. This result suggests that PEG coverage of the surface does not allow PTX-pTA-PEG to bind to E-selectin-expressing endothelial cells. The inhibition by PTX-pTA may be due to the non-specific affinity of pTA for solid surface. It is difficult to distinguish whether the inhibition by PTX-pTA-QA is due to its binding to selectin or insufficient surface coverage by QA.

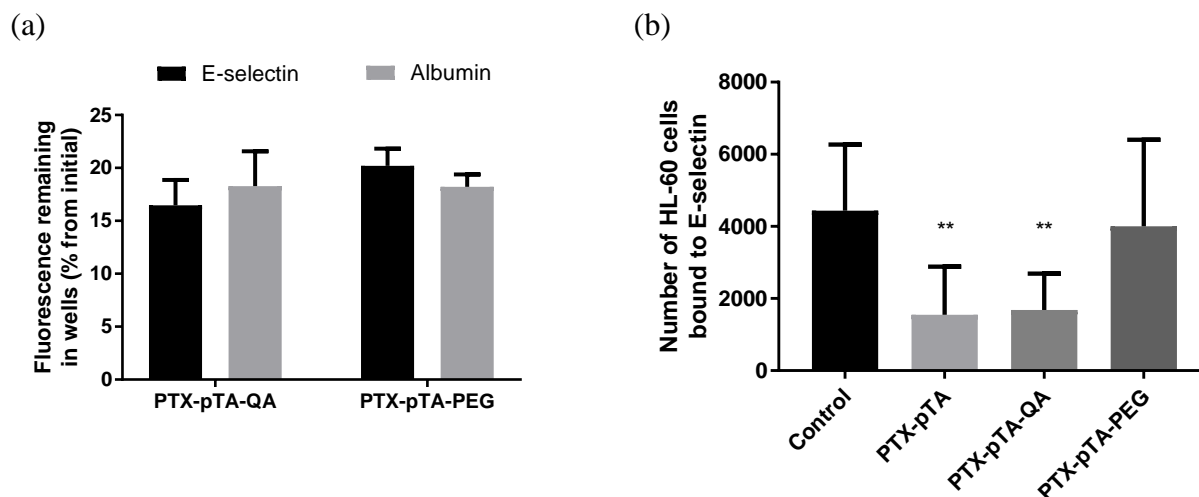


Figure 19: Binding assay of PTX-pTA-QA to mouse recombinant E-selectin immobilized on 96-well ELISA plate: (a) Direct assay, fluorescent (rhodamine-doped) nanocores (0.1 mg/mL) were incubated in the wells for 1 h followed by wash then remaining fluorescence was normalized to initial fluorescence (albumin-coated plate is control for non-specific binding), and (b) Indirect assay (HL-60 binding inhibition assay), nanocores (0.5 mg/mL) were incubated in the wells for 2.5 h, then washed and replaced with HL-60 cells for 2 h, after washing, number of bound HL-60 cells was counted using flow cytometry (PTX-pTA-PEG is negative control). ** indicates $p < 0.01$ vs. control wells (HL-60 treated without prior NP treatment) (one-way ANOVA followed by Tukey's test).

3.3.3 Surface decoration of nanocore with human serum albumin

CFZ-pTA incubated in HSA solution, washed with water and retrieved by centrifugation was called CFZ-pTA-alb. As shown by TEM images (Figure 20a), CFZ-pTA-alb size ranged from 50-100 nm. However, measured by DLS, it had a z-average of 179 ± 8 nm, consistent with DLS measurement of bare CFZ-pTA, and zeta potential of -20.6 ± 3.1 mV. The slight reduction in negative surface charge indicated the coverage of the pTA layer. The albumin layer constituted 15 ± 1 wt% and the CFZ core 41 ± 2 wt% in CFZ-pTA-alb, as measured by SDS-PAGE (Figure 20b) and HPLC, respectively. CFZ-pTA-alb showed colloidal stability in FBS (Figure 20c), similar to CFZ-pTA.

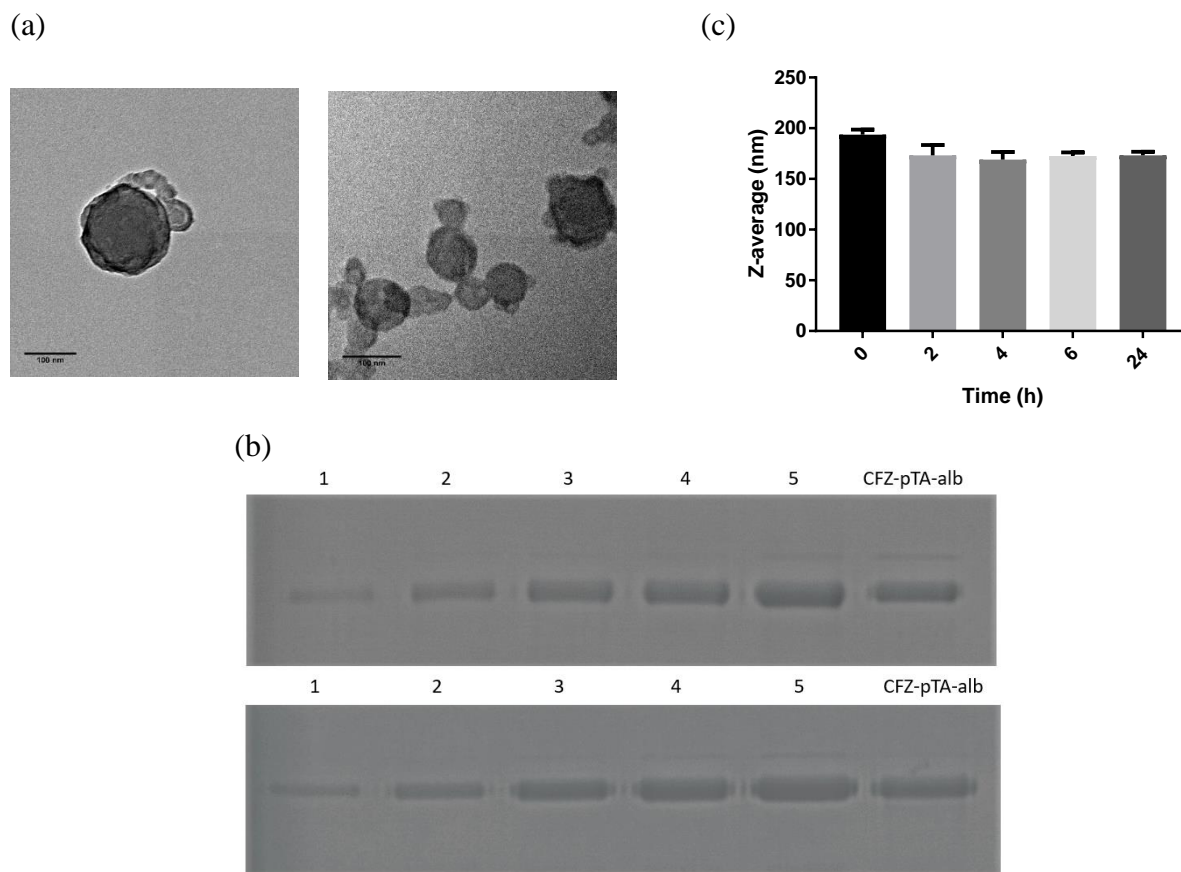


Figure 20: (a) TEM images of CFZ-pTA-alb (scale bar= 100 nm), (b) SDS-PAGE was replicated two times to confirm albumin content, lanes 1, 2, 3, 4 and 5 are albumin standards of 10, 25, 50, 75 and 100 $\mu\text{g/mL}$, and (c) size stability of CFZ-pTA-alb after incubation in 50% FBS solution.

3.3.3.1 *In vitro* drug release kinetics

To study the role of albumin in controlling CFZ release, an *in vitro* release experiment was done by housing CFZ-pTA or CFZ-pTA-alb in a PEGDA hydrogel and incubating in RPMI medium supplemented with 10% FBS. In 24 h, 5% and 10% of CFZ was released from CFZ-pTA-alb and CFZ-pTA, respectively (Figure 21a). These may be an underestimation of actual drug release with the hydrogel serving as a barrier to drug diffusion, but it allows for comparing the two formulations.

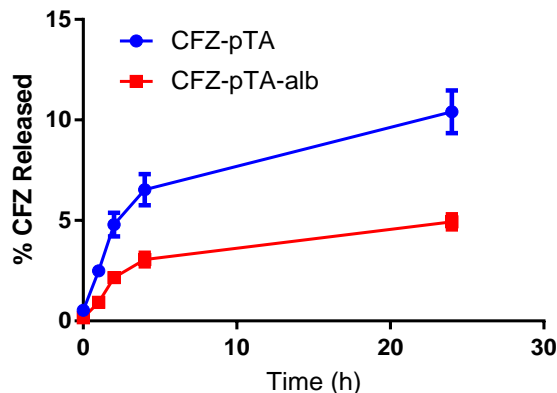


Figure 21: *In vitro* release kinetics of CFZ-pTA and CFZ-pTA-alb in 10% FBS/RPMI medium.

3.3.3.2 Cytotoxicity

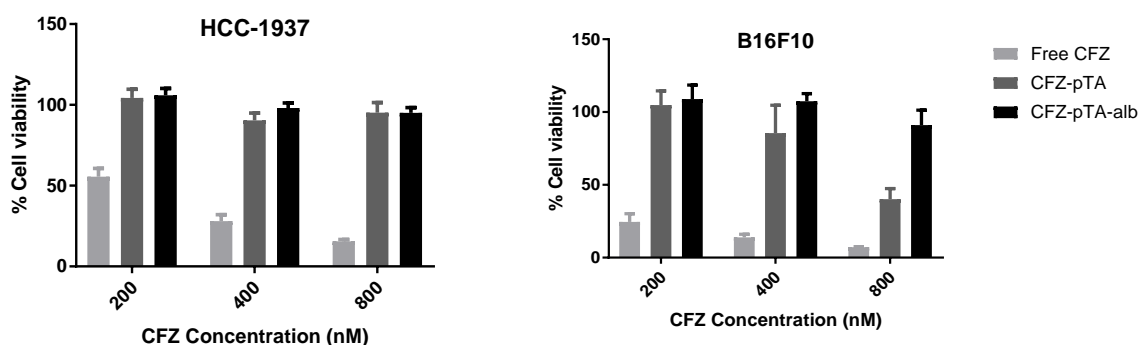
The cytotoxicity of nanocore formulations compared to free CFZ solution in cancer cell lines was evaluated as an indirect indicator of drug release stability. Free CFZ (solution in DMSO), CFZ-pTA, and CFZ-pTA-alb were incubated with HCC-1937 (triple negative breast cancer) and B16F10 (melanoma) in varying concentrations. With 2 h exposure to the cells, nanocores were less toxic than free drug due to the attenuation of CFZ release (Figure 22a). After 72 h exposure, nanocores manifested CFZ activity indicating the sustained CFZ release (Figure 22b). This trend was more obvious with CFZ-pTA-alb than CFZ-pTA due to the greater attenuation of CFZ release. To exclude carrier toxicity, the cells were treated with pTA or pTA-alb at concentrations equivalent to their respective percentages in CFZ nanocores. After 72 h exposure to the highest possible carrier concentration used, viability of B16F10 cells only slightly decreased to 84 and 76% with pTA and pTA-alb treatments, respectively (Figure 22c). This indicates that cytotoxicity of the nanocores is mainly due to the encapsulated CFZ, with the carrier only having minimal cytotoxicity.

3.3.3.3 *In vitro* metabolic stability

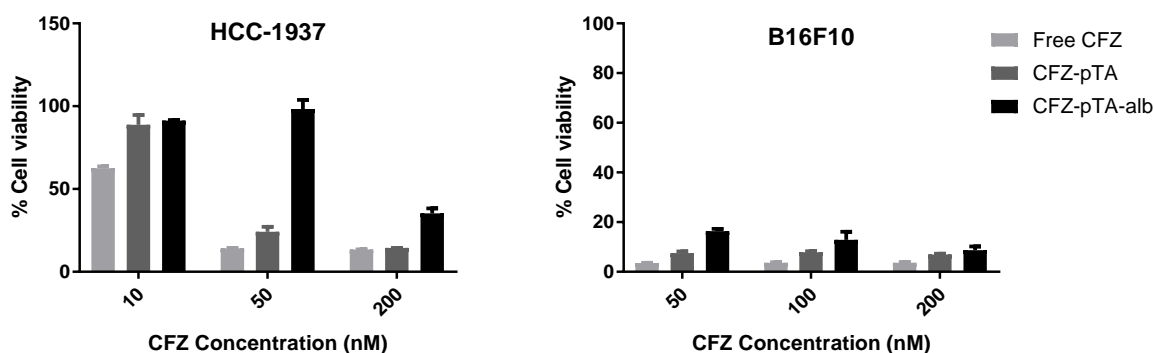
The ability of nanocores to protect CFZ against metabolic degradation was tested *in vitro* using whole blood and mouse liver homogenate. After 60 min incubation in liver homogenates, CFZ encapsulated in CFZ-pTA degraded by microsomal metabolizing enzymes to 7% remaining CFZ, whereas the free solubilized CFZ-CD formulation degraded to 1% remaining CFZ (Figure 23a). CFZ-pTA-alb displayed significantly higher stability with 14% of CFZ remaining after 60

min due to the additional protection by albumin (Figure 23b). In whole blood for 30 min, similar trend was observed (Figure 23b).

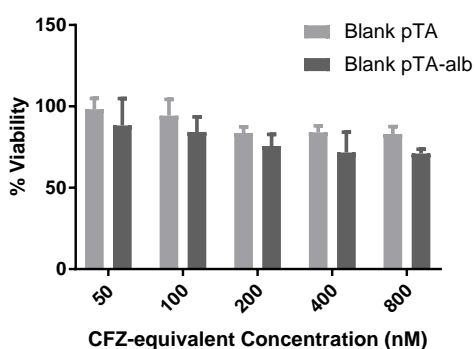
(a) 2 h of direct exposure



(b) 72 h of direct exposure



(c)



CFZ (nM)	pTA ($\mu\text{g/mL}$)	pTA-alb ($\mu\text{g/mL}$)
50	0.036	0.054
100	0.072	0.108
200	0.144	0.216
400	0.288	0.432
800	0.576	0.864

Figure 22: Controlled cytotoxicity as indirect indicator of release stability: (a) Cytotoxicity to HCC-1937 and B16F10 cells after 2 h of direct exposure to free CFZ, CFZ-pTA or CFZ-pTA-alb at equivalent CFZ concentrations, followed by incubation in drug-free medium, (b) cytotoxicity to HCC-1937 and B16F10 cells after 72 h of direct exposure to free CFZ, CFZ-pTA or CFZ-pTA-alb at equivalent CFZ concentrations, and (c) cytotoxicity to B16F10 cells after 72 h of exposure to blank pTA or pTA-alb at concentrations equivalent to their respective percentages in CFZ nanocores (the table shows concentrations of pTA and pTA-alb relative to CFZ concentrations in their corresponding nanocores).

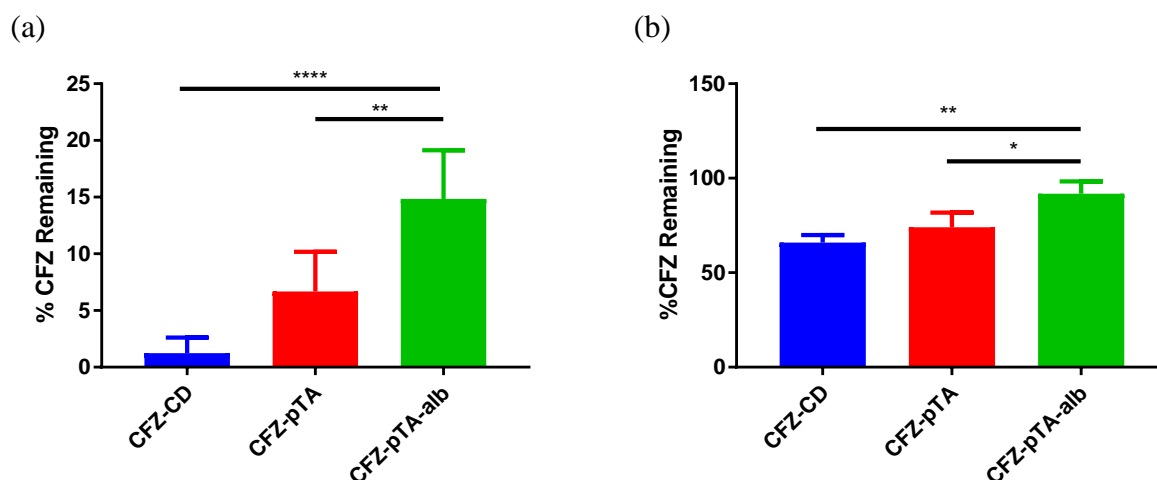


Figure 23: *In vitro* metabolic stability of CFZ in different formulations after incubation at 37 °C in (a) mouse liver homogenate for 60 min or in (b) whole blood for 30 min.

3.4 Discussion

Surface functionalization is needed to enhance NP performance. Modifying NP surface with polymers that prolong its systemic circulation can increase NP accumulation at the tumor (Tali, Aviva, & Alberto, 1995). Ligands with specific affinity to tumor-related markers can enhance NP tumor retention (Xu et al., 2018). NP surface modification can also serve for combination therapy, where drugs bound to the surface are co-delivered with drugs entrapped in the NP (Jia et al., 2015).

In chapter 2 we established the preparation scheme for nanocore formulations with high drug loading in the core and stabilized with TA/Fe³⁺ assemblies on the surface. We next thought of exploring the ability of TA/Fe³⁺ assemblies stabilizing the surface of nanocores to interact with other ligands for surface functionalization. The ability of TA to interact with molecules via hydrogen bonding, hydrophobic interaction, and electrostatic interactions is expected to help functionalize the surface of nanocores with ligands.

3.4.1 PTX-pTA-pDNA

First, PTX-pTA was decorated with nucleic acids. TA binding to DNA was previously reported (Shin et al., 2015). However, whether TA/Fe³⁺ coordination complexes retain this ability was to be confirmed. Surface binding of nucleic acids to the nanocores would allow codelivery of chemotherapeutic drugs (loaded in the core) and nucleic acids (for example; mRNA and siRNA)

for synergistic antitumor effects. In our study we utilized pDNA as a model nucleic acid, and PTX-pTA was used as the nanocore platform. Using gel retardation assay, the weight ratio of PTX-pTA/pDNA that allowed efficient pDNA binding was determined (Figure 12) and was then further challenged to evaluate the binding stability and the nature of pDNA binding. Heparin and DNase represent the negatively charged serum proteins and serum nucleases, respectively. FBS also contains exonucleases similar to those encountered in circulation (Zagorovsky, Chou, & Chan, 2016). Both PB and saline interfere with ionic interactions if present in the carrier-DNA system, while urea interferes with hydrogen bonding (Lim, Rösger, & Englander, 2009). The pDNA binding was resistant to heparin indicating that the negatively charged biopolymers may not decomplex pDNA from pTA (Figure 13c). This could be explained by the fact that the binding was not based on electrostatic interaction (Figure 13f and h), as both pTA and pDNA are negatively charged. The pDNA binding was also stable in DNase (Figure 13d), which indicates that its interaction with pTA was enough for protection of the surface-bound pDNA from serum nucleases. PTX-pTA-pDNA was also stable in FBS as well (Figure 13e and i). Similar stability of DNA to degrading enzymes was previously reported for DNA bound to gold NP via linkers and was attributed to the high DNA density on the NP surface (Zagorovsky et al., 2016). The nature of binding between pTA and pDNA was attributed, at least in part, to hydrogen bonding as it was partially affected by incubation with urea (Figure 13g). This is consistent with the previous report that attributed the strong interaction between TA and DNA to TA hydrophobicity and the numerous hydroxyl groups forming hydrogen-bonds with the DNA phosphate backbone (Labieniec & Gabryelak, 2006).

Next the functionality of the bound pDNA was tested. NCI/ADR-RES ovarian cancer cell line was used for this study as it allows for evaluation of PTX-pTA-pDNA without involving the PTX cytotoxicity. The ability of PTX-pTA-pDNA to enter the cells was evaluated using fluorescently labeled particles (PTX*-pTA), prepared by doping a small quantity of Nile red. Owing to hydrophobicity of Nile red, it is expected to reside in the core with PTX. Free Nile red was also tested in parallel, to ensure that the incorporated Nile red represents PTX-pTA. After incubation of PTX*-pTA or PTX*-pTA-pDNA with NCI/ADR-RES cells for 4 h, fluorescent signals were found associated with the cells both as measured by flow cytometry (Figure 14b) and confocal microscopy (Figure 14c), whereas free Nile red resulted in low diffuse fluorescence. The cells were thoroughly rinsed before analysis to remove surface-bound nanocores; thus, the

differential fluorescence may be interpreted as the nanocores that entered cells and were tightly bound to the cell surface. The *in vitro* transfection efficiency of PTX-pTA-pDNA in NCI/ADR-RES cells was tested and compared with Lipofectamine/pDNA complex. EGFP-expressing pDNA was used as a reporter gene. Cell imaging (Figure 16) and flow cytometry (Figure 17) showed that PTX-pTA-pDNA did not transfect the cells either after 24 or 48 h, in contrast to the Lipofectamine/pDNA complex. The potential reasons for failure of transfection are (i) inability of NP to enter the cells, (ii) instability of pDNA binding such that it is released in the culture medium prior to cell uptake of NP or (iii) insufficient intracellular release of pDNA. Although the association of fluorescent PTX-pTA-pDNA with NCI/ADR-RES cells was observed (Figure 14b and c), it is difficult to distinguish cell uptake and cell binding of PTX-pTA-pDNA; therefore, the first potential remains a viable reason. pDNA bound to PTX-pTA was challenged with either RPMI medium supplemented with 10% FBS (same used in the transfection experiment) and in acetate buffer of pH 5 (to mimic the endosomal pH encountered by NP following cell uptake via endocytosis (Casey, Grinstein, & Orlowski, 2009)). Plasmid DNA stayed well bound to PTX-pTA in serum-containing medium excluding the possibility of pDNA release prior to cell uptake of the particles. However, the stable binding in pH 5 was a sign of potential failure in intracellular release of pDNA. The excessive stability may have been detrimental to timely release of nucleic acid before it becomes degraded in lysosomes (Riley & Vermerris, 2017). The strong irreversible binding between cellular DNA and ellagic acid, one of TA's derivatives was previously reported (Whitley, Stoner, Darby, & Walle, 2003). TA was also reported to intercalate DNA, as evidenced by quenching the EtBr-DNA fluorescence, although the interaction may not be as strong as ellagic acid (Labieniec & Gabryelak, 2006). Moreover, the modification of DNA structure by TA was previously suggested (N. S. Khan, Ahmad, & Hadi, 2000).

3.4.2 PTX-pTA-QA

Secondly, QA derivative was used as a surface ligand. QA has a structural similarity with the fucose moiety of sialyl Lewis-x (sLe^x), a carbohydrate structure expressed on leukocytes surface (Munro et al., 1992). Via sLe^x, leukocytes bind to E-selectin, a transmembrane glycoprotein overexpressed on endothelium supplying various metastatic tumors in response to inflammatory mediators (Brodt et al., 1997; Fox et al., 1995; Nguyen et al., 1997). Therefore, functionalizing the surface of NP with QA may increase the NP delivery to the tumor by increasing

the interaction with peritumoral endothelium. We previously reported a QA derivative (QA-NH₂) was conjugated to a PEG molecule and used to decorate NP (Amoozgar et al., 2013). QA-NH₂ was also used to coat PLGA NP via polydopamine layer, which reacts with nucleophilic amine of QA-NH₂ via Michael Addition/Schiff Base reaction (Xu et al., 2018). These particles accumulated at selectin-upregulated tumors. We hypothesize that QA-NH₂ can bind to the surface of nanocores by interacting with TA via hydrogen bonding and hydrophobic interactions. By incubating PTX-pTA nanocores with QA-NH₂, a QA-coated nanocore was prepared, which was confirmed indirectly by quantifying the unbound molecules remaining in solution and by the reduction in surface charge from bare particles. However, PTX-pTA-QA did not show difference from PTX-pTA in the binding affinity for immobilized E-selectin (Figure 19). Three potential explanations for this result are (i) low QA-NH₂ density on the surface, thus no possible multivalent binding to E-selectin, (ii) instability of QA-NH₂ bound to the nanocore surface (which was not tested) and/or (iii) wrong orientation of QA that does not allow for efficient E-selectin binding. The orientation of QA on the surface is important, where the hydroxyl groups in cyclic QA structure are critical to calcium coordination in E-selectin binding (Girard et al., 2005). It is possible that TA interacted with QA hydroxyl groups by hydrogen bonding, leaving none for E-selectin binding.

3.4.3 CFZ-pTA-alb

Finally, human serum albumin was pursued as a surface modifier. Albumin is the most abundant protein in the body (Alvarez, Carballal, Turell, & Radi, 2010; Kratz, 2008) and has been used as surface coating for NP to enhance their *in vivo* performance (Mariam, Sivakami, & Dongre, 2016). Naked NP introduced into blood circulation become coated with serum proteins, among which immunoglobulin G and complement proteins facilitate the opsonization of NP via the macrophage phagocytic system and consequently NP clearance (Lee, Choi, Webster, Kim, & Khang, 2014). Coating NP with albumin *in vitro* has shown to prolong the circulation of NP via decreasing the adsorption of opsonin proteins (Peng et al., 2013). In addition, for hydrophobic drugs with high binding affinity for albumin, albumin coat can retard drug release from NP (Tao et al., 2012). For surface modification with albumin CFZ nanocores (CFZ-pTA) were chosen as a platform. CFZ is an epoxyketone peptide and a second-generation proteasome inhibitor recently approved for multiple myeloma (MM) treatment (Nooka, Gleason, Casbourne, & Lonial, 2013). Proteasome inhibition results in accumulation of misfolded proteins in the cell, leading to

endoplasmic reticulum (ER) stress, and inhibition of NF- κ B pathway, eventually inducing cell apoptosis (Kortuem & Stewart, 2013). When cells are under ER stress, both survival and death factors are transduced, with the former being more represented initially to prolong cell survival. However, when cells are kept under sustained ER stress, death factors accumulate to a higher extent inducing cell death (Corazzari, Gagliardi, Fimia, & Piacentini, 2017). Despite the high efficacy against MM, CFZ has not proven effective against solid tumors because of rapid inactivation in blood (>95% cleared within 30 min) due to epoxide hydrolysis and cleavage of the peptide backbone (Papadopoulos et al., 2013; Yang et al., 2011). Therefore, a NP formulation, such as CFZ-pTA, which can load CFZ with high capacity and protect the drug may make it useful for the therapy of solid tumors. We hypothesized that the coating CFZ-pTA with albumin would additionally sustain CFZ release to keep tumor cells under sustained ER stress for stable therapeutic response.

The strong interaction between TA and albumin was previously reported and suggested to be via hydrogen bonding and hydrophobic interactions (Labieniec & Gabryelak, 2006). Accordingly, the pTA coat was expected to interact with albumin allowing surface decoration. By incubating CFZ-pTA in albumin solution and washing to remove unbound albumin, CFZ-pTA-alb was prepared. The slight reduction in surface charge (-20.6 ± 3.1 mV vs -26.5 ± 3.5 mV, for CFZ-pTA-alb and CFZ-pTA, respectively) indicated the coverage of the pTA layer with albumin. Albumin coating was further confirmed using SDS-PAGE (Figure 20b). CFZ-pTA-alb showed colloidal stability in FBS (Figure 20c) and is thus expected to maintain its physical stability *in vivo* allowing prolonged circulation time.

To study the role of albumin in controlling CFZ release, an *in vitro* release experiment was done. Typically, centrifugation or dialysis methods are used for evaluating drug release kinetics from NP. However, efficient centrifugation of the nanocore formulations was not feasible. At very high speeds (> 90,000 rcf) particles underwent irreversible aggregation. In addition, the use of a dialysis bag to contain the CFZ loaded nanocores was not favorable. First, free CFZ adsorbed to a high extent to the inner side of the dialysis bag. This would not only underestimate the release rate but would also abolish the differences between formulations where the CFZ unbinding from the membrane becomes a rate limiting step. Moreover, limited by the dialysis bag dimensions, large volume of medium would be needed which results in CFZ concentrations below the HPLC analysis detection limit. Therefore, the release study was performed using a PEGDA hydrogel method

which we previously established (Sun et al., 2016). The merit of this method is that it eliminates the need for centrifugation pressure during sampling, allows particles to remain suspended throughout the incubation, and prevents sample loss due to the adsorption to the container. However, with the hydrogel matrix serving as a barrier to drug diffusion, the release rates measured would be much slower than the actual ones. Therefore, we acknowledge that this method would be suitable for rank-ordering formulations and not intended for accurately predicting the *in vivo* release kinetics. CFZ-pTA-alb had significantly slower release rate than CFZ-pTA (Figure 21a) indicating that albumin coat served as an additional barrier to CFZ release from the particles. It is possible that CFZ released from the core binds to the adsorbed albumin on the surface. With albumin being the most abundant plasma protein, this result is consistent with the extensive plasma protein binding previously reported for CFZ (May 2016; Wang et al., 2013). The use of human serum albumin as a diffusion barrier was previously reported for mitoxantrone-loaded pullulan NP (Tao et al., 2012). Mitoxantrone, known for its high binding affinity to albumin (S. N. Khan et al., 2008), showed delayed release rate in presence of the albumin coat. It was also explained as a surface steric hindrance effect delaying drug diffusion to the medium (Tao et al., 2012). Therefore, CFZ-pTA-alb is expected to stably carry its CFZ payload in circulation and avoid premature release increasing the chance of CFZ accumulation at the tumor site.

Due to its rapid inactivation in circulation via epoxide ring hydrolysis and peptidase cleavage, CFZ did not show efficacy in patients with solid tumors where the active form does not efficiently reach the tumor site (Papadopoulos et al., 2013; Yang et al., 2011). An NP formulation that protects CFZ during circulation from degrading enzymes could enhance accumulation of its active form at solid tumors. The metabolic stability of CFZ nanocore formulations were compared to that of CFZ-CD, a cyclodextrin-based CFZ solution, used to mimic the clinically used formulation, Kyprolis® (Ji Eun Park et al., 2017; J. E. Park et al., 2017). In both mouse blood and liver homogenate, CFZ was least stable as CFZ-CD and most protected by CFZ-pTA-alb (Figure 21b and c). The higher protection offered by the albumin coat agrees with the release and cytotoxicity data (Figure 21 and Figure 22). Collectively, these results indicate that CFZ-pTA-alb can protect CFZ against metabolic degradation and extend its circulation time *in vivo*.

3.5 Conclusion

This chapter explored the ability of TA/Fe³⁺ assemblies on the surface of nanocores to interact with ligands. Three surface ligands were pursued: nucleic acid (pDNA), quinic acid derivative (QA), and albumin. The nanocore surface was successfully decorated by the three ligands, and their functionality was evaluated. The pDNA-bound nanocore did not transfect NCI/ADR-RES, potentially due to irreversible binding between TA and pDNA and very slow intracellular pDNA release. The QA-bound nanocores did not specifically bind to E-selectin, possibly due to insufficient QA density on the surface, weak binding affinity of QA for the nanocore surface and/or unavailability of QA hydroxyl groups for efficient E-selectin binding. The albumin coat on CFZ-pTA-alb nanocores provided a barrier to CFZ release and protection against metabolic degradation. Therefore, CFZ-pTA-alb warrants further investigation with respect to improved delivery of active CFZ to solid tumor sites.

3.6 References

- Abouelmagd, S. A., Meng, F., Kim, B.-K., Hyun, H., & Yeo, Y. (2016). Tannic Acid-Mediated Surface Functionalization of Polymeric Nanoparticles. *ACS Biomaterials Science & Engineering*, 2(12), 2294-2303. doi: 10.1021/acsbiomaterials.6b00497
- Alvarez, B., Carballal, S., Turell, L., & Radi, R. (2010). Chapter 5 - Formation and Reactions of Sulfenic Acid in Human Serum Albumin. In E. Cadenas & L. Packer (Eds.), *Methods in Enzymology* (Vol. 473, pp. 117-136): Academic Press.
- Amoozgar, Z., Park, J., Lin, Q., Weidle, J. H., & Yeo, Y. (2013). Development of Quinic Acid-Conjugated Nanoparticles as a Drug Carrier to Solid Tumors. *Biomacromolecules*, 14(7), 2389-2395. doi: 10.1021/bm400512g
- Brodth, P., Fallavollita, L., Bresalier, R. S., Meterissian, S., Norton, C. R., & Wolitzky, B. A. (1997). Liver endothelial E-selectin mediates carcinoma cell adhesion and promotes liver metastasis. *International Journal of Cancer*, 71(4), 612-619. doi: 10.1002/(sici)1097-0215(19970516)71:4<612::aid-ijc17>3.0.co;2-d
- Casey, J. R., Grinstein, S., & Orlowski, J. (2009). Sensors and regulators of intracellular pH. [Review Article]. *Nature Reviews Molecular Cell Biology*, 11, 50. doi: 10.1038/nrm2820 <https://www.nature.com/articles/nrm2820#supplementary-information>
- Corazzari, M., Gagliardi, M., Fimia, G. M., & Piacentini, M. (2017). Endoplasmic Reticulum Stress, Unfolded Protein Response, and Cancer Cell Fate. *Frontiers in oncology*, 7, 78-78. doi: 10.3389/fonc.2017.00078
- EMA/517040/2016. (May 2016). Group of variations including an extension of indication assessment report. Retrieved Access date: Oct 2018, from https://www.ema.europa.eu/documents/variation-report/kyprolis-h-c-3790-ii-0001-g-epar-assessment-report-variation_en.pdf
- Feng, M., Ibrahim, B. M., Wilson, E. M., Doh, K. O., Bergman, B. K., Park, C., & Yeo, Y. (2014). Stabilization of a hyaluronate-associated gene delivery system using calcium ions. *Biomater Sci*, 2(6), 936-942.
- Fox, S. B., Turner, G. D. H., Gatter, K. C., & Harris, A. L. (1995). The increased expression of adhesion molecules ICAM-3, E- and P-selectins on breast cancer endothelium. *The Journal of Pathology*, 177(4), 369-376. doi: 10.1002/path.1711770407
- Girard, C., Dourlat, J., Savarin, A., Surcin, C., Leue, S., Escriou, V., . . . Scherman, D. (2005). Sialyl Lewisx analogs based on a quinic acid scaffold as the fucose mimic. *Bioorganic & Medicinal Chemistry Letters*, 15(13), 3224-3228. doi: <https://doi.org/10.1016/j.bmcl.2005.05.004>
- Jia, H.-Z., Zhang, W., Zhu, J.-Y., Yang, B., Chen, S., Chen, G., . . . Zhang, X.-Z. (2015). Hyperbranched-hyperbranched polymeric nanoassembly to mediate controllable co-delivery of siRNA and drug for synergistic tumor therapy. *Journal of Controlled Release*, 216, 9-17. doi: <https://doi.org/10.1016/j.jconrel.2015.08.006>
- Khan, N. S., Ahmad, A., & Hadi, S. M. (2000). Anti-oxidant, pro-oxidant properties of tannic acid and its binding to DNA. *Chemico-Biological Interactions*, 125(3), 177-189. doi: [https://doi.org/10.1016/S0009-2797\(00\)00143-5](https://doi.org/10.1016/S0009-2797(00)00143-5)
- Khan, S. N., Islam, B., Yennamalli, R., Sultan, A., Subbarao, N., & Khan, A. U. (2008). Interaction of mitoxantrone with human serum albumin: Spectroscopic and molecular modeling studies. *European Journal of Pharmaceutical Sciences*, 35(5), 371-382. doi: <https://doi.org/10.1016/j.ejps.2008.07.010>

- Kortuem, K. M., & Stewart, A. K. (2013). Carfilzomib. [10.1182/blood-2012-10-459883]. *Blood*, *121*(6), 893.
- Kratz, F. (2008). Albumin as a drug carrier: Design of prodrugs, drug conjugates and nanoparticles. *Journal of Controlled Release*, *132*(3), 171-183. doi: <https://doi.org/10.1016/j.jconrel.2008.05.010>
- Labieniec, M., & Gabryelak, T. (2006). Interactions of tannic acid and its derivatives (ellagic and gallic acid) with calf thymus DNA and bovine serum albumin using spectroscopic method. [Comparative Study]. *J Photochem Photobiol B*, *82*(1), 72-78. doi: [10.1016/j.jphotobiol.2005.09.005](https://doi.org/10.1016/j.jphotobiol.2005.09.005)
- Lee, Y. K., Choi, E.-J., Webster, T. J., Kim, S.-H., & Khang, D. (2014). Effect of the protein corona on nanoparticles for modulating cytotoxicity and immunotoxicity. *International Journal of Nanomedicine*, *10*, 97-113. doi: [10.2147/ijn.s72998](https://doi.org/10.2147/ijn.s72998)
- Lim, W. K., Rösgen, J., & Englander, S. W. (2009). Urea, but not guanidinium, destabilizes proteins by forming hydrogen bonds to the peptide group. *Proceedings of the National Academy of Sciences of the United States of America*, *106*(8), 2595-2600. doi: [10.1073/pnas.0812588106](https://doi.org/10.1073/pnas.0812588106)
- Mariam, J., Sivakami, S., & Dongre, P. M. (2016). Albumin corona on nanoparticles - a strategic approach in drug delivery. [Review]. *Drug Deliv*, *23*(8), 2668-2676. doi: [10.3109/10717544.2015.1048488](https://doi.org/10.3109/10717544.2015.1048488)
- Munro, J. M., Lo, S. K., Corless, C., Robertson, M. J., Lee, N. C., Barnhill, R. L., . . . Bevilacqua, M. P. (1992). Expression of sialyl-Lewis X, an E-selectin ligand, in inflammation, immune processes, and lymphoid tissues. *The American Journal of Pathology*, *141*(6), 1397-1408.
- Nguyen, M., Corless, C. L., Kräling, B. M., Tran, C., Atha, T., Bischoff, J., & Barsky, S. H. (1997). Vascular expression of E-selectin is increased in estrogen-receptor-negative breast cancer: a role for tumor-cell-secreted interleukin-1 alpha. *The American Journal of Pathology*, *150*(4), 1307-1314.
- NIH. Cell Line NCI/ADR-RES is an Ovarian tumor cell line, not a Breast line. Retrieved Dec 12th 2018, from https://dtp.cancer.gov/discovery_development/nci-60/nci-adrres.htm
- Nooka, A., Gleason, C., Casbourne, D., & Lonial, S. (2013). Relapsed and refractory lymphoid neoplasms and multiple myeloma with a focus on carfilzomib. *Biologics : Targets & Therapy*, *7*, 13-32. doi: [10.2147/btt.s24580](https://doi.org/10.2147/btt.s24580)
- Papadopoulos, K. P., Burris, H. A., Gordon, M., Lee, P., Sausville, E. A., Rosen, P. J., . . . Infante, J. R. (2013). A phase I/II study of carfilzomib 2–10-min infusion in patients with advanced solid tumors. *Cancer Chemotherapy and Pharmacology*, *72*(4), 861-868. doi: [10.1007/s00280-013-2267-x](https://doi.org/10.1007/s00280-013-2267-x)
- Park, J., Brust, T. F., Lee, H. J., Lee, S. C., Watts, V. J., & Yeo, Y. (2014). Polydopamine-Based Simple and Versatile Surface Modification of Polymeric Nano Drug Carriers. *ACS Nano*, *8*(4), 3347-3356. doi: [10.1021/nn405809c](https://doi.org/10.1021/nn405809c)
- Park, J. E., Chun, S.-E., Reichel, D., Park, J., Min, J. S., Ryoo, G., . . . Lee, W. (2017). Novel Polymer Micelle and Nanocrystal Formulations for the Proteasome Inhibitor Drug Carfilzomib: Pharmacokinetic and Pharmacodynamic Studies in Human Lung and Breast Cancer Models. *The FASEB Journal*, *31*(1_supplement), 822.826-822.826. doi: [10.1096/fasebj.31.1_supplement.822.6](https://doi.org/10.1096/fasebj.31.1_supplement.822.6)

- Park, J. E., Chun, S. E., Reichel, D., Min, J. S., Lee, S. C., Han, S., . . . Lee, W. (2017). Polymer micelle formulation for the proteasome inhibitor drug carfilzomib: Anticancer efficacy and pharmacokinetic studies in mice. *PLoS ONE*, *12*(3), e0173247. doi: 10.1371/journal.pone.0173247
- Peng, Q., Zhang, S., Yang, Q., Zhang, T., Wei, X.-Q., Jiang, L., . . . Lin, Y.-F. (2013). Preformed albumin corona, a protective coating for nanoparticles based drug delivery system. *Biomaterials*, *34*(33), 8521-8530. doi: <https://doi.org/10.1016/j.biomaterials.2013.07.102>
- Riley, M. K., & Vermerris, W. (2017). Recent Advances in Nanomaterials for Gene Delivery-A Review. *Nanomaterials (Basel, Switzerland)*, *7*(5), 94. doi: 10.3390/nano7050094
- Shamay, Y., Elkabets, M., Li, H., Shah, J., Brook, S., Wang, F., . . . Heller, D. A. (2016). P-selectin is a nanotherapeutic delivery target in the tumor microenvironment. [10.1126/scitranslmed.aaf7374]. *Science Translational Medicine*, *8*(345), 345ra387.
- Shen, G., Xing, R., Zhang, N., Chen, C., Ma, G., & Yan, X. (2016). Interfacial Cohesion and Assembly of Bioadhesive Molecules for Design of Long-Term Stable Hydrophobic Nanodrugs toward Effective Anticancer Therapy. *ACS Nano*, *10*(6), 5720-5729. doi: 10.1021/acsnano.5b07276
- Shin, M., Ryu, J. H., Park, J. P., Kim, K., Yang, J. W., & Lee, H. (2015). DNA/Tannic Acid Hybrid Gel Exhibiting Biodegradability, Extensibility, Tissue Adhesiveness, and Hemostatic Ability. *Advanced Functional Materials*, *25*(8), 1270-1278. doi: 10.1002/adfm.201403992
- Sileika, T. S., Barrett, D. G., Zhang, R., Lau, K. H. A., & Messersmith, P. B. (2013). Colorless Multifunctional Coatings Inspired by Polyphenols Found in Tea, Chocolate, and Wine. *Angewandte Chemie International Edition*, *52*(41), 10766-10770. doi: 10.1002/anie.201304922
- Sun, B., Taha, M. S., Ramsey, B., Torregrosa-Allen, S., Elzey, B. D., & Yeo, Y. (2016). Intraperitoneal chemotherapy of ovarian cancer by hydrogel depot of paclitaxel nanocrystals. *Journal of Controlled Release*, *235*(Supplement C), 91-98. doi: <https://doi.org/10.1016/j.jconrel.2016.05.056>
- Tali, S., Aviva, H., & Alberto, G. (1995). Doxorubicin encapsulated in sterically stabilized liposomes for the treatment of a brain tumor model: biodistribution and therapeutic efficacy. *Journal of Neurosurgery*, *83*(6), 1029-1037. doi: 10.3171/jns.1995.83.6.1029
- Tao, X., Zhang, Q., Ling, K., Chen, Y., Yang, W., Gao, F., & Shi, G. (2012). Effect of pullulan nanoparticle surface charges on HSA complexation and drug release behavior of HSA-bound nanoparticles. [Research Support, Non-U.S. Gov't]. *PLoS ONE*, *7*(11), e49304. doi: 10.1371/journal.pone.0049304
- Wang, Z., Yang, J., Kirk, C., Fang, Y., Alsina, M., Badros, A., . . . Infante, J. R. (2013). Clinical pharmacokinetics, metabolism, and drug-drug interaction of carfilzomib. [Clinical Trial Research Support, Non-U.S. Gov't]. *Drug Metab Dispos*, *41*(1), 230-237. doi: 10.1124/dmd.112.047662
- Whitley, A. C., Stoner, G. D., Darby, M. V., & Walle, T. (2003). Intestinal epithelial cell accumulation of the cancer preventive polyphenol ellagic acid--extensive binding to protein and DNA. [Research Support, U.S. Gov't, P.H.S.]. *Biochem Pharmacol*, *66*(6), 907-915.
- Xu, J., Lee, S. S.-Y., Seo, H., Pang, L., Jun, Y., Zhang, R.-Y., . . . Yeo, Y. (2018). Quinic Acid-Conjugated Nanoparticles Enhance Drug Delivery to Solid Tumors via Interactions with Endothelial Selectins. *Small*, *14*(50), 1803601. doi: 10.1002/sml.201803601

- Yang, J., Wang, Z., Fang, Y., Jiang, J., Zhao, F., Wong, H., . . . Kirk, C. J. (2011). Pharmacokinetics, Pharmacodynamics, Metabolism, Distribution, and Excretion of Carfilzomib in Rats. [10.1124/dmd.111.039164]. *Drug Metabolism and Disposition*, 39(10), 1873.
- Zagorovsky, K., Chou, L. Y. T., & Chan, W. C. W. (2016). Controlling DNA–nanoparticle serum interactions. *Proceedings of the National Academy of Sciences*, 113(48), 13600-13605. doi: 10.1073/pnas.1610028113

CHAPTER 4. EVALUATION OF PHARMACODYNAMICS OF ALBUMIN-COATED NANOCORES IN MURINE TUMOR MODELS

A version of this chapter will be submitted for review.

4.1 Introduction

CFZ, a second-generation proteasome inhibitor recently approved for MM treatment (Nooka, Gleason, Casbourne, & Lonial, 2013), has not proven effective against solid tumors due to rapid inactivation in blood (Papadopoulos et al., 2013; Yang et al., 2011). The *in vitro* tests described in chapter 3 demonstrated that coating CFZ nanocore formulation with albumin offered sustained release of CFZ and protection against metabolic degradation. Based on this, it was hypothesized that CFZ-pTA-alb can circulate systemically *in vivo* without premature CFZ release and protect it from metabolizing enzymes, thus increasing the accumulation of active CFZ in solid tumors.

In addition, the sustained CFZ release might be beneficial in mimicking metronomic chemotherapy. Metronomic schedules denote the frequent or prolonged administration of chemotherapeutics at much lower doses than those used in MTDs regimens (Kareva, Waxman, & Lakka Klement, 2015). While MTDs target sensitive cancer cells, usually resulting in tumor relapse and drug resistance, metronomic chemotherapy targets the tumor microenvironment, disengaging the tumor from its support system and resulting in long lasting tumor regression. Sustained low doses of chemotherapeutics results in profound antiangiogenic effects (Browder et al., 2000; Klement et al., 2000), activates the antitumor immunity without killing immune cells recruited to the tumor (Banissi, Ghiringhelli, Chen, & Carpentier, 2009; Ghiringhelli et al., 2007), and avoids the induction of tumor-initiating cancer stem cells (Chan et al., 2016). As a proteasome inhibitor, CFZ puts tumor cells under ER stress, a condition which if maintained for a prolonged time will induce cell death (Corazzari, Gagliardi, Fimia, & Piacentini, 2017; Lee, Iwakoshi, Anderson, & Glimcher, 2003). Therefore, CFZ would theoretically benefit from the sustained release formulation by keeping tumor cells under prolonged ER stress for a more sustained therapeutic response. Moreover, CFZ is a potential immunogenic cell death (ICD) inducer, causing tumor cell apoptosis to activate the immune system resulting in a long-lasting antitumor immunity

(Jarauta et al., 2016; Tang et al., 2018). To develop effective antitumor immunity, it is essential to avoid killing of immune cells recruited to the tumor. The sustained release of CFZ at low dose at the tumor site would minimize the killing of chemo-sensitive immune cells, in contrast to a bolus dose. Collectively, CFZ-pTA-alb is expected to make CFZ beneficial for solid tumor therapy.

In this chapter, the antitumor effect of CFZ-pTA-alb, in comparison to the commercial CFZ-CD, was evaluated in murine tumor models. Two syngeneic mouse models (B16F10 melanoma in C57BL/6 mice, and CT26 colon carcinoma in BALB/c mice), which preserve functional immune systems, were used to study the role of NP-mediated chemotherapy in antitumor immune effects. First, systemic intravenous (IV) injection route was utilized and the antitumor effect was evaluated, and a localized intratumoral (IT) route was used to evaluate the antitumor effects as well as the tumor immune-phenotype in response to sustained CFZ release. The ability of CFZ-pTA-alb to vaccinate the mice, producing long-lasting antitumor immunity that protects the mice against tumor re-challenges, was evaluated.

4.2 Materials and Methods

4.2.1 Materials

Human serum albumin ($\geq 96\%$ agarose gel electrophoresis) and 2-hydroxypropyl- β -cyclodextrin were purchased from Sigma–Aldrich (St. Louis, MO, USA). (3-(4,5-Dimethylthiazol-2-yl)- 2,5- diphenyltetrazolium bromide) (MTT) and mouse interferon-gamma (IFN- γ) ELISA kit were purchased from Invitrogen (Eugene, OR, USA). GM-CSF was purchased from Peprotech (Rock Hill, NJ, USA). IL-4, purified rat anti-mouse CD16/CD32 (Fc block), APC anti-mouse CD11c, FITC anti-mouse CD40, PE anti-mouse CD86, FITC anti-mouse CD4 and APC anti-mouse CD8a were purchased from Biolegend (San Diego, CA, USA). AH1 peptide was purchased from Anaspec (Fremont, CA, USA). Deoxyribonuclease I (DNase I), collagenase and hyaluronidase were purchased from Worthington (Lakewood, NJ, USA).

4.2.2 *In vitro* experiments

4.2.2.1 Cytotoxicity of bolus versus sustained CFZ

B16F10 cells were seeded at 4,000 cells per well in a 96 well plate and incubated until cells reached 70-80% confluency. CFZ solution was treated to the cells at 1, 10, 100, 1000 or 10,000

nM for 2.4 h followed by incubation in drug-free medium for the rest of 24 h, for the bolus regimen, or treated at 0.1, 1, 10, 100 or 1000 nM for 24 h, for the sustained regimen. Spleen cells were obtained from freshly harvested spleen of male C57BL/6 mice. Spleen was cut into pieces and filtered through 70 μ m then 40 μ m cell strainer to obtain single cell suspension and incubated with 1 mL ACK lysis buffer for 1 min to eliminate red blood cells. Spleen cells were seeded at 200,000 cells per well and treated as above. At the end of 24 h incubation, cell viability was determined using MTT assay. Briefly, 100 μ L of fresh medium and 15 μ L of MTT solution (5 mg/mL) replaced the medium and cells were incubated for 4 hours. Stop solution (100 μ L) (50 % DMSO, 20% SDS and 0.02% acetic acid) was added to solubilize formazan crystals. Next day, absorbance was measured using a SpectraMax M3 microplate reader (Molecular Device, Sunnyvale, CA) at 529 nm.

4.2.2.2 Dendritic cells phagocytosis

Bone marrow cells were collected from C57BL/6 or Balb/c mice using a syringe. After treatment with ACK buffer and washing, cells were suspended (2×10^6 cells/10 mL) in IMDM medium supplemented with 10% FBS, 1% P/S, 20 ng/mL GM-CSF, 40 ng/mL IL-4, and 10 mM β -mercaptoethanol (day 0). Additional media was added on day 3, and floating and loosely adherent cells were collected by centrifugation on day 6. DC differentiation was confirmed with CD11c staining. DC (100,000 cells) were cocultured in non-tissue culture-treated 6 well plates, with 400,000 B16F10 cells that were either nontreated or treated for 24 h with blank pTA-alb, CFZ solution or CFZ-pTA-alb (at 10 μ M CFZ equivalent) and rinsed once. B16F10 cells were labeled with DiI prior to the different treatments. The coculture was incubated for 4 h, then cells were collected and resuspended in staining buffer. Cells were incubated with Fc block for 5 min then stained with APC anti-mouse CD11c. Phagocytosis was quantified as the percentage of DiI⁺/CD11c⁺ cells among the CD11c⁺ cells.

4.2.3 Systemic administration

4.2.3.1 Antitumor effect

All animal procedures were approved by Purdue Animal Care and Use Committee, in conformity with the NIH guidelines for the care and use of laboratory animals. Male C57BL/6 mice (5-6 week old, ~20 g), were purchased from Envigo (Indianapolis, IN, USA) and acclimatized

for 1 week prior to tumor inoculation. One million B16F10 melanoma cells were inoculated subcutaneously in the upper flank of the mice right hind limb. When the tumors reached $\sim 100 \text{ mm}^3$, the mice were randomly assigned to 3 groups (n=5 for PBS, n=6 for CFZ-CD and n=9 for CFZ-pTA-alb, equivalent to 6 mg/kg of CFZ). One hundred microliter of each treatment was injected via tail vein on 2 consecutive days (QDx2) for 2 weeks. Tumor volume and mice weight were measured every day. The tumor length (L) and width (W) were measured using a digital caliper and the volume (V) was calculated using the formula: $V = (L \times W^2)/2$. The specific growth rate of the tumor was calculated as $\Delta \log V / \Delta t$ (t: time in days). Animals losing >20% body weight or with tumors reaching over 10% of the body weight were humanely sacrificed before the end of the study.

4.2.3.2 Biodistribution and blood chemistry

PBS, CFZ-CD, CFZ-pTA-alb or blank pTA-alb (6 mg/kg CFZ equivalent) were injected via tail vein of B16F10 bearing C57BL/6 mice (with 100 mm^3 tumors) on 2 consecutive days. The mice were sacrificed 48 h after the last injection and blood was collected via cardiac puncture and serum was separated for blood chemistry testing. Tumor and major organs were harvested, washed with PBS and snap-frozen and kept at -80°C until analysis. To quantify CFZ in the tissues, tissues were homogenized in cold PBS (pH 7.4) (100 mg tissue per 400 μL) with Omni Tissue Master 125 homogenizer. For 100 μL of each tissue homogenate, 200 μL Triton-X (5%) was added and vortexed for 2 min. CFZ was extracted by adding TBME (1800 μL) containing carfilzomib-d8 (Cayman Chemical, Ann Arbor, MI, USA) as an internal standard (250 ng/mL) and mixed by rotation for 40 min. The organic layer was separated by centrifugation at 4,500 rcf for 15 min, transferred to glass vials and evaporated under vacuum. The dried films were reconstituted in 100 μL acetonitrile and transferred to vials for LC-MS/MS analysis. An individual standard curve was prepared by spiking CFZ in respective tissue homogenates to yield the final concentrations of 500, 250, 125, 62.25, 31.13, 15.56, 7.78, 3.89, 1.99, and 0.99 ng/mL and processed in the same way as the samples. For analysis of blood chemistry, the collected blood was clotted in a silica-coated tube and analyzed by Purdue Clinical Pathology Laboratory.

4.2.4 Local administration

4.2.4.1 Antitumor effect in B16F10 tumor model

One million B16F10 melanoma cells were inoculated subcutaneously in the upper flank of C57BL/6 mice right hind limb. When the tumors reached $\sim 100 \text{ mm}^3$, the mice were randomly assigned to 3 groups. Fifty microliters of PBS (n=4), CFZ-CD (n=5) or CFZ-pTA-alb (n=5) (1.2 μg CFZ equivalent) were injected intratumorally on day 0. Tumor size was monitored for 7 days, then mice were sacrificed, and tumor and spleen were collected. Tumors were subjected to immunophenotyping, and spleens were used to evaluate the tumor-specific immunity.

4.2.4.2 B16F10 tumor immunophenotyping

Harvested B16F10 tumors were cut into small pieces and mechanically minced. Dissociated tumors were filtered through cell strainer (70 μm then 40 μm) to obtain single cell suspension and incubated with 3 mL ammonium-chloride-potassium (ACK) lysis buffer for 1 min to eliminate red blood cells. Cells were washed with PBS, resuspended in cell staining buffer (1x10⁶ cells in 100 μL) and incubated with Fc block for 5 min. Cells were stained with PE anti-mouse CD8a for 1 h at 4 °C. Cells were washed and suspended in cell staining buffer for analysis using flow cytometer (Accuri C6, BD Biosciences, San Jose, CA).

4.2.4.3 Tumor-specific immunity

Splenocytes (2,000,000 cells) from treated B16F10 bearing mice were seeded into 6 well plate and stimulated with 100 μg of irradiated B16F10 tumor lysate (control well contained spleen cells with no tumor lysate). Cells were incubated for 72 h and then centrifuged down to collect the supernatant. The concentration of interferon gamma (IFN- γ) was measured in the collected supernatants using BD™ Cytometric Bead Array (CBA) kit.

4.2.4.4 CFZ retention in tumor

Fifty microliters of CFZ-CD or CFZ-pTA-alb (1.2 μg CFZ equivalent) were injected intratumorally into 100 mm^3 B16F10 tumors (inoculated in C57BL/6 mice). Two hours later the mice were sacrificed, blood was collected via cardiac puncture into heparinized tubes and the tumors were harvested, washed with PBS and processed for CFZ quantification (as above). To measure CFZ concentration in plasma, 40 μL of acetonitrile (containing 250 ng/mL CFZ-d8) was

added to 5 μ L plasma, made up to 20 μ L with water. The mixture was vortexed for 5 min then centrifuged at 16,000 g for 10 min. The supernatant was transferred to vials for LC-MS/MS analysis. An individual standard curve was prepared by spiking CFZ in plasma to yield the final concentrations of 416.7, 208.3, 104.2, 52.08, 26.04, 13.02, 6.51 and 3.26 ng/mL and processed in the same way as the samples.

4.2.4.5 Antitumor effect in CT26 tumor model

CT26 mouse colon carcinoma cells (ATCC, USA) (100,000 cells) were inoculated in the mammary fat pad of Balb/c mice. When the tumors reached ~ 100 mm³, the mice were randomly assigned to 3 groups. Fifty microliters of PBS (n=3), CFZ-CD (n=4) or CFZ-pTA-alb (n=4) (1.2 μ g CFZ equivalent) were injected intratumorally on day 0. Tumor size was monitored for 7 days.

4.2.4.6 Abscopal effect in CT26 tumor model

To test the generation of adaptive immunity in response to treatment, BALB/c mice were inoculated with CT26 tumors at different sites. CT26 cells were inoculated subcutaneously (300,000 cells) in the upper flank of right hind limb of BALB/c mice. Either on the same day or 7 days later, the same mice were inoculated subcutaneously in the upper flank of left hind limb with 100,000 CT26 cells. When the right-side tumors reached ~ 50 mm³, the mice were randomly assigned to 3 groups. Twenty microliters of PBS (n=6), CFZ-CD (n=5) or CFZ-pTA-alb (n=6) (60 μ g CFZ equivalent) were injected intratumorally in the right-side tumors. Size of the treated tumors and tumor appearance/size on the left side were monitored. The criteria for early sacrifice of animals were over 20% body weight loss, tumors excessively ulcerating or reaching over 10% of the body weight. For mice inoculated on different days, they were sacrificed on day 22 post treatment. Spleen and draining lymph node (DLN) were collected and used to evaluate the tumor-specific immunity. Spleen or DLN cells (300,000 cells) from treated CT26 bearing mice were seeded into 96 well plate and were stimulated with 10 μ g/mL of AH1 peptide (control well contained spleen cells with no tumor lysate). GM-CSF was added to all wells at 20 ng/mL. Cells were incubated for 72 h then centrifuged at 300 g for 5 min to collect supernatant. Level of IFN- γ production was measured in the collected supernatants using ELISA kit.

4.3 Results

4.3.1 Antitumor effect and biodistribution with systemic administration

Antitumor effect of CFZ-pTA-alb in comparison to CFZ-CD was evaluated upon systemic administration in a syngeneic mouse model of B16F10 melanoma (B16F10@C57BL/6). Treatments were injected via tail vein on two consecutive days (QDx2) to mimic the clinical dosing schedule for CFZ in MM therapy (Jakubowiak, 2014) and the CFZ dose used (6 mg/kg) was previously reported for mice preclinical studies (Mehta et al., 2015). At this dose, CFZ-CD did not show difference from the control group, whereas CFZ-pTA-alb treatment significantly delayed tumor growth (Figure 24a). The specific growth rate, which describes the rate of exponential tumor growth in each animal, showed significant difference of CFZ-pTA-alb from both CFZ-CD and PBS groups ($p < 0.001$ and $p < 0.0001$, respectively, one-way ANOVA with Tukey's multiple comparisons test) (Figure 24b). (Some of the tumors, from the control group, grew beyond the endpoint and required early sacrifice of animals before the completion of remaining doses; therefore, statistical comparison was performed only for 7-day period post-treatment.)

CFZ biodistribution was examined at 48 h after IV administration of 2 consecutive doses (an equivalent of 6 mg/kg *2). the CFZ-pTA-alb group showed higher CFZ accumulation in the tumor as well as liver, spleen and lungs (Figure 25). Therefore, CFZ-pTA-alb enhanced the tumor accumulation of CFZ by protecting the drug against degradation in circulation. Additionally, CFZ levels in the kidneys were lower in the CFZ-pTA-alb group indicating low CFZ release from the nanocores in circulation. It is noteworthy that the absolute levels of CFZ in the tissues could have been higher than measured, because CFZ binds irreversibly to its target sites in the proteasome making it difficult to quantify the entire drug in each tissue. Moreover, the real significant difference between formulations might have not been realized due to the delayed time of sacrifice and tissue analysis (48 h after the last treated dose).

Although CFZ-pTA-alb attenuated the tumor growth, the animals treated with CFZ-pTA-alb ultimately succumbed to death with additional injections (Figure 26a), likely due to cumulative off-target effects of potent CFZ. The off-target toxicity was not reflected on the mice body weight, where mice in all groups did not lose weight with injections until their death or sacrifice (Figure 26b). Blood chemistry 48 h after IV administration of 2 consecutive doses (an equivalent of 6 mg/kg *2) also did not show any difference from those of the PBS group and other treatments (Figure 27). Blood chemistry analysis was not performed after 4 injections, as some of the mice

were either sacrificed due to tumor growth (in PBS and CFZ-CD groups) or deceased due to accumulated toxicity (in CFZ-pTA-alb group) by that time.

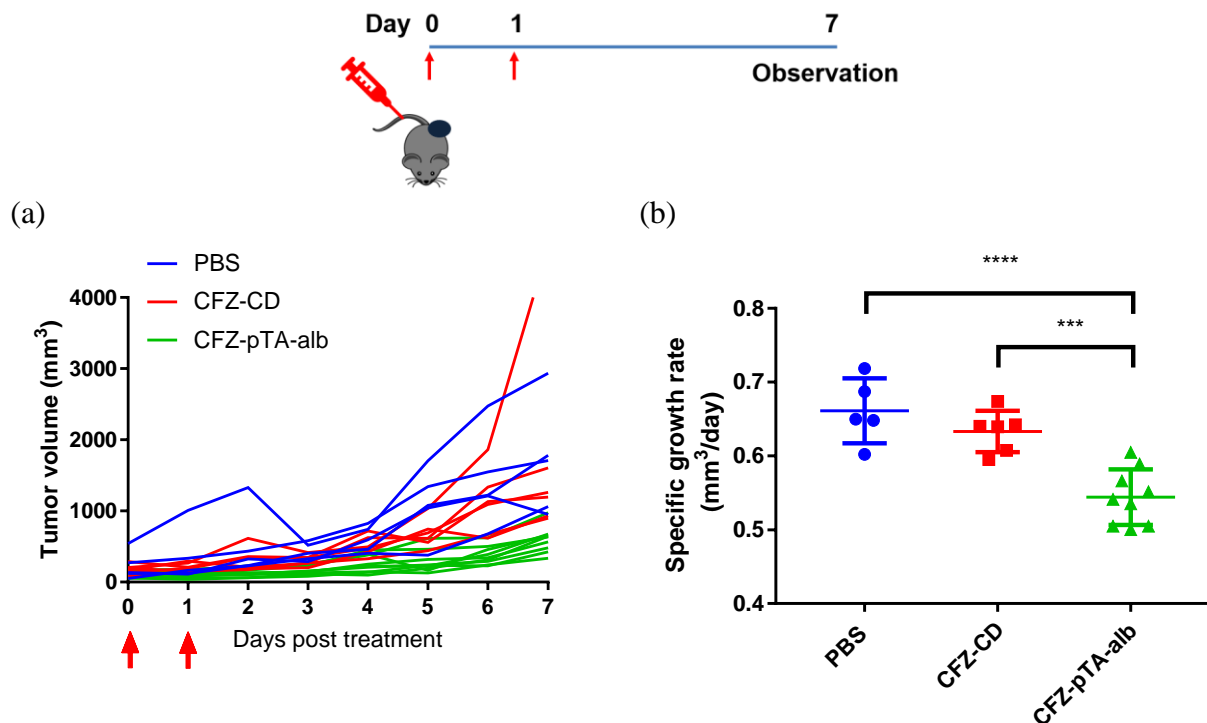


Figure 24: Antitumor activity of CFZ-pTA-alb and CFZ-CD in B16F10@C57BL/6 tumor model after IV injection: (a) Tumor growth curves for individual mice treated with either PBS (n=5), CFZ-CD (n=6) or CFZ-pTA-alb (n=9) at 6 mg/kg of CFZ-equivalent QDx2, and (b) specific tumor growth rate ($\Delta \log V / \Delta t$, V: tumor volume and t: time in days). ***: $p < 0.001$ and ****: $p < 0.0001$, one-way ANOVA with Tukey's multiple comparisons test.

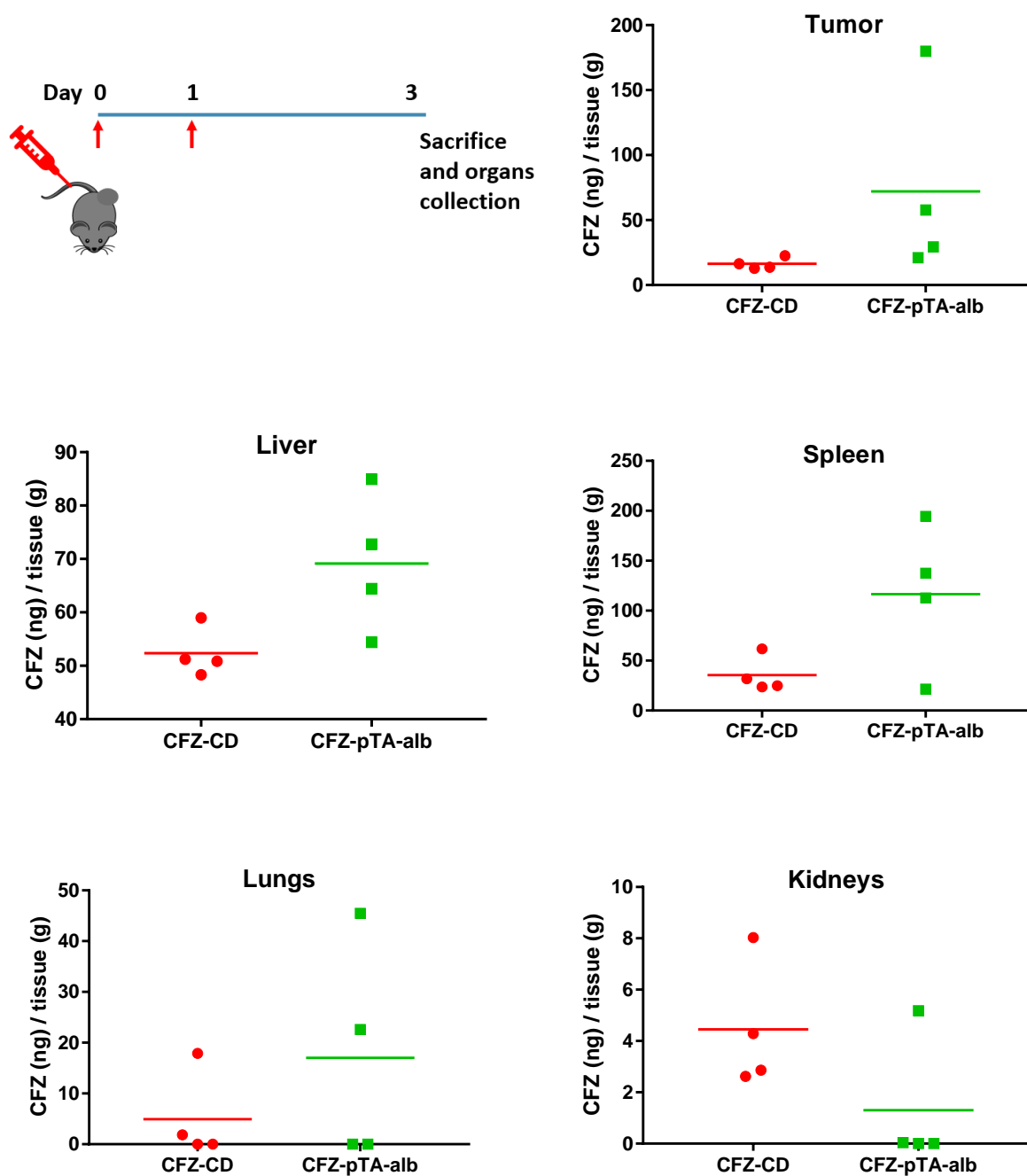


Figure 25: Biodistribution of CFZ in major organs 48 h after 2 consecutive doses of CFZ-CD or CFZ-pTA-alb at a dose equivalent to 6 mg/kg*2 of CFZ in B16F10@C57BL/6 (n=4 mice per group). Quantification done using LC-MS/MS.

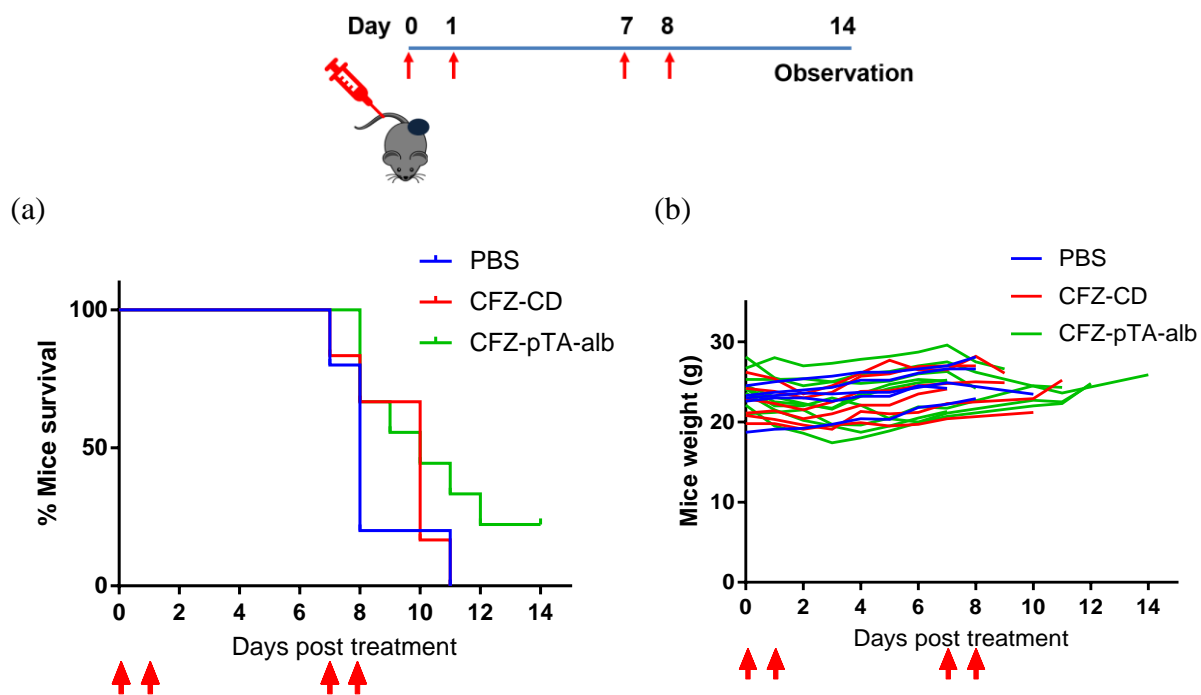


Figure 26: Repeated injections in B16F10@C57BL/6 tumor model. (a) Kaplan–Meier survival curve of mice treated with PBS, CFZ-CD or CFZ-pTA-alb (6 mg/kg CFZ equivalent, QDx2 for 2 weeks), and (b) body weight of treated mice.

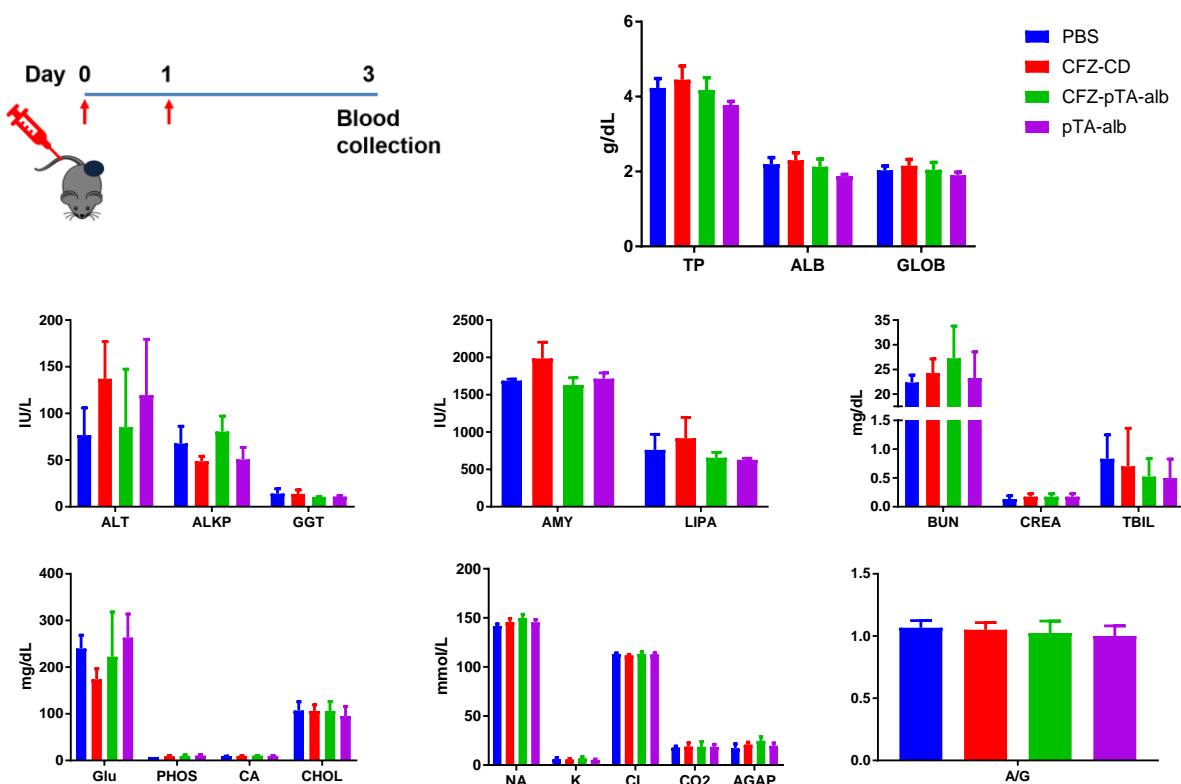


Figure 27: Blood chemistry 48 h after 2 consecutive doses of PBS, CFZ-CD, CFZ-pTA-alb or blank pTA-alb, at a dose equivalent to 6 mg/kg*2 of CFZ in B16F10@C57BL/6 (n=4 mice per group). (TP: total serum protein, ALB: albumin, GLOB: globulin, ALT: alanine transaminase, ALKP: alkaline phosphatase, GGT: gamma-glutamyl transpeptidase, AMY: amylase, LIPA: lipase, BUN: blood urea nitrogen, CREA: creatinine, TBIL: total bilirubin, Glu: glucose, PHOS: phosphate, CA: calcium, CHOL: cholesterol, NA: sodium, K: potassium, CL: chloride, CO2: carbon dioxide, AGAP: anion gap, and A/G: albumin/globulin ratio).

4.3.2 Antitumor effect with localized administration

4.3.2.1 B16F10 tumor model

Next, the IT injection route was utilized as a tool to evaluate the effect of controlled CFZ release on the tumor microenvironment. The antitumor effect of CFZ-pTA-alb was tested in the syngeneic B16F10@C57BL/6 model. Mice with 100 mm³ tumors were injected intratumorally once with PBS, CFZ-CD or CFZ-pTA-alb at a dose equivalent to CFZ 1.2 μg, and tumor volume was monitored for 7 days. CFZ-pTA-alb significantly attenuated tumor growth as indicated by the tumor growth curves (Figure 28a). The specific growth rate values for CFZ-pTA-alb group were significantly lower than both CFZ-CD and PBS groups ($p < 0.05$ and $p < 0.005$, respectively, Tukey's multiple comparisons test) (Figure 28b).

The immunophenotyping of the tumors harvested 7 days after treatment showed a lower percentage of CD8⁺ T cells in CFZ-CD group than those in CFZ-pTA-alb group ($p < 0.05$, Tukey's multiple comparisons test) (Figure 28c). Therefore, the superior antitumor efficacy of CFZ-pTA-alb might be attributable to the sustained release of CFZ from CFZ-pTA-alb, which helped spare tumor infiltrating cytotoxic lymphocytes while efficiently killing tumor cells. To validate this hypothesis, the difference in bolus (high dose for short time) versus sustained (low dose for extended time) cytotoxic effect of CFZ on tumor and immune cells was evaluated. The total exposure, indicated by AUC (area under the curve: dose x exposure time), was kept the same in both regimens (Figure 29a). Bolus regimen was meant to mimic CFZ-CD where the whole dose is freely available to the tumor upon IT injection but would rapidly diffuse to the circulation, and sustained regimen would mimic sustained release of CFZ out of injected CFZ-pTA-alb over time. Spleen cells prepared from freshly harvested C57BL/6 mice spleen were used as a surrogate for immune cells. Being the largest secondary lymphoid organ, spleen is infiltrated with 25% of the body's lymphocytes (Cesta, 2006). The largest immune cell populations in the mouse spleen are B and T cells, being 45-50% and 30-35%, respectively (Invitrogen). B16F10 cells were equally sensitive to CFZ whether applied as bolus or sustained manner (Figure 29b). On the other hand, spleen cells were less sensitive to sustained CFZ exposure than bolus exposure (Figure 29c). These results demonstrate the importance of controlled CFZ release in the tumor microenvironment to maintain the anti-tumor immunity, at least partly, by sparing the tumor infiltrating lymphocytes.

Dendritic cells (DC) play a central role in development of antitumor immunity. DC phagocytose tumor antigens, deliver them to DLNs where they cross-present them to activate cytotoxic lymphocytes. We hypothesized that due to its sticky nature, nanocores capture tumor antigens from dying tumor cells and present them to DC, enhancing the antitumor immune response. To evaluate this, we tested the phagocytosis of B16F10 cells by bone marrow-derived DC (BMDC). B16F10 cells were either non-treated or pretreated with CFZ, CFZ-pTA-alb or blank pTA-alb. Flow cytometry data (Figure 30) shows that pretreatment of B16F10 cells with CFZ formulations significantly increased their uptake by DC. More importantly, CFZ-pTA-alb-treated cells were taken up significantly more than CFZ-treated cells (Figure 30). This result indicates the additional role of the carrier in increasing DC phagocytosis probably by capturing antigens and damage-associated molecular patterns (DAMPs) and delivering them to DC.

The retention of CFZ-CD and CFZ-pTA-alb in the tumor following IT injection was also tested. Both formulations were injected to 100 mm³ tumors at equivalent doses, the mice were sacrificed 2 h later and tumors were harvested for CFZ quantification. CFZ binds irreversibly to its target sites in the proteasome, and this proteasome complex is undetected by LC-MS/MS. Accordingly, the 2 h-timeframe before sacrifice was chosen to allow enough time for free drug drainage but avoid underestimation due to irreversible binding of the drug to its proteasome target. The excised tumors were homogenized and treated with Triton X to destroy CFZ-pTA-alb and allow release of CFZ. Therefore, the quantified CFZ represents the active form of CFZ retained in the tumor, both free and encapsulated within the particles. The amount of CFZ retrieved from CFZ-pTA-alb treated tumors was 3 times higher than that of CFZ-CD group ($p < 0.01$, unpaired two-tailed t -test) (Figure 31a). This result indicates that CFZ-CD initially provided high CFZ dose to the cells followed by rapid clearance (high dose-short exposure). On the other hand, stable CFZ-pTA-alb, retained more in the tumor tissue due to impaired lymphatic drainage, allowed sustained cell exposure to CFZ (low dose-extended exposure). The lower CFZ retention in the tumor, in the CFZ-CD group, corresponded to higher plasma level as well ($p < 0.05$, unpaired two-tailed t -test) (Figure 31b).

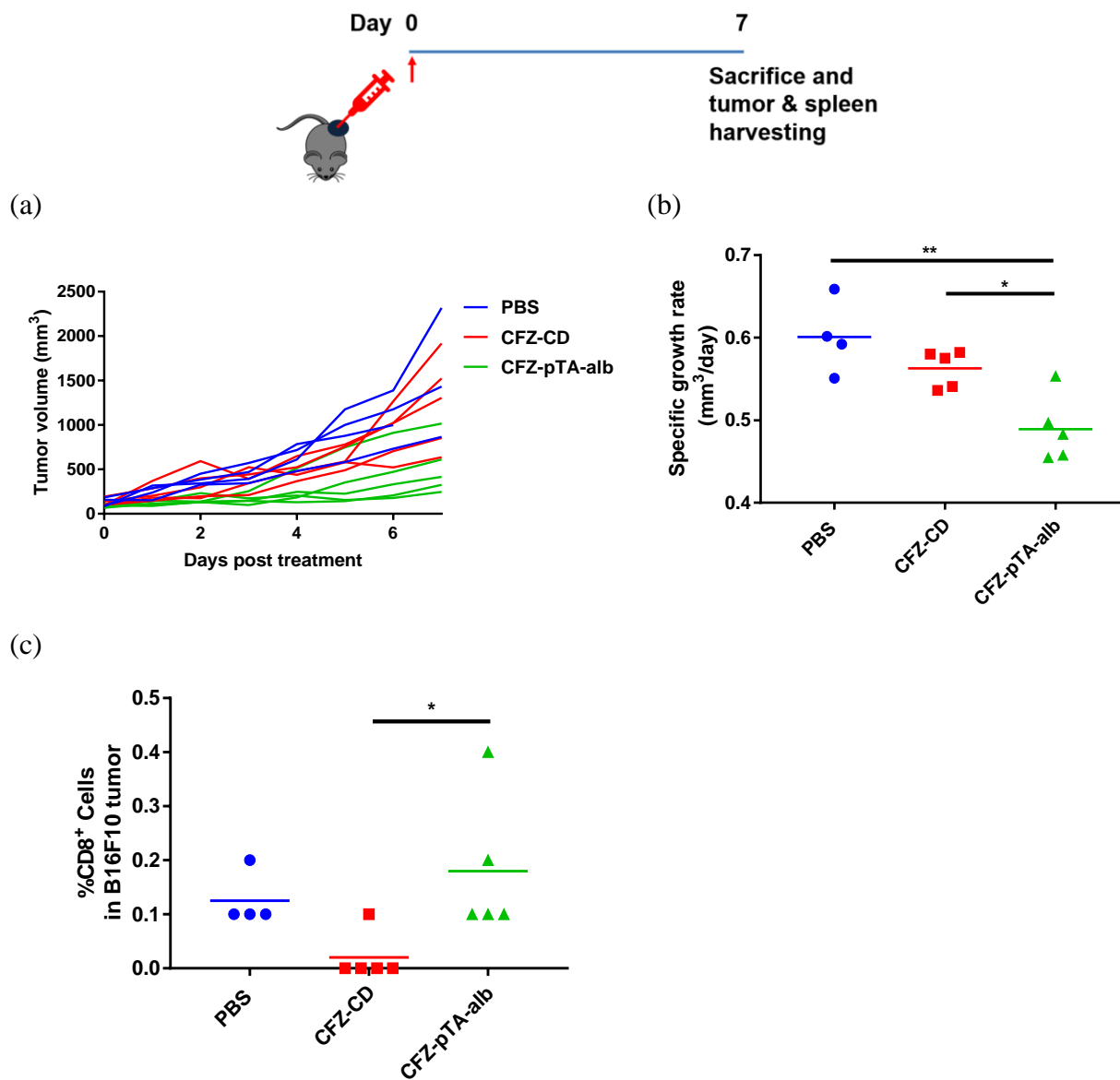


Figure 28: Antitumor activity of CFZ-pTA-alb and CFZ-CD in B16F10@C57BL/6 tumor model after IT injection: (a) Tumor growth curves for individual mice treated once with either PBS (n=4), CFZ-CD (n=5) or CFZ-pTA-alb (n=5) at 1.2 μ g CFZ equivalent, (b) specific growth rate of B16F10 tumor ($\Delta \log V / \Delta t$, V: tumor volume and t: time in days), and (c) quantification of tumor infiltrating CD8⁺ T cells using antibody staining and flow cytometry analysis. *: $p < 0.05$ and **: $p < 0.005$ by one-way ANOVA with Tukey's multiple comparisons test.

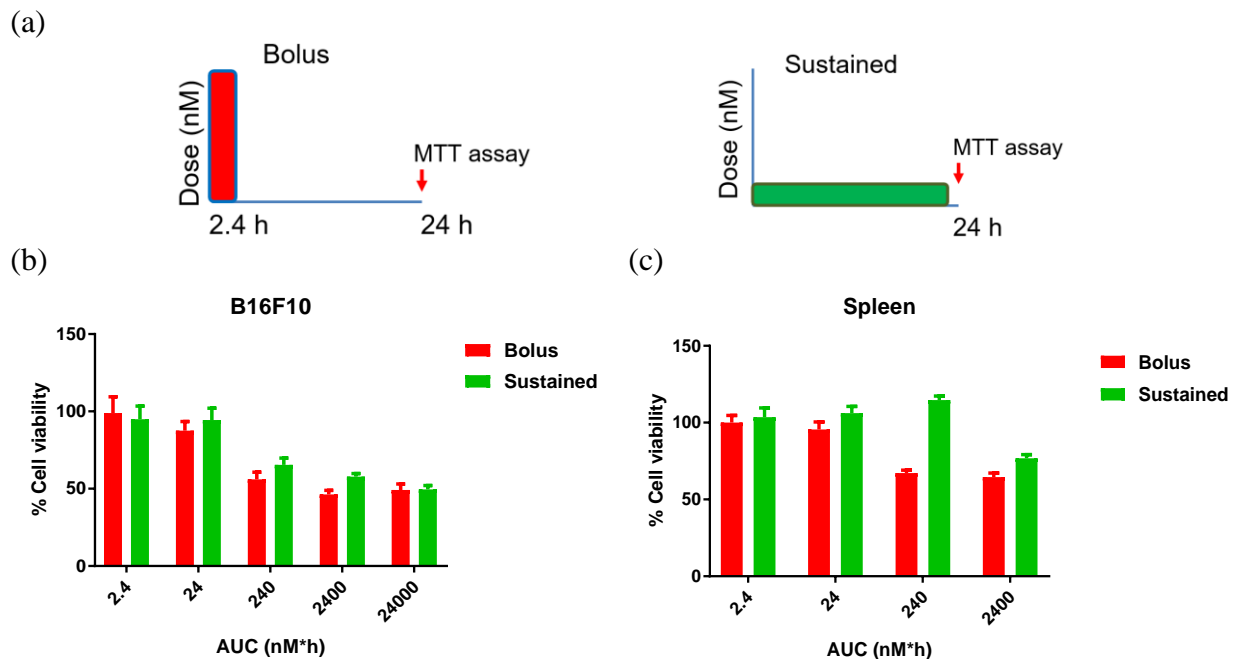


Figure 29: *In vitro* Cytotoxicity of bolus versus sustained CFZ: (a) Schematic for the bolus (cells incubated with different CFZ concentrations for 2.4 h then washed and incubated with drug-free medium for additional 21.6 h) and sustained (cells incubated with different CFZ concentrations for 24 h) exposure regimens, (b) cell viability of B16F10 cells, and (c) cell viability of spleen cells from C57BL/6 mice, after treatment with CFZ (solution in DMSO) in a bolus regimen or sustained regimen. Cell viability measured using MTT assay at the end of 24 h. AUC (area under the curve: dose x exposure time) indicates the total exposure to CFZ over time.

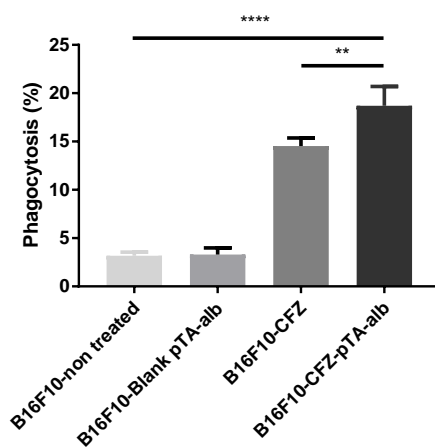


Figure 30: *In vitro* DC phagocytosis: B16F10 cells (DiI-labeled) were either non-treated or treated with blank pTA-alb, CFZ solution or CFZ-pTA-alb (at 10 μ M CFZ equivalent) for 4 h, followed by wash and coculture with BMDCs for 4 h. BMDCs were labeled with APC anti-mouse CD11c antibody and analyzed with flow cytometry. Percentage DC phagocytosis, quantified as the percentage of DiI⁺/CD11c⁺ cells among the CD11c⁺ cells. **: $p < 0.005$ and ****: $p < 0.0001$ by one-way ANOVA with Tukey's multiple comparisons test.

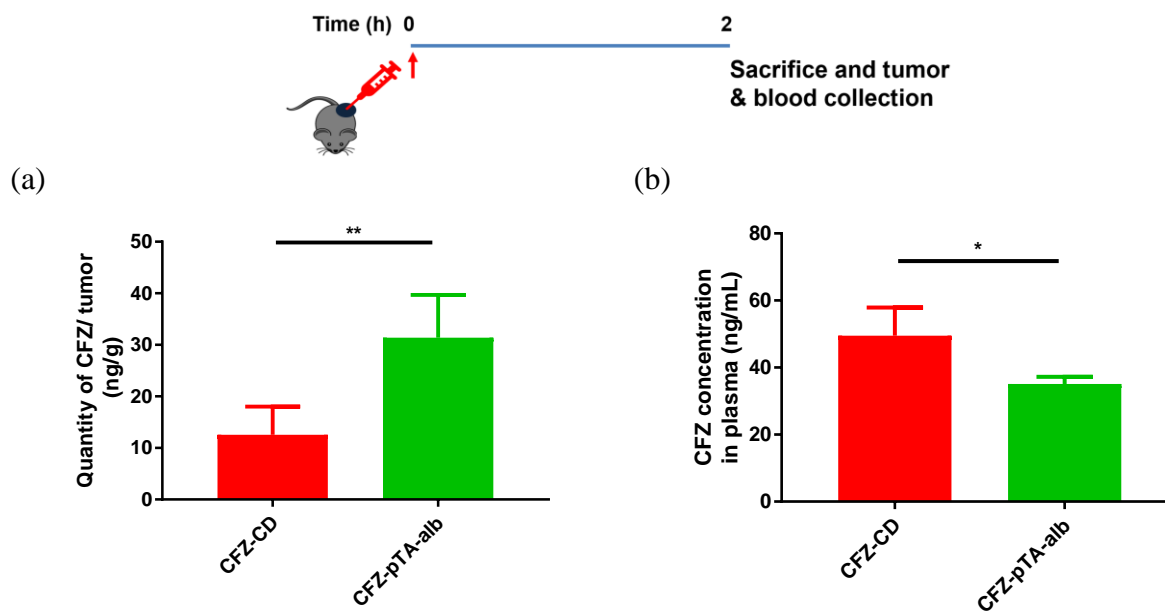


Figure 31: Retention of CFZ formulations in tumor after IT injection: (a) Amount of CFZ in tumor tissue 2 h following IT injection of CFZ-CD (n=4) or CFZ-pTA-alb (n=4) at 1.2 μ g CFZ equivalent, and (b) CFZ concentration in plasma collected at mice sacrifice. Quantification done using LC-MS/MS. *: $p < 0.05$ and **: $p < 0.01$, unpaired two-tailed t -test.

These results demonstrate that locally administered CFZ-pTA-alb attenuates the growth of B16F10 tumors by at least three mechanisms: (i) increasing tumor availability of CFZ (Figure 31), (ii) maintaining CFZ at a subtoxic level to local immune cells (Figure 28c and Figure 29), and (iii) serving as a carrier of tumor antigen to dendritic cells (Figure 30). Based on these observations, we asked if CFZ-pTA-alb was superior to activate cytotoxic T-cells in tumors. To test whether a tumor-specific immunity was developed in the mice upon treatment with different CFZ formulations, spleens were collected 7 days post-treatment for testing antigen-specific T-cell activation. Spleen cells were incubated *in vitro* with irradiated B16F10 cell lysate (tumor antigen) for 72 h, then the supernatants were used to measure IFN- γ production. There was no difference in IFN- γ levels of either CFZ-pTA-alb or CFZ-CD groups from the PBS control group (Figure 32), indicating no tumor antigen-specific immunity attributable to the treatments. This may be due to the fact that B16F10 tumors are poorly immunogenic with few tumor-infiltrating lymphocytes in the first place.

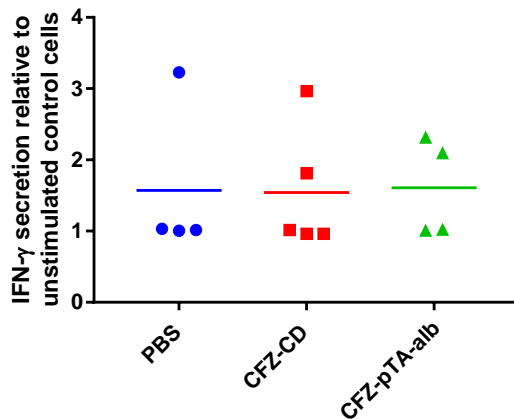


Figure 32: Levels of IFN- γ secretion from splenic T cells upon stimulation with irradiated B16F10 lysate (relative to unstimulated control cells), following single IT injection in B16F10@C57BL/6 tumor model with either PBS (n=4), CFZ-CD (n=5) or CFZ-pTA-alb (n=4) at 1.2 μ g CFZ equivalent.

4.3.2.2 CT26 tumor model

To observe the effect of CFZ-pTA-alb on local immune environment more clearly, we used syngeneic CT26@Balb/c model, which is known for its high immunogenicity and is thus commonly used for evaluation of immune-activating therapies and phenotypic changes in tumor immune microenvironment (Aaes et al., 2016; Baghdadi, Chiba, Yamashina, Yoshiyama, & Jinushi, 2012; Casares et al., 2005; Lechner et al., 2013). CFZ equivalent dose of 1.2 μ g was injected IT in 100 mm³ tumors and tumor volume was monitored for 7 days. Similar to the result obtained with B16F10, CFZ-pTA-alb significantly attenuated tumor growth compared to CFZ-CD and PBS groups ($p < 0.05$ and $p < 0.005$, respectively, Tukey's multiple comparisons test) (Figure 33).

Next, to evaluate whether CFZ-pTA-alb helps establish adaptive immunity to tumors, Balb/c mice were inoculated with CT26 cells in two different sites, where only one tumor (tumor A) was treated with IT injection of PBS or CFZ-pTA-alb at 60 μ g equivalent of CFZ and the other side left untreated. The tumor growth of the untreated tumor (tumor B) was monitored to inform the abscopal effect caused by the treated tumor A. When both tumors were inoculated on the same day (Figure 34a), 6 out of 8 mice had tumor B already when tumor A reached 50 mm³. CFZ-pTA-alb suppressed the growth of tumor A better than PBS (Figure 34b) consistent with previous results.

Tumor B grew rapidly in PBS group, whereas 2 out of 4 mice in CFZ-pTA-alb group showed delayed appearance and growth of tumor B (Figure 34b-d). However, in these 2 mice the onset of tumor B has been delayed from the start of experiment (before the treatment of CFZ-pTA-alb); therefore, it is difficult to judge whether the delay was due to the CFZ-pTA-alb treatment or not. The experiment was repeated with tumor B inoculated 7 days after tumor A inoculation (Figure 35a). Tumor A reaching 50 mm³ was treated with single intratumoral injection of PBS, CFZ-CD or CFZ-pTA-alb at a dose equivalent to CFZ 60 µg. Again, CFZ-pTA-alb significantly attenuated growth of treated tumor (Figure 35b). All mice, including PBS group, did not grow tumor B until the end of the experiment, indicating that concomitant immunity has developed during the growth of tumor A. Since the difference in the extent of immunity could not be judged by the growth of tumor B, splenocytes and DLN were collected from the mice at 22 days post-treatment for ex vivo evaluation of antigen-specific activation. The cells were challenged with AH1 peptide, a CT26 immunodominant MHC class-I restricted antigen (Huang et al., 1996). Splenocytes collected from CFZ-pTA-alb group showed significant IFN-γ secretion upon stimulation with AH1 peptide compared to PBS ($p < 0.05$ vs PBS, Tukey's multiple comparisons test) but those from CFZ-CD-treated animals did not (Figure 35c). However, DLN cells had similar level of IFN-γ secretion in all groups (Figure 35d).

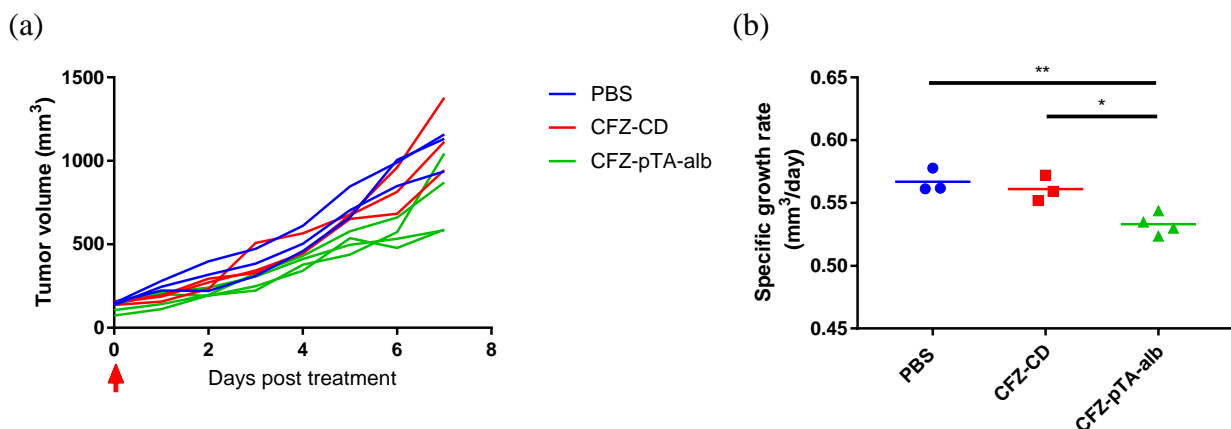


Figure 33: Antitumor activity of CFZ-pTA-alb and CFZ-CD in CT26@Balb/c tumor model after IT injection: (a) Tumor growth curves for individual mice treated once with either PBS (n=3), CFZ-CD (n=3) or CFZ-pTA-alb (n=4) at 1.2 µg CFZ equivalent, and (b) specific growth rate of CT26 tumor ($\Delta \log V / \Delta t$, V: tumor volume and t: time in days). *: $p < 0.05$ and **: $p < 0.005$ by one-way ANOVA with Tukey's multiple comparisons test.

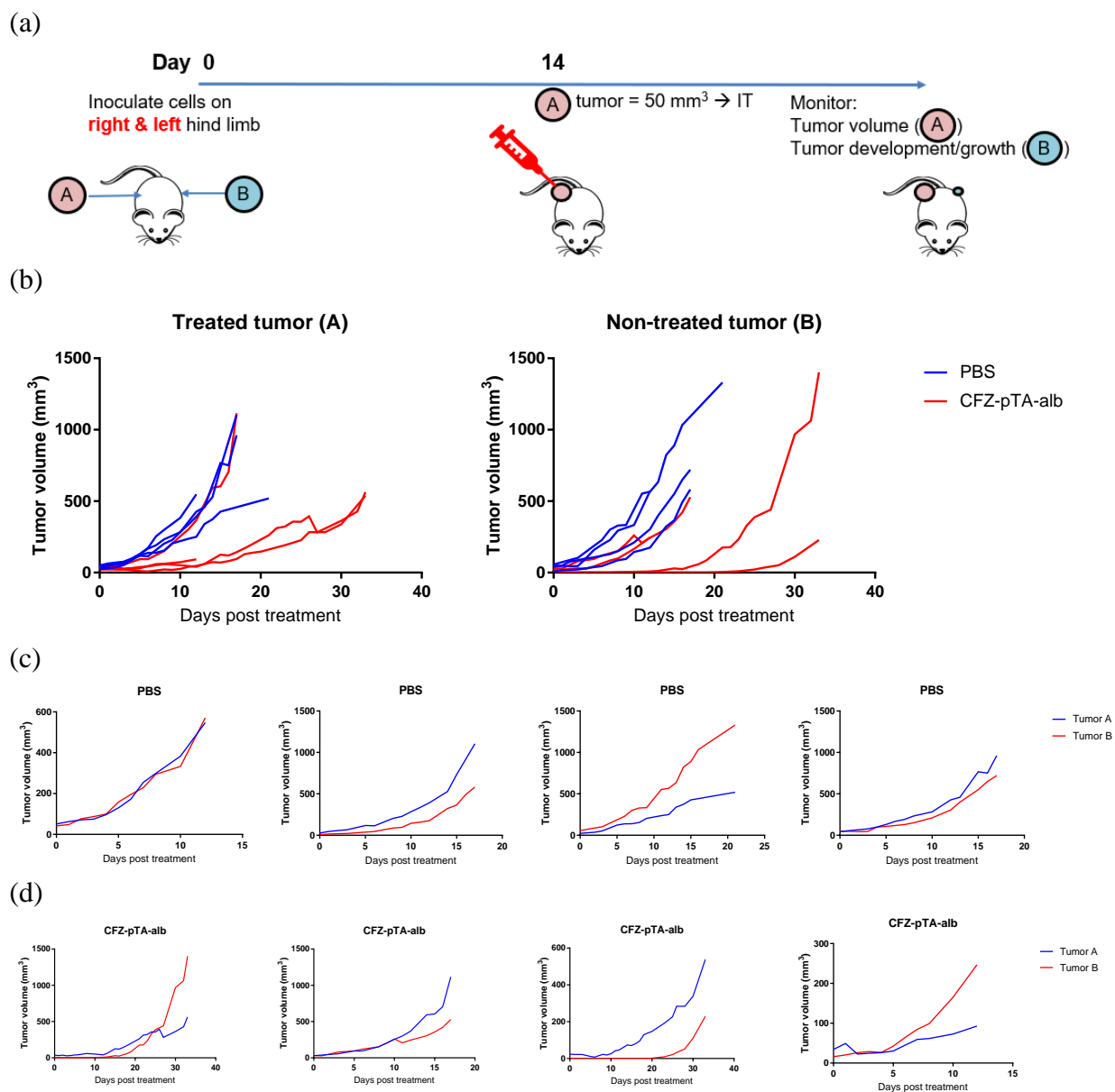


Figure 34: Evaluation of abscopal effect with simultaneous tumor inoculation. (a) Balb/c mice were inoculated with 300,000 and 100,000 CT26 on the right and left hind limb, respectively, on the same day. Right tumors (tumor A) reaching 50 mm³ were treated once with 60 μ g CFZ-equivalent CFZ-pTA-alb or PBS (n=4 per group). (b) Growth curves for treated (tumor A) and non-treated (tumor B) tumors in all mice collectively, and (c and d) individual tumor growth curves for each mouse receiving (c) PBS or (d) CFZ-pTA-alb.

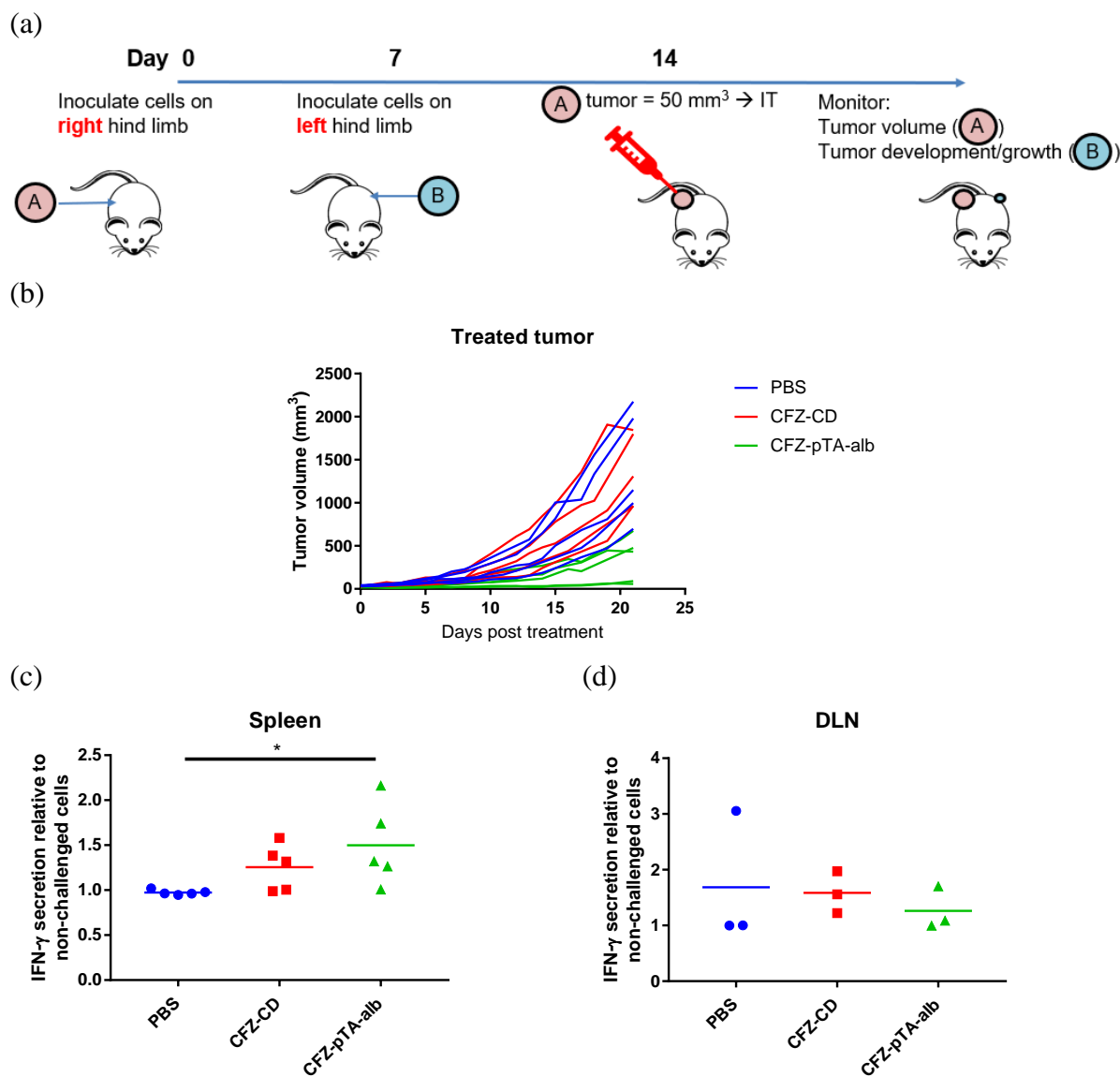


Figure 35: Evaluation of abscopal effect with separated tumor inoculation. (a) Balb/c mice were inoculated with 300,000 CT26 cells on the right hind limb followed by 100,000 CT26 cells on the left hind limb 7 days later. Right tumors (tumor A) reaching 50 mm³ were treated once with 60 μ g CFZ-equivalent CFZ-pTA-alb, CFZ-CD or PBS (n=5 per group). (b) Growth curves for treated (tumor A) tumors. (c and d) Tumor-specific immunity: (c) spleen or (d) DLN cells from mice sacrificed on day 22 post-treatment were challenged with AH1 peptide and IFN- γ secretion was measured using ELISA kit (IFN- γ secretion is presented relative to basal secretion of non-challenged cells). *: $p < 0.05$ by one-way ANOVA with Tukey's multiple comparisons test.

4.3.3 Discussion

CFZ, a second-generation proteasome inhibitor recently approved for MM treatment (Nooka et al., 2013), has not proven effective against solid tumors. The rapid inactivation in blood, via epoxide hydrolysis and cleavage of the peptide backbone, prevents accumulation of active drug at solid tumors sites (Papadopoulos et al., 2013; Yang et al., 2011). Therefore, a NP formulation that can load CFZ with high capacity and protect the drug may make it useful for the therapy of solid tumors. Systemically administered NP are protected from renal clearance owing to their size and have the advantage of greater tumor accumulation than small molecules via the EPR phenomenon (Choi et al., 2007; Matsumura & Maeda, 1986). NP-carried drugs are also protected from metabolizing enzymes in the liver and circulation (Singh & Lillard, 2009).

In previous chapters a CFZ nanocore formulation coated with albumin, CFZ-pTA-alb, was developed. CFZ-pTA-alb loaded CFZ at high capacity, released it in a sustained way and protected it against metabolic degradation *in vitro*. In this chapter we first evaluated if CFZ-pTA-alb would result in better antitumor effect than CFZ-CD upon systemic administration in the B16F10 melanoma model. Compared to CFZ-CD, intravenously injected CFZ-pTA-alb led to slower tumor growth rate over 7 days (Figure 24) and accumulated more CFZ at the tumor site (Figure 25). This is explained by stability of CFZ encapsulation within CFZ-pTA-alb in circulation and thus its protection against degradation, in contrast to CFZ-CD that would rapidly expose CFZ to metabolic degradation and clearance. However, accumulation of CFZ-pTA-alb in RES organs, which is typical for NP, eventually resulted in mice mortality. Therefore, the CFZ stability offered by CFZ-pTA-alb unleashed the CFZ toxicity that was otherwise not observed with the unstable cyclodextrin formulation. Although albumin coating was supposed to have a stealth effect against opsonization, its effect was not sufficient to substantially modify the biodistribution of CFZ-pTA-alb. The amount and conformation of albumin on nanocore surface need to be optimized to improve its stealth effect in future studies. PEG may be used as an alternative stealth coating. It was previously shown that TA coated PLGA NP can be physically coated with PEG. However, despite the long circulation of PEGylated NP, the majority of injected NP is likely to end up in the RES (Li & Huang, 2010; Wilhelm et al., 2016). The PEGylated liposomal doxorubicin formulation had prolonged circulation and enhanced tumor access, yet it accumulated in the liver, spleen and bone marrow (Stewart & Harrington, 1997; Working et al., 1994). However, the difference in potency between doxorubicin and CFZ, as well as the difference in release rate from Doxil® and

CFZ-pTA-alb (which are not studied side-by-side) could be possible reasons for the difference in RES exposure to drug's toxicity.

To capitalize on the stability of CFZ-pTA-alb, we next explored the localized IT injection route. For solid tumors that are easily locatable, IT injection is a viable clinical strategy (Andtbacka et al., 2015). This route is especially attractive for immunotherapy to avoid systemic side effects (Aznar et al., 2017). In addition, recent studies have shown systemic antitumor response with localized IT injections of immunomodulatory drugs (Nuhn et al., 2018; Sagiv-Barfi et al., 2018). ICD inducers injected intratumorally would expose tumor antigens creating *in-situ* patient-specific antitumor vaccines. This personalized immunotherapy approach would result in immune responses against a wide range of tumor antigens epitopes and protect against unreachable metastatic sites. In that regard, CFZ-pTA-alb was hypothesized to serve as an efficient vaccination tool. CFZ has been previously identified as a potential ICD inducer, where it exposes immunogenic markers, namely calreticulin, to the surface of dying apoptotic tumor cells (Jarauta et al., 2016). Immune recognition of the dying tumor cells after IT injection of CFZ, would provide long lasting antitumor adaptive immunity. The sustained release of CFZ at low dose at the tumor site would mimic metronomic chemotherapy with fewer injections. Metronomic chemotherapy refers to the frequent or prolonged administration of chemotherapeutics at much lower doses than those used in MTDs regimens (Kareva et al., 2015). MTDs selectively target chemo-sensitive cancer cells leaving behind chemo-resistant populations that might lead to tumor relapse and emergence of drug resistance (Shah, Rejniak, & Gevertz, 2016). On the contrary, metronomic chemotherapy targets the tumor microenvironment, disengaging the tumor cells from its support system and resulting in long lasting tumor regression. Sustained low doses of chemotherapeutics results in profound antiangiogenic effects (Browder et al., 2000; Klement et al., 2000), activate the antitumor immunity without killing the immune cells recruited to the tumor (Banissi et al., 2009; Ghiringhelli et al., 2007), and avoids the induction of tumor-initiating cancer stem cells (Chan et al., 2016). One study reports that topotecan treated to tumor-endothelial spheroids in fractionated doses, to mimic the metronomic chemotherapy, was more effective in reducing the spheroid size than the bolus dose given once (Jyoti et al., 2015). More interestingly, topotecan encapsulated in a liposomal formulation that offered sustained release rate, was found as effective as the fractionated doses. As an ICD inducer, the antitumor effect of CFZ depends largely on the immune cell population within the tumor, including antigen presenting cells and cytotoxic T cells. The sustained

CFZ release formulation can spare the activity of these cells. In the B16F10 tumor model, CFZ-pTA-alb suppressed tumor growth better than CFZ-CD for 7 days post injection (Figure 28a and b). The superior effect of CFZ-pTA-alb could be attributed to several factors. First, CFZ-pTA-alb nanoparticles displayed better tumor retention after IT injection than the freely diffusing CFZ-CD solution (Figure 31). Second, sustained CFZ release from CFZ-pTA-alb minimizes the killing of chemo-sensitive immune cells that are required for efficient antitumor immune response. This was suggested by the lower percentage of CD8⁺ T cells in tumors harvested from CFZ-CD group than those in CFZ-pTA-alb (Figure 28c). In addition, the *in vitro* cytotoxicity experiment showed the differential toxicity of CFZ to spleen cells (as a surrogate for immune cells) with varying the dosing schedule (Figure 29). The killing effect of sustained low CFZ dose was less than that of a higher bolus dose, at equivalent total exposure. Third, the sticky nanocores capturing dying tumor cells served as antigen-delivery carrier to DC (Figure 30). DC play a central role in development of antitumor immunity. DC phagocytose tumor antigens, deliver them to DLNs where they cross-present them to activate cytotoxic lymphocytes (Hansen & Andersen, 2017). Therefore, enhanced DC phagocytosis of tumor antigens enabled by nanocores may have played a role in the observed antitumor effect.

Although the above results suggest more active local immune activity in B16F10 tumors treated with CFZ-pTA-alb than those with CFZ-CD, the splenocytes harvested from different treatment groups showed no appreciable difference in IFN- γ production in response to B16F10 lysate. Reasons for this result could be the suboptimal dose of CFZ-pTA-alb that did not create enough tumor antigens for immune activation and the poor immunogenicity of the tumor model. B16F10 is usually reported as a poorly immunogenic, or cold tumor, and thus capable of evading the immune system (Xu et al., 2004). This poor immunogenicity was attributed to the low expression of MHC antigens and costimulatory molecules essential for immune activation (Seliger, Wollscheid, Momburg, Blankenstein, & Huber, 2001; Wang, Saffold, Cao, Krauss, & Chen, 1998). Even irradiated B16F10 cells did not generate antitumor immunity in mice (Wang et al., 1998). Accumulation of CD4⁺ regulatory (Treg) cells in B16F10 was reported, and upon depletion of intratumoral CD4⁺ cells, tumor infiltration of CD8⁺ and NK cells significantly increased resulting in enhanced antitumor responses (Fujiwara et al., 2014; von Scheidt, Möller, Smyth, & Teng, 2013).

Therefore, to vaccinate mice by creating tumor antigens *in-situ*, the CT26 colon carcinoma model was utilized. This tumor model is known for its high immunogenicity and is thus commonly used for evaluation of immune-activating therapies and phenotypic changes in tumor immune microenvironment (Aaes et al., 2016; Baghdadi et al., 2012; Casares et al., 2005; Lechner et al., 2013). In the CT26 model, long-lasting tumor-specific immunity was detected 22 days after intratumoral injection of CFZ-pTA-alb (Figure 35c), evidenced by increased IFN- γ production from spleen cells of CFZ-pTA-alb-treated CT26-bearing mice upon stimulation *in vitro* with AH1 peptide, the CT26 immunodominant MHC class-I restricted antigen (Huang et al., 1996). The abscopal effect was not directly observed in this model due to concomitant immunity phenomenon, where mice bearing a first tumor will reject a second tumor challenge even in absence of treatment (Lin et al., 2009).

4.3.4 Conclusions

In a syngeneic model of B16F10 melanoma, intravenously administered CFZ-pTA-alb enhanced biodistribution of CFZ in tumor and antitumor effect as compared to CFZ-CD due to the increased stability. Repeated IV injections of CFZ-pTA-alb exposed the mice to CFZ toxicity that was not observed with the unstable CFZ-CD formulation. Therefore, further modification of the nanocore surface is required to decrease the RES uptake. Intratumorally administered CFZ-pTA-alb attenuated tumor growth better than CFZ-CD in B16F10 and CT26 tumor models, potentially by increased tumor retention, sparing tumor infiltrating lymphocytes and delivering tumor antigens to DCs. Intratumorally administered CFZ-pTA-alb generated a long-lasting systemic antitumor immunity.

4.3.5 References

- Aaes, Tania L., Kaczmarek, A., Delvaeye, T., De Craene, B., De Koker, S., Heyndrickx, L., . . . Krysko, Dmitri V. (2016). Vaccination with Necroptotic Cancer Cells Induces Efficient Anti-tumor Immunity. *Cell Reports*, 15(2), 274-287. doi: <https://doi.org/10.1016/j.celrep.2016.03.037>
- Andtbacka, R. H. I., Kaufman, H. L., Collichio, F., Amatruda, T., Senzer, N., Chesney, J., . . . Coffin, R. S. (2015). Talimogene Laherparepvec Improves Durable Response Rate in Patients With Advanced Melanoma. *Journal of Clinical Oncology*, 33(25), 2780-2788. doi: 10.1200/jco.2014.58.3377
- Aznar, M. A., Tinari, N., Rullán, A. J., Sánchez-Paulete, A. R., Rodriguez-Ruiz, M. E., & Melero, I. (2017). Intratumoral Delivery of Immunotherapy—Act Locally, Think Globally. *The Journal of Immunology*, 198(1), 31. doi: 10.4049/jimmunol.1601145
- Baghdadi, M., Chiba, S., Yamashina, T., Yoshiyama, H., & Jinushi, M. (2012). MFG-E8 regulates the immunogenic potential of dendritic cells primed with necrotic cell-mediated inflammatory signals. *PLoS ONE*, 7(6), e39607-e39607. doi: 10.1371/journal.pone.0039607
- Banissi, C., Ghiringhelli, F., Chen, L., & Carpentier, A. F. (2009). Treg depletion with a low-dose metronomic temozolomide regimen in a rat glioma model. *Cancer Immunology, Immunotherapy*, 58(10), 1627-1634. doi: 10.1007/s00262-009-0671-1
- Browder, T., Butterfield, C. E., Kräling, B. M., Shi, B., Marshall, B., O'Reilly, M. S., & Folkman, J. (2000). Antiangiogenic Scheduling of Chemotherapy Improves Efficacy against Experimental Drug-resistant Cancer. *Cancer Research*, 60(7), 1878.
- Casares, N., Pequignot, M. O., Tesniere, A., Ghiringhelli, F., Roux, S., Chaput, N., . . . Kroemer, G. (2005). Caspase-dependent immunogenicity of doxorubicin-induced tumor cell death. *The Journal of experimental medicine*, 202(12), 1691. doi: 10.1084/jem.20050915
- Cesta, M. F. (2006). Normal structure, function, and histology of the spleen. [Research Support, N.I.H., Extramural Review]. *Toxicol Pathol*, 34(5), 455-465. doi: 10.1080/01926230600867743
- Chan, T.-S., Hsu, C.-C., Pai, V. C., Liao, W.-Y., Huang, S.-S., Tan, K.-T., . . . Tsai, K. K. (2016). Metronomic chemotherapy prevents therapy-induced stromal activation and induction of tumor-initiating cells. *The Journal of experimental medicine*, 213(13), 2967-2988. doi: 10.1084/jem.20151665
- Choi, H. S., Liu, W., Misra, P., Tanaka, E., Zimmer, J. P., Ipe, B. I., . . . Frangioni, J. V. (2007). Renal Clearance of Nanoparticles. *Nature biotechnology*, 25(10), 1165-1170. doi: 10.1038/nbt1340
- Corazzari, M., Gagliardi, M., Fimia, G. M., & Pientini, M. (2017). Endoplasmic Reticulum Stress, Unfolded Protein Response, and Cancer Cell Fate. *Frontiers in oncology*, 7, 78-78. doi: 10.3389/fonc.2017.00078
- Fujiwara, S., Nagai, H., Shimoura, N., Oniki, S., Yoshimoto, T., & Nishigori, C. (2014). Intratumoral CD4+ T Lymphodepletion Sensitizes Poorly Immunogenic Melanomas to Immunotherapy with an OX40 Agonist. *Journal of Investigative Dermatology*, 134(7), 1884-1892. doi: <https://doi.org/10.1038/jid.2014.42>
- Ghiringhelli, F., Menard, C., Puig, P. E., Ladoire, S., Roux, S., Martin, F., . . . Chauffert, B. (2007). Metronomic cyclophosphamide regimen selectively depletes CD4+CD25+ regulatory T cells and restores T and NK effector functions in end stage cancer patients. *Cancer Immunology, Immunotherapy*, 56(5), 641-648. doi: 10.1007/s00262-006-0225-8

- Hansen, M., & Andersen, M. H. (2017). The role of dendritic cells in cancer. *Seminars in Immunopathology*, 39(3), 307-316. doi: 10.1007/s00281-016-0592-y
- Huang, A. Y., Gulden, P. H., Woods, A. S., Thomas, M. C., Tong, C. D., Wang, W., . . . Jaffee, E. M. (1996). The immunodominant major histocompatibility complex class I-restricted antigen of a murine colon tumor derives from an endogenous retroviral gene product. *Proceedings of the National Academy of Sciences of the United States of America*, 93(18), 9730-9735.
- Invitrogen. Cell concentrations in human and mouse samples, from https://assets.thermofisher.com/TFS-Assets/LSG/brochures/I-076357%20cell%20count%20table%20topp_WEB.pdf
- Jakubowiak, A. J. (2014). Evolution of carfilzomib dose and schedule in patients with multiple myeloma: a historical overview. [Review]. *Cancer Treat Rev*, 40(6), 781-790. doi: 10.1016/j.ctrv.2014.02.005
- Jarauta, V., Jaime, P., Gonzalo, O., de Miguel, D., Ramírez-Labrada, A., Martínez-Lostao, L., . . . Naval, J. (2016). Inhibition of autophagy with chloroquine potentiates carfilzomib-induced apoptosis in myeloma cells in vitro and in vivo. *Cancer letters*, 382(1), 1-10. doi: <https://doi.org/10.1016/j.canlet.2016.08.019>
- Jyoti, A., Fugit, K. D., Sethi, P., McGarry, R. C., Anderson, B. D., & Upreti, M. (2015). An in vitro assessment of liposomal topotecan simulating metronomic chemotherapy in combination with radiation in tumor-endothelial spheroids. *Scientific Reports*, 5, 15236-15236. doi: 10.1038/srep15236
- Kareva, I., Waxman, D. J., & Lakka Klement, G. (2015). Metronomic chemotherapy: an attractive alternative to maximum tolerated dose therapy that can activate anti-tumor immunity and minimize therapeutic resistance. *Cancer letters*, 358(2), 100-106. doi: 10.1016/j.canlet.2014.12.039
- Klement, G., Baruchel, S., Rak, J., Man, S., Clark, K., Hicklin, D. J., . . . Kerbel, R. S. (2000). Continuous low-dose therapy with vinblastine and VEGF receptor-2 antibody induces sustained tumor regression without overt toxicity. [Research Support, Non-U S Gov't Research Support, U S Gov't, P H S]. *J Clin Invest*, 105(8).
- Lechner, M. G., Karimi, S. S., Barry-Holson, K., Angell, T. E., Murphy, K. A., Church, C. H., . . . Epstein, A. L. (2013). Immunogenicity of murine solid tumor models as a defining feature of in vivo behavior and response to immunotherapy. *Journal of immunotherapy* (Hagerstown, Md. : 1997), 36(9), 477-489. doi: 10.1097/01.cji.0000436722.46675.4a
- Lee, A. H., Iwakoshi, N. N., Anderson, K. C., & Glimcher, L. H. (2003). Proteasome inhibitors disrupt the unfolded protein response in myeloma cells. [Research Support, Non-U.S. Gov't Research Support, U.S. Gov't, P.H.S.]. *Proc Natl Acad Sci U S A*, 100(17), 9946-9951. doi: 10.1073/pnas.1334037100
- Li, S.-D., & Huang, L. (2010). Stealth Nanoparticles: High Density but Sheddable PEG is a Key for Tumor Targeting. *Journal of controlled release : official journal of the Controlled Release Society*, 145(3), 178-181. doi: 10.1016/j.jconrel.2010.03.016
- Lin, Y.-C., Chang, L.-Y., Huang, C.-T., Peng, H.-M., Dutta, A., Chen, T.-C., . . . Lin, C.-Y. (2009). Effector/Memory but Not Naive Regulatory T Cells Are Responsible for the Loss of Concomitant Tumor Immunity. *The Journal of Immunology*, 182(10), 6095. doi: 10.4049/jimmunol.0803829

- Matsumura, Y., & Maeda, H. (1986). A New Concept for Macromolecular Therapeutics in Cancer Chemotherapy: Mechanism of Tumor-tropic Accumulation of Proteins and the Antitumor Agent Smancs. *Cancer Research*, 46(12 Part 1), 6387.
- Mehta, A., Zhang, L., Boufraqueh, M., Zhang, Y., Patel, D., Shen, M., & Kebebew, E. (2015). Carfilzomib is an effective anticancer agent in anaplastic thyroid cancer. [Research Support, N I H , Intramural]. *Endocr Relat Cancer*, 22(3), 319-329.
- Nooka, A., Gleason, C., Casbourne, D., & Lonial, S. (2013). Relapsed and refractory lymphoid neoplasms and multiple myeloma with a focus on carfilzomib. *Biologics : Targets & Therapy*, 7, 13-32. doi: 10.2147/btt.s24580
- Nuhn, L., De Koker, S., Van Lint, S., Zhong, Z., Catani, J. P., Combes, F., . . . De Geest, B. G. (2018). Nanoparticle-Conjugate TLR7/8 Agonist Localized Immunotherapy Provokes Safe Antitumoral Responses. *Advanced Materials*, 30(45), 1803397. doi: 10.1002/adma.201803397
- Papadopoulos, K. P., Burris, H. A., Gordon, M., Lee, P., Sausville, E. A., Rosen, P. J., . . . Infante, J. R. (2013). A phase I/II study of carfilzomib 2–10-min infusion in patients with advanced solid tumors. *Cancer Chemotherapy and Pharmacology*, 72(4), 861-868. doi: 10.1007/s00280-013-2267-x
- Sagiv-Barfi, I., Czerwinski, D. K., Levy, S., Alam, I. S., Mayer, A. T., Gambhir, S. S., & Levy, R. (2018). Eradication of spontaneous malignancy by local immunotherapy. *Science Translational Medicine*, 10(426), eaan4488. doi: 10.1126/scitranslmed.aan4488
- Seliger, B., Wollscheid, U., Momburg, F., Blankenstein, T., & Huber, C. (2001). Characterization of the Major Histocompatibility Complex Class I Deficiencies in B16 Melanoma Cells. *Cancer Research*, 61(3), 1095.
- Shah, A. B., Rejniak, K. A., & Gevertz, J. L. (2016). Limiting the development of anti-cancer drug resistance in a spatial model of micrometastases. *Mathematical biosciences and engineering : MBE*, 13(6), 1185-1206. doi: 10.3934/mbe.2016038
- Singh, R., & Lillard, J. W. (2009). Nanoparticle-based targeted drug delivery. *Experimental and molecular pathology*, 86(3), 215-223. doi: 10.1016/j.yexmp.2008.12.004
- Stewart, S., & Harrington, K. J. (1997). The Biodistribution and Pharmacokinetics of Stealth Liposomes in Patients with Solid Tumors. *Oncology*, 11(10), 33-37.
- Tang, A. C., Rahavi, S. M., Fung, S.-Y., Lu, H. Y., Yang, H., Lim, C. J., . . . Turvey, S. E. (2018). Combination therapy with proteasome inhibitors and TLR agonists enhances tumour cell death and IL-1 β production. *Cell Death & Disease*, 9(2), 162. doi: 10.1038/s41419-017-0194-1
- von Scheidt, B., Möller, A., Smyth, M. J., & Teng, M. W. L. (2013). The interaction between murine melanoma and the immune system reveals that prolonged responses predispose for autoimmunity AU - Ngiow, Shin Foong. *OncoImmunology*, 2(2), e23036. doi: 10.4161/onci.23036
- Wang, J., Saffold, S., Cao, X., Krauss, J., & Chen, W. (1998). Eliciting T Cell Immunity Against Poorly Immunogenic Tumors by Immunization with Dendritic Cell-Tumor Fusion Vaccines. *The Journal of Immunology*, 161(10), 5516.
- Wilhelm, S., Tavares, A. J., Dai, Q., Ohta, S., Audet, J., Dvorak, H. F., & Chan, W. C. W. (2016). Analysis of nanoparticle delivery to tumours. [Perspective]. *Nature Reviews Materials*, 1, 16014. doi: 10.1038/natrevmats.2016.14

- Working, P. K., Newman, M. S., Huang, S. K., Mayhew, E., Vaage, J., & Lasic, D. D. (1994). Pharmacokinetics, Biodistribution and Therapeutic Efficacy of Doxorubicin Encapsulated in Stealth® Liposomes (Doxil®). *Journal of Liposome Research*, 4(1), 667-687. doi: 10.3109/08982109409037065
- Xu, D., Gu, P., Pan, P.-Y., Li, Q., Sato, A. I., & Chen, S.-H. (2004). NK and CD8+ T cell-mediated eradication of poorly immunogenic B16-F10 melanoma by the combined action of IL-12 gene therapy and 4-1BB costimulation. *International Journal of Cancer*, 109(4), 499-506. doi: 10.1002/ijc.11696
- Yang, J., Wang, Z., Fang, Y., Jiang, J., Zhao, F., Wong, H., . . . Kirk, C. J. (2011). Pharmacokinetics, Pharmacodynamics, Metabolism, Distribution, and Excretion of Carfilzomib in Rats. [10.1124/dmd.111.039164]. *Drug Metabolism and Disposition*, 39(10), 1873.

CHAPTER 5. CONCLUSION

5.1 Summary

The preparation of nanocore formulations stabilized with TA/Fe³⁺ interfacial assemblies has been optimized using different drugs. TA/Fe³⁺ interfacial assemblies successfully coated drug nuclei to form stabilized spherical nanocores. The nanocores had high drug loading capacity and loaded 2 drugs in a controllable ratio. The TA/Fe³⁺ assemblies efficiently covered the drug in the core to avoid Ostwald ripening and prevent aggregation.

The ability of TA/Fe³⁺ assemblies stabilizing the surface of nanocores to interact with ligands was explored. Three surface functionalization were pursued: a nucleic acid (pDNA), a quinic acid derivative (QA), and albumin. The nanocore surface was successfully decorated by the three ligands, and their functionality was evaluated. The pDNA-bound nanocore did not transfect NCI/ADR-RES, potentially due to inefficient cell uptake, irreversible binding between TA and pDNA, and /or very slow intracellular pDNA release. The QA-bound nanocores did not specifically bind to E-selectin, possibly due to insufficient QA density on the surface, weak binding affinity of QA to the nanocore surface and/or unavailability of QA hydroxyl groups for efficient E-selectin binding. Albumin coat on CFZ nanocores (CFZ-pTA-alb) provided a barrier to CFZ release and protection against metabolic degradation.

In a syngeneic model of B16F10 melanoma, intravenously administered CFZ-pTA-alb enhanced biodistribution of CFZ in tumor and antitumor effect as compared to CFZ cyclodextrin-based solution (CFZ-CD) due to the increased stability. Repeated intravenous injections of CFZ-pTA-alb exposed the mice to CFZ toxicity that was not observed with the unstable CFZ-CD formulation. Therefore, further modification of the nanocore surface is required to decrease the RES uptake. Intratumorally administered CFZ-pTA-alb attenuated tumor growth better than CFZ-CD in B16F10 and CT26 tumor models and generated a long-lasting systemic antitumor immunity. This superior effect is potentially by increased tumor retention, sparing tumor infiltrating lymphocytes and delivering tumor antigens to DCs.

5.2 Future studies

To reduce the RES uptake of the nanocores and avoid systemic toxicity, surface functionalization with other ligands need to be pursued. Examples of stealth polymers include PEG, polyoxazolines, poly(amino acids), polybetaines and polysaccharides (Amoozgar & Yeo, 2012).

The nanocore formulation can be utilized to co-deliver CFZ with immune check point inhibitor to combine immunogenic cell death with immune checkpoint blockade.

The antiangiogenic effect of sustained CFZ nanocore formulation will be studied. The antiangiogenic effect of bortezomib (a first-generation proteasome inhibitor) has been reported, where it induces endothelial cell apoptosis and downregulates vascular endothelial cell growth factor (VEGF) interleukin-6 (IL-6), insulin-like growth factor-I (IGF-I), angiopoietin 1 (Ang1) and angiopoietin 2 (Ang2), which are required for angiogenic phenotype in endothelial cells (Roccaro et al., 2006; Williams et al., 2003). The antiangiogenic effect of oprozomib (orally bioavailable CFZ analog) was also reported (Sanchez et al., 2017). Accordingly, CFZ is assumed to possess similar antiangiogenic effects, which would manifest better with less toxicity to the immune microenvironment with the sustained metronomic dosing.

The role of the carrier in the antitumor activity of CFZ-pTA-alb also needs to be studied. TA was proved to inhibit the CXCL12/CXCR4 interaction, suppressing tumor cell migration and angiogenesis (Chen et al., 2003). In glioma Hs683 cells, TA increased intracellular reactive oxygen species production and resulted in cell apoptosis in a dose dependent manner (Zhang et al., 2018). TA has also shown potent inhibition of proteasome chymotrypsin-like activity in tumor cells, in a mechanism similar to CFZ, and this was attributed to the ester bond in its structure (Chang & Wang, 2013; Nam, Smith, & Dou, 2001a, 2001b). The apoptotic tumor cell death induced by TA suggests its ICD induction ability. A study on the gallotannin-rich fraction separated from *Caesalpinia spinosa* plant extract has shown to induce ICD markers *in vitro* (Urueña et al., 2015). In addition, 4T1 tumor cells treated with this fraction successfully vaccinated mice resulting in long-lasting tumor-specific immune response and delayed tumor growth. TA hydrogen bonded with poly (N-vinylpyrrolidone) was previously used to form microparticles that encapsulated tumor antigens and generated adaptive immunity via dendritic cell activation (Dierendonck et al., 2014); however, the role of TA in dendritic cells activation has not been studied.

5.3 References

- Amoozgar, Z., & Yeo, Y. (2012). Recent advances in stealth coating of nanoparticle drug delivery systems. *Wiley Interdisciplinary Reviews. Nanomedicine and Nanobiotechnology*, 4(2), 219-233. doi: 10.1002/wnan.1157
- Chang, T.-L., & Wang, C.-H. (2013). Combination of quercetin and tannic acid in inhibiting 26S proteasome affects S5a and 20S expression, and accumulation of ubiquitin resulted in apoptosis in cancer chemoprevention *Biological Chemistry* (Vol. 394, pp. 561).
- Chen, X., Beutler, J. A., McCloud, T. G., Loehfelm, A., Yang, L., Dong, H.-F., . . . Howard, O. M. Z. (2003). Tannic Acid Is an Inhibitor of CXCL12 (SDF-1 α)/CXCR4 with Antiangiogenic Activity. *Clinical Cancer Research*, 9(8), 3115.
- Dierendonck, M., Fierens, K., De Rycke, R., Lybaert, L., Maji, S., Zhang, Z., . . . De Geest, B. G. (2014). Nanoporous Hydrogen Bonded Polymeric Microparticles: Facile and Economic Production of Cross Presentation Promoting Vaccine Carriers. *Advanced Functional Materials*, 24(29), 4634-4644. doi: 10.1002/adfm.201400763
- Nam, S., Smith, D. M., & Dou, Q. P. (2001a). Ester Bond-containing Tea Polyphenols Potently Inhibit Proteasome Activity in Vitro and in Vivo. *Journal of Biological Chemistry*, 276(16), 13322-13330. doi: 10.1074/jbc.M004209200
- Nam, S., Smith, D. M., & Dou, Q. P. (2001b). Tannic Acid Potently Inhibits Tumor Cell Proteasome Activity, Increases p27 and Bax Expression, and Induces G₂M Arrest and Apoptosis. *Cancer Epidemiology Biomarkers & Prevention*, 10(10), 1083.
- Roccaro, A. M., Hideshima, T., Raje, N., Kumar, S., Ishitsuka, K., Yasui, H., . . . Anderson, K. C. (2006). Bortezomib Mediates Antiangiogenesis in Multiple Myeloma via Direct and Indirect Effects on Endothelial Cells. *Cancer Research*, 66(1), 184. doi: 10.1158/0008-5472.can-05-1195
- Sanchez, E., Li, M., Wang, C. S., Tang, G., Gillespie, A., Chen, H., & Berenson, J. R. (2017). Anti-angiogenic and anti-multiple myeloma effects of oprozomib (OPZ) alone and in combination with pomalidomide (Pom) and/or dexamethasone (Dex). *Leukemia Research*, 57, 45-54. doi: <https://doi.org/10.1016/j.leukres.2017.03.002>
- Urueña, C., Gomez, A., Sandoval, T., Hernandez, J., Li, S., Barreto, A., & Fiorentino, S. (2015). Multifunctional T Lymphocytes Generated After Therapy With an Antitumor Gallotanin-Rich Normalized Fraction Are Related to Primary Tumor Size Reduction in a Breast Cancer Model. *Integrative Cancer Therapies*, 14(5), 468-483. doi: 10.1177/1534735415596425
- Williams, S., Pettaway, C., Song, R., Papandreou, C., Logothetis, C., & McConkey, D. J. (2003). Differential effects of the proteasome inhibitor bortezomib on apoptosis and angiogenesis in human prostate tumor xenografts. *Molecular Cancer Therapeutics*, 2(9), 835.
- Zhang, J., Chen, D., Han, D.-M., Cheng, Y.-H., Dai, C., Wu, X.-J., . . . Heng, X.-Y. (2018). Tannic acid mediated induction of apoptosis in human glioma Hs 683 cells. *Oncology letters*, 15(5), 6845-6850. doi: 10.3892/ol.2018.8197

VITA

Maie Taha was born in Giza, a city located on the west bank of the Nile, southwest of central Cairo, Egypt. She received her B.Sc. degree in Pharmaceutical Sciences from Cairo University in 2008, ranking the 1st in her class. After graduation, she worked as a teaching and research assistant for six years in Department of Pharmaceutics in the same University. She earned her M.Sc. degree in Pharmaceutics in 2013 with a research focused on developing new bucco-adhesive formulations to enhance the bioavailability of extensively metabolized drugs.

Based on the excellence of her work, she received a full Ph.D. fellowship from the Egyptian Ministry of Higher Education in 2014. In January 2015, Maie joined Dr. Yeon Yeo's lab in the Department of Industrial and Physical Pharmacy, College of Pharmacy, Purdue University to pursue her Ph.D. degree. During her Ph.D. she has performed research on developing nanoparticle formulations for enhanced tumor drug delivery. Her time at Purdue University has trained her to become a competent and strong-minded scientist. With completion of her Ph.D., Maie intends to continue her research career as a post-doctoral research associate, after which she will accept an Assistant Professor position in the Department of Pharmaceutics, Faculty of Pharmacy, Cairo University.

PUBLICATION

Journal of Controlled Release 235 (2016) 91–98



Contents lists available at ScienceDirect

Journal of Controlled Release

journal homepage: www.elsevier.com/locate/jconrel

Intraperitoneal chemotherapy of ovarian cancer by hydrogel depot of paclitaxel nanocrystals



Bo Sun^a, Maie S. Taha^{a,b}, Benjamin Ramsey^c, Sandra Torregrosa-Allen^c, Bennett D. Elzey^{c,d}, Yoon Yeo^{a,e,*}

^a Department of Industrial and Physical Pharmacy, Purdue University, 575 Stadium Mall Drive, West Lafayette, IN 47907, USA

^b Department of Pharmaceutics and Industrial Pharmacy, Faculty of Pharmacy, Cairo University, Cairo, Egypt

^c Biological Evaluation Shared Resource, Purdue University Center for Cancer Research, 201 S. University Street, West Lafayette, IN 47907, USA

^d Department of Comparative Pathobiology, Purdue University, West Lafayette, IN 47907, USA

^e Weldon School of Biomedical Engineering, Purdue University, West Lafayette, IN 47907, USA

ARTICLE INFO

Article history:

Received 12 December 2015

Received in revised form 20 May 2016

Accepted 25 May 2016

Available online 26 May 2016

Keywords:

Nanocrystals

Intraperitoneal chemotherapy

Hydrogel depot

Drug delivery

Ovarian cancer

ABSTRACT

Intraperitoneal (IP) chemotherapy is a promising post-surgical therapy of ovarian cancer, but the full potential is yet to be realized. To facilitate IP chemotherapy of ovarian cancer, we developed an *in-situ* crosslinkable hydrogel depot containing paclitaxel (PTX) nanocrystals (PNC). PNC suppressed SKOV3 cell proliferation more efficiently than microparticulate PTX precipitates (PPT), and the gel containing PNC (PNC-gel) showed a lower maximum tolerated dose than PPT-containing gel (PPT-gel) in mice, indicating greater dissolution and cellular uptake of PNC than PPT. A single IP administration of PNC-gel extended the survival of tumor-bearing mice significantly better than Taxol, but PPT-gel did not. These results support the advantage of PNC over PPT and demonstrate the promise of a gel depot as an IP drug delivery system.

© 2016 Elsevier B.V. All rights reserved.

1. Introduction

Peritoneal malignancies are currently managed by surgical debulking of visible tumors and subsequent chemotherapy of residual microscopic tumors [1–3]. Intraperitoneal (IP) chemotherapy has been pursued as a promising post-surgical therapy. A well-formulated IP chemotherapy can maintain an effective local drug concentration for a prolonged period and maximize the locoregional effects on residual tumors [4–9]. IP chemotherapy has proven more effective than intravenous (IV) therapy in several clinical studies [2,10,11]. Furthermore, part of the IP-administered drug is slowly absorbed to systemic circulation and provides sustained systemic effects [12–14]. In 2006, the National Cancer Institute issued an official announcement encouraging the clinical use of combined IP and IV chemotherapy for patients with optimally resected stage III ovarian cancer, based on clinical evidence of survival benefits [15]. A recent review of clinical practice in 2006–2012 finds that IP/IV chemotherapy have significantly improved the overall survival as compared with IV chemotherapy alone [16].

Despite the clinically-proven advantages, IP chemotherapy has been met with mixed enthusiasm. Frequently mentioned problems are the complications related to IP infusion, including abdominal pain, intolerance to a high level of drug, and discomfort related to the catheter

implantation [17]. We speculate that these problems mainly stem from the difficulty in drug release control. Small molecule drugs such as paclitaxel (PTX) or docetaxel were cleared from the peritoneal cavity in less than a day [18–20]. The short IP retention time requires frequent or continuous dosing, necessitating the use of large volume infusion and indwelling catheters. For IP chemotherapy to provide the anticipated benefits, it is critical that the formulation control the drug release and avoid burst initial release and bulk drug absorption to the systemic circulation.

Considering this need, we previously developed an injectable depot consisting of *in-situ* crosslinkable hyaluronic acid (HA) gel and micrometer-scale PTX precipitates (PPT) to improve the IP retention of PTX [21]. The gel remained in the peritoneal cavity and maintained a high level of local PTX concentration in mice for 2 weeks. However, in suppressing IP SKOV3 human ovarian cancer xenografts, the PPT-gel was not better than Taxol-gel, which released PTX much faster than PPT-gel. Possible explanations were that the dissolution of PPT was too slow to provide an effective local drug concentration and/or the duration of experiment was too short to observe the benefit of prolonged IP retention of PPT.

In the present study, we aim to overcome this challenge by replacing PPT with nanocrystals (PNC), which can accelerate PTX dissolution from the HA gel. Nanocrystals are crystalline particles of poorly soluble drugs in nanometer range [22]. They are produced by breaking down large particles (“top-down”) or crystallizing from drug solutions (“bottom-up”) with an optional aid of surfactants or polymeric surface stabilizers [22,23]. Due to the small size and thus, the high surface area to volume

* Corresponding author at: Department of Industrial and Physical Pharmacy, Purdue University, 575 Stadium Mall Drive, West Lafayette, IN 47907, USA.
E-mail address: yyeo@purdue.edu (Y. Yeo).

ratio, nanocrystals can show greater dissolution rate than larger particles [24,25]. Here, we produced PNC by anti-solvent and temperature-induced crystallization and evaluated its ability to enhance PTX release *in vitro* as compared to PPT. PNC was administered IP with the HA gel as an injection medium to mice bearing SKOV3 ovarian tumor xenografts in the peritoneal cavity. Progression of tumor burden after single treatment was monitored up to 14 weeks using non-invasive whole body imaging, and the outcome was compared with those of PPT-gel and Taxol. PNC killed SKOV3 ovarian cancer cells more efficiently than PPT, and the PNC-containing gel outperformed Taxol to a greater extent than PPT-containing gel in extending the survival of tumor-bearing mice. These results support the advantage of PNC over PPT and demonstrate the promise of a gel depot as an IP drug delivery system.

2. Materials and methods

2.1. Materials

Hyaluronic acid (HA, 20 kDa and 500 kDa) was purchased from Lifecore Biomedical, LLC (Chaska, MN, USA). Paclitaxel (PTX) was a gift of Samyang Biopharm (Seoul, Korea). Carbamazepine was purchased from Enzo life sciences (Plymouth Meeting, PA, USA). Cremophor ELP was a gift from BASF (New York, NY, USA). D-Luciferin potassium salt was purchased from Gold Biotechnology (St. Louis, MO, USA). Geneticin® selective antibiotic (G418 sulfate, 50 mg/mL) was purchased from Life technologies (Grand Island, NY, USA). Cell culture medium and supplements were purchased from Invitrogen (Carlsbad, CA, USA). Micro BCA Protein Assay Kit was purchased from Life technologies (Grand Island, NY, USA). All other reagents were purchased from Sigma-Aldrich (St. Louis, MO, USA).

2.2. Preparation and characterization of PTX nanocrystals (PNC)

PNC were prepared according to the published method [26]. Briefly, 4 mg/mL PTX/ethanol solution was added to 20 mL of deionized (DI) water and stirred at 42 rcf for 10 min in a round-bottom flask immersed in a sonication bath filled with ice water. The formed PNC was captured on a 100 nm polycarbonate membrane and resuspended in DI water. Taxol and PPT were prepared as described previously [21]: Taxol was prepared by diluting “Taxol concentrate” (6 mg PTX dissolved in 1 mL of 1:1 mixture of Cremophor ELP and ethanol). PPT was prepared by the addition of PTX-dimethyl sulfoxide (DMSO) solution to DI water without low temperature, vigorous stirring or sonication.

The particle size of PNC was measured with a Zetasizer Nano-ZS90 (Malvern instruments, Westborough, MA, USA). The zeta potentials of PNC and PPT were measured with a Zetasizer Nano-ZS90 in 1 mM phosphate buffer (pH 7.4). The morphology of lyophilized PNC and PPT was visualized with a FEI Nova nanoSEM field emission scanning electron microscopy (Hillsboro, OR, USA). Freeze-dried PNC was sputter-coated with platinum for 1 min and observed with a high resolution through-the-lens detector under 5 kV accelerating voltage and spot size 3. PPT suspended in DI water was observed with Axio Imager 2 microscope with polarized light (Carl Zeiss Microscopy GmbH, Germany). X-ray powder diffraction (XPRD) patterns of lyophilized PNC and PPT were obtained on a Siemens D5000 X-ray diffractometer with a CuK α radiation source (40 kV, 40 mA). The measurement was conducted at room temperature over an angle (2θ) range of 5–40° with a step size of 0.02° and a scan rate of 4°/min.

2.3. Preparation of in-situ crosslinkable HA gel loaded with PPT or PNC (PPT-gel or PNC-gel)

HA gel was prepared by crosslinking HA-adipic acid dihydrazide (HA-ADH) and HA-aldehyde (HA-CHO) *in situ* as described previously [21,27]. HA-ADH was synthesized by conjugating adipic dihydrazide to carboxyl groups in HA via 1-ethyl-3-carbodiimide (EDC) and 1-

hydroxybenzotriazole (HOBT) at pH 6.8 and room temperature. HA-CHO was produced by oxidizing HA with sodium periodate. HA-ADH and HA-CHO were purified by dialysis, freeze dried and stored at 4 °C until use. PNC- or PPT-gel was prepared by suspending PNC or PPT in solutions of these HA derivatives in phosphate buffered saline (PBS, pH 7.4) and extruding them through a common outlet using a double-barreled syringe. HA concentration in the gel was 40 mg/mL.

2.4. Dissolution kinetics of PPT and PNC

Dissolution kinetics of PPT and PNC was tested in 0.05% or 0.2% PBST following a method described by Peschka et al., which used an agarose hydrogel to contain drug-encapsulated liposomes, thereby separating them from receptor medium [28]. In this study, we replaced agarose gel with photocrosslinkable polyethyleneglycol (PEG) hydrogel to avoid the thermal effect needed to dissolve agarose. PPT and PNC equivalent to 15 μ g of PTX were suspended in 0.25 mL of 10% PEG dimethylacrylate (PEGDA, 3400 Da) solution in PBS. The suspensions were crosslinked under UV (365 nm) illumination for 10 min in the presence of 25 μ L of irgacure solution (20% w/v in methanol). The crosslinked PEGDA matrix was briefly rinsed with water to remove free PPT or PNC. One milliliter of PBST was added to the PNC- or PPT-containing PEGDA matrices ($n = 3$ per group), which were then incubated at 37 °C on an orbital shaker. At predetermined time points, the entire release medium was sampled, and the PEGDA surface was washed with another 1 mL of fresh medium; the 2 mL was combined together for HPLC analysis. One milliliter of fresh medium was added to the matrices for further incubation. The sampled release media were mixed with an equal volume of acetonitrile (ACN) prior to HPLC analysis.

2.5. PTX release kinetics from PPT-gel and PNC-gel

PTX release from the gels was studied in two ways: one in the sink condition (total drug concentration being less than one third of the saturation solubility [29]) and the other in a condition violating the sink condition. For the release kinetics study in the sink condition, 0.1 mL of PNC-gel or PPT-gel containing 22 μ g PTX was formed as described in Section 2.3 and placed in a tube containing 20 mL of 0.2% PBST ($n = 3$). This condition made the initial PTX concentration in the release medium 1.1 μ g/mL, less than one third of PTX solubility in 0.2% PBST (5.5 μ g/mL). Thirty-six identical samples were incubated at 37 °C on an orbital shaker. At predetermined time points, 3 samples per group were taken and centrifuged at 2095 rcf for 10 min to separate the gels. The collected gels were freeze-dried and incubated with 5 mL of ACN/water (50/50) mixture at room temperature for 24 h. The swollen gels were ground with a mortar and a pestle to help release PTX into ACN/water. The crushed gel suspension was filtered and analyzed with HPLC to determine the PTX content, according to the condition described in Section 2.7. For a non-sink condition, 0.3 mL of PNC-gel or PPT-gel containing 200 μ g PTX was placed in a container with 20 mL of 0.2% PBST ($n = 3$). The initial PTX concentration in the release medium was therefore 10 μ g/mL, 2 times higher than the PTX solubility in PBST [30]. All the samples were incubated at 37 °C on an orbital shaker. At predetermined time points, 3 mL release medium were sampled and centrifuged at 9300 rcf for 10 min to separate a supernatant. Two milliliters of the supernatant was taken for HPLC analysis, and the remaining 1 mL was combined with 2 mL of fresh PBST and returned to the sample tube for further incubation.

2.6. Cytotoxicity and cellular retention of PTX

SKOV3 human ovarian cancer cells (ATCC) were maintained in RPMI-1640 medium supplemented with 10% fetal bovine serum (FBS) and 1% penicillin-streptomycin. Cells were plated in a 12-well plate at a density of 200,000 cells per well with 0.8 mL of complete medium.

After 24 h incubation, PNC or PPT suspended in 88 μ L PBS (pH 7.4) was added to each well to make the final PTX concentration 6 μ g/mL (7 μ M). A control group was treated with 88 μ L PBS. Cells were incubated with the treatments for 3 h and washed twice with 0.5 mL complete medium after removal of the treatments. The treated cells were incubated for two days in fresh medium and evaluated with the MTT (3-(4,5-dimethylthiazol-2-yl)-2,5-diphenyltetrazolium bromide) assay. The absorbance of the solubilized formazan was measured with a SpectraMax M3 microplate reader (Molecular Devices, Sunnyvale, CA, USA) at a wavelength of 562 nm. The measured absorbance was normalized to the absorbance of the control group. To determine PTX retained in the cells after each treatment, another set of SKOV3 cells were treated in the same way as above. Immediately after removing treatments, 1 mL of sterile water was added to each well, frozen and thawed once to lyse the cells. The cell lysate was analyzed with HPLC and Micro BCA assay to determine the concentrations of PTX and protein, respectively.

In a separate experiment, SKOV3 cells were plated in a 12-well plate at a density of 60,000 cells per well with 1.5 mL of complete medium. After 24 h incubation, a Transwell insert was suspended in each well as a container of a PTX treatment. The Transwell membrane was perforated with fifteen 21-gauge needle holes to facilitate the transport of released PTX (either as free molecules or particles) to the underlying cell layer. 0.1 mL of PNC-gel, PPT-gel, PNC, or PPT suspension was placed in each insert along with 0.4 mL PBS, making the final PTX concentration in each well 30 μ g/mL (35 μ M). A control group was treated with 0.1 mL of PBS. Cells were incubated with the treatments for 3 h, 24 h or 48 h, removed of the treatments, washed twice, and incubated for additional two days in complete medium prior to the MTT assay.

2.7. HPLC analysis of PTX

PPT and PNC were quantified after dissolving in 50% ACN and analyzed with HPLC. PTX in PBST solution (both 0.05% and 0.2%) was directly analyzed with HPLC after filtration with a 0.45 μ m PVDF syringe filter. PTX in the crushed gel suspension was centrifuged at 9300 rcf for 10 min and filtered with a 0.45 μ m PVDF syringe filter prior to HPLC analysis. PTX in the cell lysate was analyzed after ethyl acetate extraction. Briefly, 2 mL of the cell lysate was spiked with 10 μ g/mL carbamazepine as an internal standard, mixed with 6 mL ethyl acetate, and agitated on a rotating shaker for 40 min. The mixture was then centrifuged at 3724 rcf for 15 min to separate an organic layer, which was transferred to a new glass vial and dried under vacuum. The dried sample was dissolved in the HPLC mobile phase, filtered through 0.45 μ m syringe filter, and analyzed with HPLC. A calibration curve was drawn with PTX dissolved in complete medium (containing 10% FBS) in known concentrations, treated in the same manner as the sample solutions. PTX was analyzed with HPLC equipped with UV detector (1100 series, Agilent Technologies, Palo Alto, CA) and an Ascentis C18 column (25 cm \times 4.6 mm, particle size 5 μ m) (Supelco, St. Louis, MO, USA). The mobile phase was a mixture of ACN and water (50:50), run in the isocratic mode at a flow rate of 1 mL/min. PTX was detected at 227 nm.

2.8. Determination of the maximum tolerated doses (MTDs) of treatments

All animal procedures were approved by Purdue Animal Care and Use Committee, in conformity with the NIH guidelines for the care and use of laboratory animals. The MTD of each treatment was determined according to the method published by the National Cancer Institute's Developmental Therapeutics Program [31]. Healthy female Balb/c wild-type mice (8–10 week old, ~20 g, Harlan Laboratories, Indianapolis, IN, USA) were randomly assigned to Taxol, PPT-gel, and PNC-gel groups and given a single IP injection of each formulation at different dose levels (one mouse per dose). The mice were observed over a period of 2 weeks after the injection. The highest dose tolerated without >20% weight loss or other signs of significant toxicity was designated

as the MTD of each treatment. This experiment was repeated at least three times to confirm the reproducibility.

2.9. In-vivo efficacy studies

A mouse model of IP tumor was prepared as described in our previous study [21]. Luciferase-expressing SKOV3 (SKOV3-luc) cells [32] were maintained in complete RPMI-1640 medium containing 500 μ g/mL G418 sulfate. 10^7 cells were suspended in 1 mL RPMI-1640 medium and IP injected to a female Balb/c nude mouse (8–10 week old, ~20 g, Harlan Laboratories). Tumor growth was monitored every week by measuring the bioluminescence with the IVIS Lumina II whole body imaging system (Caliper Life Science, Hopkinton, MA, USA) [33]. When the radiance of tumors reached 10^5 – 10^6 p/s/cm²/sr, which took 1–2 weeks, animals were evenly assigned to 5 treatment groups (n = 3 per group per study, repeated three times, total n = 9 per group): PBS, HA gel, Taxol, PNC-gel and PPT-gel (equivalent to 30 mg/kg of PTX). One milliliter of each treatment was IP injected through a catheter, and the skin was sealed with GLUture topical tissue adhesive (Abbott Park, IL, USA). Bioluminescence of IP tumor was measured weekly up to 14 weeks. Animals were observed every 3 days for weight change and signs of pain until they reached the criteria of sacrifice, which include >20% loss in body weight, bloated abdomen and signs of respiratory distress, according to the approved animal procedure.

2.10. Statistical analysis

All *in vitro* data were analyzed using GraphPad Prism 6 (La Jolla, CA, USA), with the unpaired *t*-test to determine the difference of means between two groups. The comparison of survival curves was conducted with the Log-rank (Mantel-Cox) test built in GraphPad Prism 6. A value of *p* < 0.05 was considered statistically significant. For the tumor growth study, analysis of variance (ANOVA) was performed using IBM SPSS Statistics 23 (Armonk, NY, USA) to test the differences between the treatment groups in the change of tumor burden over time.

3. Results and discussion

3.1. Characterization of PPT and PNC

The properties of PNC and PPT are summarized in Table 1. PNC were rod-shape nanoparticles with a length of 310 ± 86 nm and a width of 65 ± 10 nm under SEM (Fig. 1a). The average diameter (z-average) of PNC measured by Dynamic Light Scattering (DLS) was 258.0 ± 28.1 nm with polydispersity index values ranging from 0.045 to 0.223, which indicated mid-range polydispersity [34]. On the contrary, PPT were needle-shaped crystals with a length of 11.5 ± 2.2 μ m and a width of 2.0 ± 0.4 μ m (Fig. 1b). Polarized light microscopy detected clusters of PTX crystals, confirming the broad size distribution of PPT. Both PNC and PPT showed weakly negative charges (PNC: -5.51 ± 0.42 mV; PPT: -3.08 ± 0.98 mV) at pH 7.4. PNC and PPT exhibited

Table 1
Summary of PNC and PPT properties.

	PNC	PPT
Particle size	Length ^a : 310 ± 86 nm; Width ^a : 65 ± 10 nm z-average ^b : 258 ± 28.1 nm	Length ^c : 11.5 ± 2.2 μ m; Width ^c : 2.0 ± 0.4 μ m
Zeta potential ^d	-5.51 ± 0.42 mV	-3.08 ± 0.98 mV

^a Estimated by SEM; based on 50 measurements with ImageJ.

^b Measured by a zeta sizer (DLS); average and standard deviation of 8 independently prepared batches.

^c Estimated by light microscopy; based on 50 measurements with ImageJ.

^d Measured by a zeta sizer; average and standard deviation of 5 independently prepared batches.

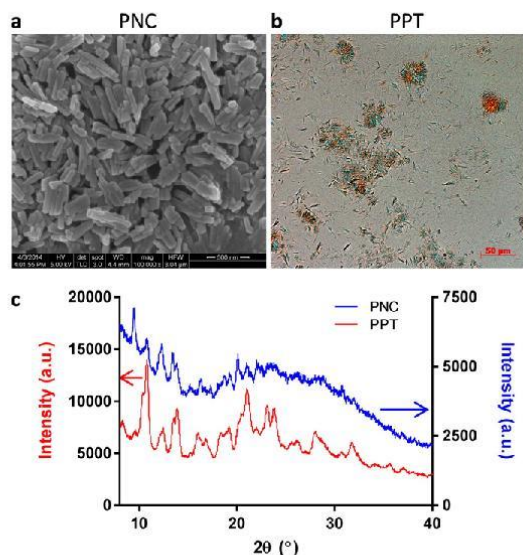


Fig. 1. (a) Scanning electron micrograph of PNC. (b) Polarized light micrograph of PPT. (c) XRPD pattern of PNC and PPT.

sharp peaks typical of crystalline solids (Fig. 1c). The crystal pattern of PNC was consistent with the result in the literature [26].

3.2. Dissolution kinetics of PPT and PNC

Drug dissolution or release kinetics of a particulate formulation is typically studied by separating dissolution medium from the formulation by high speed centrifugation or a dialysis bag and measuring the drug concentration in the sampled medium. Neither is appropriate for estimating PTX dissolution from PNC or PPT: centrifugation does not completely separate small particles from the suspension and accelerates particle aggregation, and the dialysis method bears the risk of underestimating drug release/dissolution due to drug adsorption to the membrane and/or reprecipitation of dissolved drug in the bag [30]. Alternatively, *in-situ* analytical technique based on light scattering may be used to monitor dissolution of drug particles [25]. However, this method is not applicable to large particles like PPT that sediment rapidly.

To bypass the limitations of existing methods, we used photocrosslinkable PEGDA matrix to help separate PNC and PPT from the medium during sampling. PNC and PPT were suspended in gel precursor solutions, which were solidified under UV and immersed in the release medium. The crosslinked PEGDA matrix confined particles but allowed the diffusion of the dissolution medium. The PEGDA matrix did not degrade in the dissolution medium and retained particles during the test period (Supporting Fig. 1). This method avoided problems associated with the centrifugation or dialysis methods: it eliminated the need for centrifugation pressure during sampling, kept the particles apart throughout the incubation, and prevented sample loss due to the adsorption to the container. On the other hand, the dissolution rates measured by this method would be much slower than the actual dissolution rate due to PEGDA matrix, which could delay drug diffusion up to 48 h in case of PTX. Therefore, this method was only meaningful for *in vitro* comparison of formulations. A dissolution aid was included in the medium to maintain the solubility of the dissolved PTX. Serum would have been the most physiologically relevant option; however, it was not suitable for long-term monitoring of drug dissolution due to

the detrimental effect on PTX stability [30]. Instead, we chose Tween80, which we previously found to help generate a similar PTX dissolution profile as serum with less stability issue than serum [30]. With 0.2% PBST, in which PTX was soluble up to 5.5 $\mu\text{g}/\text{mL}$, no difference in dissolution rate was observed between PNC and PPT: $78.8 \pm 2.0\%$ and $74.7 \pm 8.1\%$ of total PTX were dissolved from PNC and PPT, respectively, in 4 days (Fig. 2a, b). We suspected that 0.2% PBST might have been too invasive that it actively dissolved PTX from both particles and eliminate the difference in dissolution rate. As expected, the difference was detected in PBST with a reduced Tween80 (0.05% PBST), where PTX was less soluble (maximum 1.6 $\mu\text{g}/\text{mL}$), and thus, the medium was less invasive to the particles. The overall dissolution rate in 0.05% PBST was much slower than in 0.2% PBST, $54.8 \pm 3.0\%$ and $46.0 \pm 3.3\%$ of total PTX was dissolved from PNC and PPT, respectively, over 19 days (Fig. 2c).

3.3. Cellular retention and cytotoxicity of PPT and PNC

We then compared the cytotoxicity of PPT and PNC as an indirect indicator of drug dissolution profiles. SKOV3 cells were incubated with PPT and PNC for 3 h, and the level of PTX retained with cells were determined. Much less PTX was detected in the SKOV3 cells treated with PNC than those with PPT (Fig. 3a). The relatively high level of PTX retained with PPT-treated cells is attributable to the large size of PPT, bound on the cell surface and not readily removed from cells by gentle washing. Surprisingly, despite the low level of PTX retained with the cells, PNC showed higher cytotoxicity than PPT (Fig. 3b). The cell fraction affected by the unit amount of PTX was 3.3 times greater for PNC than PPT (Fig. 3c), which indicates that PNC killed SKOV3 cells more efficiently than PPT. These results suggest that the small size of PNC facilitated PTX dissolution and increased its availability to the cells as compared to PPT. In addition, the small size may have helped PNC to enter cells. A recent study supports that drug nanocrystals could be endocytosed as solid particles [35].

3.4. *In-vitro* PTX release kinetics from PPT-gel and PNC-gel

To predict the drug release from PPT-gel and PNC-gel in the peritoneal cavity, we evaluated *in-vitro* PTX release kinetics in 0.2% PBST. We first attempted to compare the release rates under a sink condition as defined by the United States Pharmacopeia (the volume of medium at least three times that required to form a saturated solution of a drug [29]). Since the highest PTX concentration (1.1 $\mu\text{g}/\text{mL}$) in the release medium fell far below the limit of quantitation (3.8 $\mu\text{g}/\text{mL}$) calculated per the ICH guideline, the released amount was indirectly determined by measuring the PTX amount remaining in the gel at each time point and subtracting it from the initial PTX amount. With this method, up to 80% of PTX was found to be released from the gels in 7 days, with no apparent difference between PPT-gel and PNC-gel

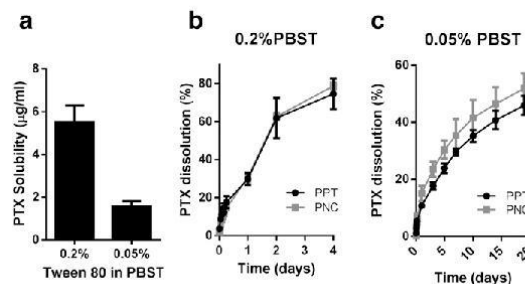


Fig. 2. (a) Solubility of PTX in PBST. Dissolution kinetics of PPT and PNC in (b) 0.2% PBST and (c) 0.05% PBST.

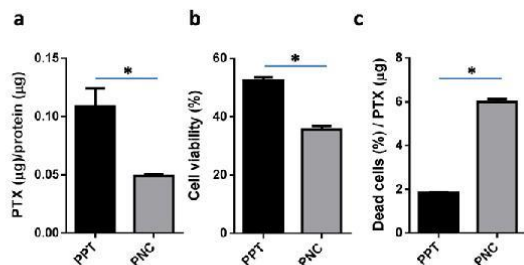


Fig. 3. (a) PTX retention normalized with total protein content. Micro BCA assay was performed to determine the total protein content in the cell lysate as an estimate of cell population. The PTX to protein ratio reflects PTX retained by each cell. (b) Cytotoxicity of PPT and PNC (equivalent to 7 µM PTX) to SKOV3 cells after 3 h of direct exposure followed by incubation in drug-free medium. (c) Fraction of cells affected by unit amount of PTX. Data are expressed as averages and standard deviations of three measurements of a representative batch. *: $p < 0.05$ by *t*-test.

(Fig. 4a), probably for the same reason as described in Section 3.2 (invasiveness of 0.2% PBST).

We next tested the dissolution rate in a non-sink condition to reflect the limited fluid volume in the peritoneal cavity. The volume of peritoneal fluid in a healthy adult is approximately 50 mL with a protein content 75% lower than that of the blood [36,37]. The turnover rate of peritoneal fluid is 4–5 mL/h [36]. A Balb/c mouse, used in this study, has < 1 mL peritoneal fluid. Since the small volume of the peritoneal fluid (compared to blood) is likely to challenge the sink condition assumption, we used 20 mL of 0.2% PBST for PPT-gel and PNC-gel equivalent to 200 µg of PTX to create a situation that intentionally violated a sink condition. The release medium sampled at each time point was directly analyzed to determine the cumulative drug release. Under the non-sink condition, 32.6% and 30.6% of the total PTX were released from PPT-gel and PNC-gel, respectively, in 12 days (Fig. 4b). 66.0% (PPT-gel) and 59.7% of PTX (PNC-gel) were recovered in the remaining gel (Supporting Fig. 2). The relatively slow release (compared to the sink condition) suggests that the released PTX might have undergone reprecipitation in the medium as the PTX concentration reached the saturation solubility [30], especially in the presence of existing seeds such as PTX particles. Although we expected that the two gels would show different release kinetics at least initially, we did not observe any difference, most likely due to rapid reprecipitation of released PTX.

The lack of difference in *in-vitro* release kinetics between PPT-gel and PNC-gel may be explained in two ways. First, both methods may

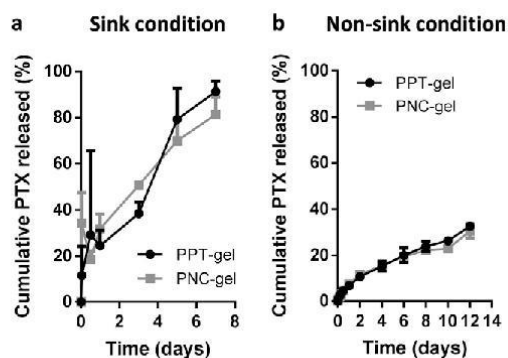


Fig. 4. (a) *In-vitro* PTX release kinetics from PPT- and PNC-gels under sink condition (initial PTX concentration: 1.1 µg/mL). (b) *In-vitro* PTX release kinetics from PPT- and PNC-gels under non-sink condition (initial PTX concentration: 10 µg/mL).

involve the centrifugation-induced artifacts. In the sink condition method, it is possible that the remaining PTX at each time point might have been underestimated (*i.e.*, drug release overestimated) due to the centrifugation, which would have pressurized the gels and caused artificial release of PPT and PNC loosely associated with them. In the non-sink method, the centrifugation force might have contributed to underestimation by accelerating the aggregation of reprecipitates. Second, the invasiveness of Tween80, observed in the dissolution kinetics study, might have masked the potential difference between two gels.

3.5. Cytotoxicity of PPT-gel and PNC-gel

Acknowledging these limitations of *in vitro* release kinetics tests, we measured the cytotoxicity of PPT-gel and PNC-gel varying the exposure time to predict their *in vivo* effects. The gel was contained in a perforated Transwell insert to avoid direct contact with the cell layer that might limit oxygen supply. Free particles were supplied in the same manner to mimic a situation where degrading gel was no longer able to retain the particles. Therefore, the tests with gels and free particles represented the initial and later phase of the delivery, respectively. With 3 h exposure, PNC-gel was found to be more toxic than PPT-gel, indicating faster dissolution of PNC than PPT (Fig. 5a). This difference disappeared upon longer incubation (24 h and 48 h), which may be explained by the reprecipitation of released PTX exceeding the saturation solubility, as expected from the release kinetics results. In contrast, free PNC showed consistently high cytotoxicity as compared to PPT, indicating that at least part of PNC were endocytosed by the cells as solid particles before they underwent dissolution and reprecipitation in the medium (Fig. 5b). This result suggests that PNC-gel would achieve greater anti-tumor effect than PPT-gel *in vivo*, as the endocytosis of released PNC offset the effect of reprecipitation of dissolved PTX.

3.6. MTDs of PPT-gel and PNC-gel

MTDs of PNC-gel, PPT-gel, and Taxol were determined using healthy Balb/c mice to determine the maximum PTX dose to administer in the anti-tumor efficacy study. Mice did not survive a single administration at doses higher than 60 mg/kg of Taxol. On the other hand, PPT-gel and PNC-gel were tolerated at much higher doses: 120 mg/kg and 90 mg/kg, respectively. This result first confirms the benefit of the gel formulations free of the toxic solubilizer, Cremophor ELP [38]. Interestingly, PNC-gel showed lower MTD than PPT-gel, despite the identical composition. The difference between PNC-gel and PPT-gel suggests that PNC-gel might have released a greater amount of PTX (as free drug and/or PNC) than PPT-gel in the given time. This result is consistent with the cellular PTX retention and cytotoxicity results.

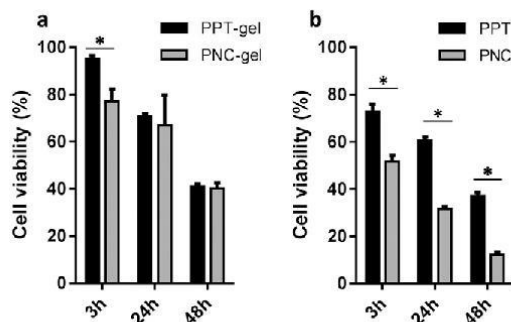


Fig. 5. Cytotoxicity of (a) PNC-gel and PPT-gel and (b) PPT and PNC (equivalent to 35 µM PTX) to SKOV3 cells after 3 h, 24 h or 48 h exposure *via* a perforated Transwell membrane, followed by incubation in drug-free medium. Data are expressed as averages and standard deviations of three measurements of a representative batch. *: $p < 0.05$ by *t*-test.

3.7. Anti-tumor effects of PPT-gel and PNC-gel

The anti-tumor efficacy of PPT- and PNC-gels was studied using a mouse model of IP tumor. Once the tumor reached a certain size as indicated by the bioluminescence signals, treatments (Taxol, PPT-gel, and PNC-gel) equivalent to 30 mg/kg PTX as well as vehicle controls were administered IP once. A single administration regimen was chosen to compare the duration of the therapeutic effects of the treatments (Fig. 6a). The tumor burden was monitored up to 14 weeks until the animals reached a humane endpoint (Fig. 6b). Animals treated with PBS or HA gel vehicle reached the endpoint in <7 weeks with median survival periods of 37 days. All animals receiving PTX-treatments survived longer than the vehicle control groups with notable difference among the treatments. Tumor growth in animals treated with Taxol was initially delayed but resumed after 3 weeks to reach the endpoint in <9 weeks with a median survival time of 56 days. This result may be explained by the rapid clearance of PTX from the peritoneal cavity [21]. Animals treated with PPT-gel showed a similar survival curve (median survival time of 51 days) as Taxol-treated ones. On the other hand, mice treated with PNC-gel showed a significant extension of the survival period (67 days), which clearly contrasted with Taxol-treated groups ($p < 0.05$; PNC-gel vs. Taxol, Log rank Mantel-Cox test) (Fig. 6c). Both PPT-gel- and PNC-gel-treated animals showed minimal increase in tumor signals in surviving animals until 7 weeks post-treatment (Fig. 6b, Supporting Fig. 3). However, statistical differences between the two groups based on bioluminescence signals vs. time plot were not achieved due to the attrition of animals over the survival period and the large variation in tumor growth. Thus, the change of tumor burden (tumor burden at each time point – initial tumor burden) was plotted with respect to the survival time for each mouse, and the area under the curve over time (AUC/time) was calculated as an estimate of

average tumor burden during the survival period. The mice treated with PNC-gel or PPT-gel showed the lowest median AUC/time value among the treatments (Fig. 6d). The AUC/time value of Taxol group was not significantly different from PBS or HA gel control groups. Both PPT-gel and PNC-gel showed significantly lower AUC/time values than Taxol group, but the difference between PNC-gel and Taxol groups was more significant than that of PPT-gel and Taxol groups ($p: 0.0012$ vs. 0.0306).

Taken together, the *in vivo* studies demonstrated that a single dose PNC-gel was significantly better than Taxol in delaying tumor progression. PPT-gel was not different from Taxol in the median survival time. This result is consistent with the *in vitro* cellular toxicity test and MTD values, which indicated greater dissolution and cellular uptake of PNC than PPT. Based on the depot effect of HA gel, PNC could have a prolonged effect on IP tumors than Taxol. It remains to be investigated how the prolonged local delivery improved the efficacy of PTX. A potential mechanism may involve the tumor priming effect by initial PTX exposure, which suppresses stroma expansion [39], thereby facilitating the transport of subsequently released PTX. A remaining challenge is to improve the specificity of local delivery of PTX. The current PNC-gel does not have a mechanism to distinguish tumors vs. normal tissues; thus, some toxicity to adjacent normal tissues is likely unavoidable (although no abnormalities were observed on macroscopic level in this study). This may be achieved by surface modification of PNC with tumor cell-interactive ligands.

3.8. Perspective on the predictive value of *in vitro* release kinetics studies

This study illustrates how *in vitro* release kinetics studies can have little value in predicting *in vivo* outcomes. *In vitro* release kinetics studies are routinely performed to demonstrate the ability of new

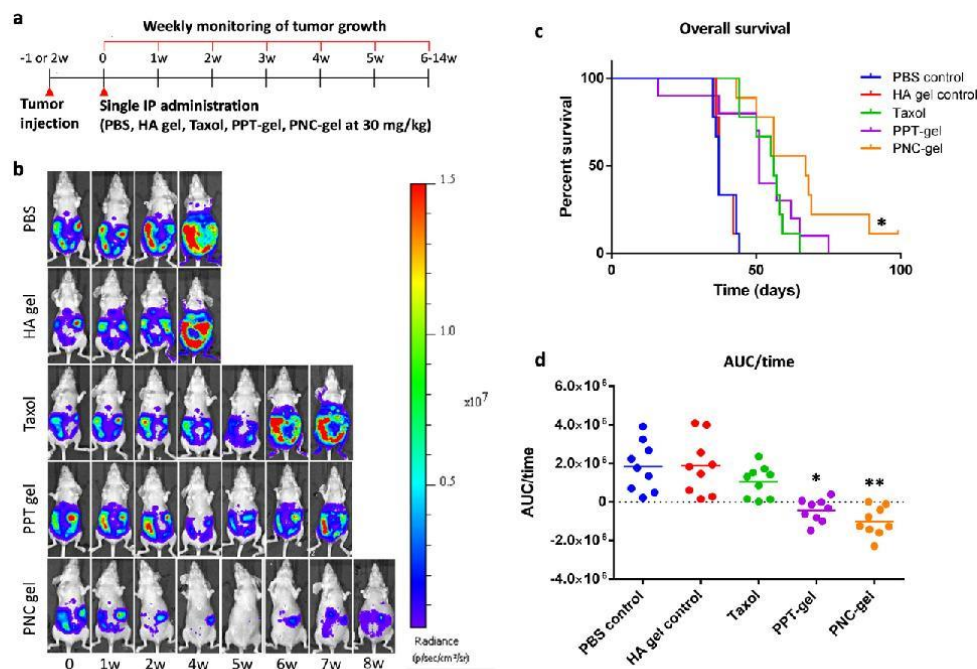


Fig. 6. (a) Treatment schedule. (b) Representative whole body bioluminescence images of animals administered with different treatments. The most representative animal in each group is presented. (c) Kaplan-Meier analysis for survival time post-tumor cells inoculation. $n = 9$ per group. *: $p < 0.05$, PNC-gel vs. Taxol by Log-rank Mantel-Cox test. (d) AUC of tumor burden change over survival time of animals treated with PBS, HA gel, Taxol, PNC-gel and PPT-gel. *: $p < 0.05$, PPT-gel vs. Taxol, **: $p < 0.05$, PNC-gel vs. Taxol by Tukey's test.

formulations to control the drug release. Our release kinetics studies, performed in both sink and non-sink conditions, failed to distinguish between PNC-gel and PPT-gel. Nevertheless, the *in vivo* MTD and anti-tumor effect studies show that PNC-gel can provide greater benefits than PPT-gel as compared to Taxol. In this regard, it is worthwhile to revisit the current practice of *in vitro* release kinetics studies. Drug release kinetics is largely affected by sampling methods, choice of release medium, and the concentration difference between the formulation and the release medium [30]. Various methods and conditions are employed in the literature, however, with very little justifications. Sampling methods involve the aforementioned problems such as accelerated aggregation or delayed diffusion. The sink condition assumption is not necessarily applicable to some parts of the body, including the peritoneal cavity. 0.2% PBST is widely used as a dissolution/release medium for poorly water-soluble drug formulations as a solubility enhancer [40–45]; however, its physiological relevance is not clearly established, and the active role of Tween80 in drug release is seldom considered in data interpretation. These limitations critically hamper the translation of drug delivery technologies and warrant increased efforts for developing new *in vitro* methods with greater predictive potential.

4. Conclusion

PTX-gel formulation comprising PNC and HA gel was developed for IP chemotherapy of ovarian cancer. In cellular toxicity test and MTD assessment, PNC-gel provided more efficient killing effect and greater toxicity than PPT-gel containing larger PTX particles. A single IP administration of PNC-gel outperformed the same dose Taxol in extending the survival of mice with IP tumors, due to the local depot effect, but PPT-gel did not. The cell toxicity test and *in vivo* results consistently point to the beneficial effect of particle size reduction, which lead to a greater dissolution rate and cellular uptake of PTX.

Acknowledgments

This work was supported by NSF DMR-1056997, NIH R01EB017791, Purdue Research Foundation Research Grant, and the Purdue University Center for Cancer Research Small Grants Program. We also acknowledge the fellowship support from the Egyptian Government Ministry of Higher Education Missions Sector to M.S.T. The *in vivo* data were acquired at the Biological Evaluation Shared Resource supported by NIH P30 CA023168. We appreciate the kind donation of the SKOV3-luc cell line from Prof. Glen S. Kwon at University of Wisconsin at Madison. We also thank Samyang Biopharm (Seoul, Korea) for the kind donation of paclitaxel and the NAL Pharmaceuticals Ltd. (Monmouth Junction, NJ, USA) for the gift support. We thank the Statistical Consulting Service in the Department of Statistic at Purdue University for the help with *in vivo* data analysis and Alice C. Chang for technical assistance with *in vitro* PTX release kinetics.

Appendix A. Supplementary data

Supplementary data to this article can be found online at <http://dx.doi.org/10.1016/j.jconrel.2016.05.056>.

References

- [1] K. Munstedt, F.E. Franke, Role of primary surgery in advanced ovarian cancer, *World J. Surg. Oncol.* 2 (2004) 32.
- [2] D.K. Armstrong, B. Bundy, L. Wenzel, H.Q. Huang, R. Baergen, S. Lele, L.J. Copeland, J.L. Walker, R.A. Burger, Intraperitoneal cisplatin and paclitaxel in ovarian cancer, *N. Engl. J. Med.* 354 (1) (2006) 34–43.
- [3] R.F. Ozols, B.N. Bundy, B.E. Greer, J.M. Fowler, D. Clarke-Pearson, R.A. Burger, R.S. Mannel, K. DeGeest, E.M. Hartenbach, R. Baergen, Phase III trial of carboplatin and paclitaxel compared with cisplatin and paclitaxel in patients with optimally resected stage III ovarian cancer: a Gynecologic Oncology Group study, *J. Clin. Oncol.* 21 (17) (2003) 3194–3200.
- [4] R.L. Dedrick, M.F. Flessner, Pharmacokinetic problems in peritoneal drug administration: tissue penetration and surface exposure, *J. Natl. Cancer Inst.* 89 (7) (1997) 480–487.
- [5] M. Markman, Intraperitoneal drug delivery of antineoplastics, *Drugs* 61 (8) (2001) 1057–1065.
- [6] M. Markman, E. Rowinsky, T. Hakes, B. Reichman, W. Jones, J.L. Lewis, S. Rubin, J. Curtin, R. Barakat, M. Phillips, Phase I trial of intraperitoneal taxol: a Gynecologic Oncology Group study, *J. Clin. Oncol.* 10 (9) (1992) 1485–1491.
- [7] S.K. Chambers, H.H.S. Chow, M.F. Janicek, J.M. Gragun, K.D. Hatch, H. Cui, C. Laughren, M.C. Clouser, J.L. Cohen, H.M. Wright, N. Abu Shahin, D.S. Alberts, Phase I trial of intraperitoneal metretexed, cisplatin, and paclitaxel in optimally debulked ovarian cancer, *Clin. Cancer Res.* 18 (9) (2012) 2668–2678.
- [8] C. Hasovits, S. Clarke, Pharmacokinetics and pharmacodynamics of intraperitoneal cancer chemotherapeutics, *Clin. Pharmacokinet.* 51 (4) (2012) 203–224.
- [9] J.L. Au, Z. Lu, M.G. Wientjes, Versatility of particulate carriers: development of pharmacodynamically optimized drug-loaded microparticles for treatment of peritoneal cancer, *AAPS J.* 17 (5) (2015) 1065–1079.
- [10] D.S. Alberts, P.Y. Liu, E.V. Hannigan, R. O'Toole, S.D. Williams, J.A. Young, E.W. Franklin, D.L. Clarke-Pearson, V.K. Malviya, B. DuBeshter, M.D. Adelson, W.J. Hoskins, Intraperitoneal cisplatin plus intravenous cyclophosphamide versus intravenous cisplatin plus intravenous cyclophosphamide for stage III ovarian cancer, *N. Engl. J. Med.* 335 (26) (1996) 1950–1955.
- [11] M. Markman, B.N. Bundy, D.S. Alberts, J.M. Fowler, D.L. Clarke-Pearson, L.F. Carson, S. Wadler, J. Sichel, Phase III trial of standard-dose intravenous cisplatin plus paclitaxel versus moderately high-dose carboplatin followed by intravenous paclitaxel and intraperitoneal cisplatin in small-volume stage III ovarian carcinoma: an intergroup study of the Gynecologic Oncology Group, Southwestern Oncology Group, and Eastern Cooperative Oncology Group, *J. Clin. Oncol.* 19 (4) (2001) 1001–1007.
- [12] K.B. Nemes, M. Abermann, E. Bojti, G. Crezal, S. Al-Behaisi, I. Klebovich, Oral, intraperitoneal and intravenous pharmacokinetics of deramciclane and its *N*-desmethyl metabolite in the rat, *J. Pharm. Pharmacol.* 52 (1) (2000) 47–51.
- [13] P. Marchetti, O.A. Stuart, F. Mohamed, D. Yoo, P.H. Sugarbaker, Docetaxel: pharmacokinetics and tissue levels after intraperitoneal and intravenous administration in a rat model, *Cancer Chemother. Pharmacol.* 49 (6) (2002) 499–503.
- [14] C.N. Krasner, M. Roche, N.S. Horowitz, J.G. Supko, S.I. Lee, E. Oliva, Case records of the Massachusetts General Hospital. Case 11–2006. A 54-year-old woman with a mass in the pelvis, *N. Engl. J. Med.* 354 (15) (2006) 1615–1625.
- [15] NCI clinical announcement on intraperitoneal therapy for ovarian cancer, http://ctep.cancer.gov/highlights/docs/clin_annnc_010506.pdf 2006.
- [16] A.A. Wright, A. Cronin, D.E. Milne, M.A. Bookman, R.A. Burger, D.E. Cohn, M.C. Cristea, J.J. Griggs, N.L. Keating, C.F. Levenback, G. Mantia-Smaldone, U.A. Matulonis, L.A. Meyer, J.C. Niland, J.C. Weeks, D.M. O'Malley, Use and effectiveness of intraperitoneal chemotherapy for treatment of ovarian cancer, *J. Clin. Oncol.* 33 (26) (2015) 2841–2847.
- [17] M. Markman, J.L. Walker, Intraperitoneal chemotherapy of ovarian cancer: a review, with a focus on practical aspects of treatment, *J. Clin. Oncol.* 24 (6) (2006) 988–994.
- [18] F. Mohamed, P. Marchetti, O.A. Stuart, P. Sugarbaker, Pharmacokinetics and tissue distribution of intraperitoneal paclitaxel with different carrier solutions, *Cancer Chemother. Pharmacol.* 52 (5) (2003) 405–410.
- [19] F. Mohamed, O.A. Stuart, P.H. Sugarbaker, Pharmacokinetics and tissue distribution of intraperitoneal docetaxel with different carrier solutions, *J. Surg. Res.* 113 (1) (2003) 114–120.
- [20] M. Tsai, Z. Lu, J. Wang, T.K. Yeh, M.G. Wientjes, J.L. Au, Effects of carrier on disposition and antitumor activity of intraperitoneal paclitaxel, *Pharm. Res.* 24 (9) (2007) 1691–1701.
- [21] G. Bajaj, M.R. Kim, S.I. Mohammed, Y. Yeo, Hyaluronic acid-based hydrogel for regional delivery of paclitaxel to intraperitoneal tumors, *J. Control. Release* 158 (3) (2012) 386–392.
- [22] B. Sun, Y. Yeo, Nanocrystals for the parenteral delivery of poorly water-soluble drugs, *Curr. Opin. Solid State Mater. Sci.* 16 (6) (2012) 295–301.
- [23] R.H. Müller, S. Gohla, C.M. Keck, State of the art of nanocrystals – special features, production, nanotoxicology aspects and intracellular delivery, *Eur. J. Pharm. Biopharm.* 78 (1) (2011) 1–9.
- [24] V.B. Patravale, A.A. Date, R.M. Kulkarni, Nanosuspensions: a promising drug delivery strategy, *J. Pharm. Pharmacol.* 56 (7) (2004) 827–840.
- [25] K. Anhalt, S. Geissler, M. Harms, M. Weigandt, G. Fricker, Development of a new method to assess nanocrystal dissolution based on light scattering, *Pharm. Res.* 29 (10) (2012) 2887–2901.
- [26] R. Zhao, C.P. Hollis, H. Zhang, L. Sun, R.A. Gemeinhart, T. Li, Hybrid nanocrystals: achieving concurrent therapeutic and biomaging functionalities toward solid tumors, *Mol. Pharm.* 8 (5) (2011) 1985–1991.
- [27] P. Bulpitt, D. Beschlimann, New strategy for chemical modification of hyaluronic acid: preparation of functionalized derivatives and their use in the formation of novel biocompatible hydrogels, *J. Biomed. Mater. Res.* 47 (2) (1999) 152–169.
- [28] R. Peschka, C. Dennehy, F.C. Szoka, A simple *in vitro* model to study the release kinetics of liposome encapsulated material, *J. Control. Release* 56 (1–3) (1998) 41–51.
- [29] The United States Pharmacopeia, The National Formulary (USP37/NF32), The United States Pharmacopeial Convention, Inc., Rockville, MD, 2014.
- [30] S.A. Abouelmagd, B. Sun, A.C. Chang, Y.J. Ku, Y. Yeo, Release kinetics study of poorly water-soluble drugs from nanoparticles: are we doing it right? *Mol. Pharm.* 12 (3) (2015) 997–1003.
- [31] E. Lengyel, B. Schmalfeldt, E. Konik, K. Spathe, K. Harting, A. Fenn, U. Berger, R. Fridman, M. Schmitt, D. Prechtel, W. Kuhn, Expression of latent matrix metalloproteinase 9 (mmp-9) predicts survival in advanced ovarian cancer, *Gynecol. Oncol.* 82 (2) (2001) 291–298.

- [32] H. Cho, T.C. Lai, G.S. Kwon, Poly(ethylene glycol)-block-poly(ϵ -caprolactone) micelles for combination drug delivery: evaluation of paclitaxel, cyclophosphamide and gossypol in intraperitoneal xenograft models of ovarian cancer, *J. Control. Release* 166 (1) (2013) 1–9.
- [33] E.J. Cho, B. Sun, K.O. Doh, E.M. Wilson, S. Torregrosa-Allen, B.D. Elzey, Y. Yeo, Intraperitoneal delivery of platinum with in-situ crosslinkable hyaluronic acid gel for local therapy of ovarian cancer, *Biomaterials* 37 (2015) 312–319.
- [34] Malvern zetaserizer info DLS Nano and HPPS Customer Training Manual Chapter 1 DLS Theory.
- [35] Y. Chen, T. Li, Cellular uptake mechanism of paclitaxel nanocrystals determined by confocal imaging and kinetic measurement, *AAPS J.* 17 (2015) 1126–1134.
- [36] L. Sherwood, *Human Physiology: From Cells to Systems*, Thomson/Brooks/Cole, Australia; Belmont, CA, 2007.
- [37] M.S. Watson, *Oxford Handbook of Palliative Care*, Oxford University Press, Oxford; New York, 2009.
- [38] H. Gelderblom, J. Verweij, K. Nooter, A. Sparreboom, Cremophor EL: the drawbacks and advantages of vehicle selection for drug formulation, *Eur. J. Cancer* 37 (13) (2001) 1590–1598.
- [39] Z. Lu, M. Tsai, D. Lu, J. Wang, M.G. Wientjes, J.L. Au, Tumor-penetrating microparticles for intraperitoneal therapy of ovarian cancer, *J. Pharmacol. Exp. Ther.* 327 (3) (2008) 673–682.
- [40] B.E. Kilfoyle, L. Sheihet, Z. Zhang, M. Laohoo, J. Kohn, B.B. Michniak-Kohn, Development of paclitaxel-TyroSpheres for topical skin treatment, *J. Control. Release* 163 (1) (2012) 18–24.
- [41] T. Yang, F.D. Cui, M.K. Choi, J.W. Cho, S.J. Chung, C.K. Shim, D.D. Kim, Enhanced solubility and stability of PEGylated liposomal paclitaxel: in vitro and in vivo evaluation, *Int. J. Pharm.* 338 (1–2) (2007) 317–326.
- [42] E.J. Cha, J.E. Kim, C.H. Ahn, Stabilized polymeric micelles by electrostatic interactions for drug delivery system, *Eur. J. Pharm. Sci.* 38 (4) (2009) 341–346.
- [43] E. Gullotti, Y. Yeo, Beyond the imaging: limitations of cellular uptake study in the evaluation of nanoparticles, *J. Control. Release* 164 (2) (2012) 170–176.
- [44] Z. Amoozgar, J. Park, Q. Lin, Y. Yeo, Low molecular-weight chitosan as a pH-sensitive stealth coating for tumor-specific drug delivery, *Mol. Pharm.* 9 (5) (2012) 1262–1270.
- [45] E. Gullotti, J. Park, Y. Yeo, Polydopamine-based surface modification for the development of peritumorally activatable nanoparticles, *Pharm. Res.* 30 (8) (2013) 1956–1967.